AMERICAN UNIVERSITY OF BEIRUT

NUMERCIAL INVESTIGATION OF DIP-SLIP FAULT PROPAGATION EFFECTS ON OFFSHORE SEABEDS FOR PIPELINE APPLICATIONS

by

LAMA TAYSIR THEBIAN

A thesis
submitted in partial fulfillment of the requirements
for the degree of Master of Engineering
to the Department of Civil and Environmental Engineering
of the Faculty of Engineering and Architecture
at the American University of Beirut

Beirut, Lebanon

August 2016

AMERICAN UNIVERSITY OF BEIRUT

NUMERCIAL INVESTIGATION OF DIP-SLIP FAULT PROPAGATION EFFECTS ON OFFSHORE SEABEDS FOR PIPELINE APPLICATIONS

by

LAMA TAYSIR THEBIAN

Approved by:

Dr. Salah Sadek, Professor
Department of Civil and Environmental Engineering — Advisor

Dr. Shadi Najjar, Associate Professor
Department of Civil and Environmental Engineering — Co-Advisor

Dr. Mounir Mabsout, Professor
Department of Civil and Environmental Engineering — Member of Committee

Date of thesis defense: August 23, 2016

AMERICAN UNIVERSITY OF BEIRUT

THESIS, DISSERTATION, PROJECT RELEASE FORM

Student Name: _____

◯ Master's Thesis ◯ Master's Project ◯ Doctoral Dissertation

☐ I authorize the American University of Beirut to: (a) reproduce hard or electronic copies of my thesis, dissertation, or project; (b) include such copies in the archives and digital repositories of the University; and (c) make freely available such copies to third parties for research or educational purposes.

☐ I authorize the American University of Beirut, **three years after the date of submitting my thesis, dissertation, or project,** to: (a) reproduce hard or electronic copies of it; (b) include such copies in the archives and digital repositories of the University; and (c) make freely available such copies to third parties for research or educational purposes.

_____

Signature Date

ACKNOWLEDGMENTS

First and foremost I wish to thank my advisors, Professor Salah Sadek and Shadi Najjar my professors in the Geotechnical Engineering department at AUB. They have been supportive since my first days at the university and the days I started my research work. They helped come up with the thesis topic and guided me all over the masters program. They gave me the moral and academic support throughout the journey to finish the thesis.

Special thanks to Professor Mounir Mabsout for his guidance and assistance in our finite element modeling work and his patience.

PHD candidate Samer Hasan supported me continuously in my work and Professor Elie Hantouche was always helpful and allowed us to use his Abaqus licenses whenever we needed them.

I would like to thank my parents and family for supporting me throughout my life.

-AN ABSTRACT OF THE THESIS OF

Lama Taysir Thebian for Master of Engineering
Major: Civil Engineering

Title: Numerical Investigation of Dip-Slip fault Propagation Effects on Offshore Seabed for Pipeline Applications

The present thesis addresses the behavior of seabed sands subjected to underlying dip-slip fault movement. This problem is of interest in reference to subsea oil/gas pipelines connecting offshore platforms to the shoreline, crossing known existing dip-slip faults in the eastern Mediterranean. The propagation of the faulting offset in seabed sediments is explored using 2D finite element modeling. Abaqus© is used as a numerical platform which allowed the modeling of this complex problem, accounting for nonlinear material behavior with strain softening. Different dip angles and vertical fault displacements up to 10% of the soil layer thickness were considered. The results presented in this thesis include the effect of the relative density of the seabed sands on the extent and magnitude of ground surface deformations. The required bedrock displacement/offset for the rupture to reach the surface and the length and location of the distorted zone are reported. The effects of the overlying soil layer thickness and the width of the faulting breccia zone are also investigated. The results show that loose sand case and larger fault breccia zone widths, and larger soil layer thicknesses result in larger distorted zones and higher bedrock displacements for the fault base rupture to propagate to the surface. At larger relative densities and shallower dip angles, the formation of back-thrust conditions are observed for normal fault case and pop-up structures are observed for reverse fault case at certain bedrock displacements. Based on the parametric analyses and results presented in this paper, observations related to the potential magnitudes and extents of surface deformations for various conditions of seabed densities and thicknesses are provided. These would be of critical need/use in determining likely effects of distortion/loading on pipelines crossing the fault zone.

CONTENTS

ACKNOWLEDGEMENTS..... iii

ABSTRACT..... iv

ILLUSTRATIONS..... vii

TABLES..... xi

Chapter

Page

1. INTRODUCTION 1
   1.1 Introduction 1
   1.2 Thesis Objective and Scope of Work 3
   1.3 Significance of the Proposed Research 4
   1.4 Thesis Organization 5
2. LITERATURE REVIEW 6
   2.1 Fault Propagation Literature Review 6
      2.1.1 Experimental Work 6
      2.1.2 Numerical Work 7
   2.2 Literature Review for Unburied Pipelines Subjected to Seismic Faults 9
   2.3 Literature Review for Buried Pipelines Subjected to Seismic Faults 10
      2.3.1 Analytical Work 10
      2.3.2 Experimental Work: 17
      2.3.3 Finite Element Analyses 20
3. MODEL AND METHOD OF ANALYSIS 39
   3.1 Finite Element Model 39
   3.2 Model Geometry, Mesh, and Boundary Conditions 39

3.3 Soil Constitutive Model 40
3.4 Soil Properties: 48
4. NUMERICAL RESULTS AND DISCUSSION 51
4.1 Introduction: 51
4.2 Effect of Relative Density 51
4.2.1 Ground Surface Deformation Profile 51
4.2.2 Extent and Location of the Shear Surface/Band 58
4.2.3 Bedrock Displacement Required for Rupture to reach the Surface 61
4.2.4 Length and Center of Distorted Zone 63
4.3 Effect of Fault Breccia Thickness 71
4.3.1 Ground Surface Deformation Profile 71
4.3.2 Extent and Location of the Shear Surface/Band 76
4.3.3 Bedrock Displacement Required for Rupture to reach the Surface 77
4.3.4 Length and Center of the distorted zone 78
4.4 Effect of Height of Overlying Soil Layer: 84
4.4.1 Ground Surface Deformation Profile 84
4.4.3 Bedrock Displacement Required for Rupture to reach the Surface 87
4.4.4 Length and Location of Distorted Zone 88
5. CONCLUSIONS AND FURTHER RESEARCH 92
5.1 Introduction 92
5.2 Conclusions 92
5.2.1 Dip Angle and Relative Density: 92
5.2.2 Fault Breccia Thickness: 95
5.2.3 Soil Layer Thickness 96
5.3. Further Research 97
APPENDIX 98
REFERENCES: 117

ILLUSTRATIONS

Figure		Page
2-1	Pipeline Lateral Snaking Deflection (Kershenbaum et al. (2000))……..	9
2-2	Newmark Model and Kennedy's method…….……..…….....	10
2-3	Pipe Analysis Model proposed by Wang and Yeh (1985…….……	11
2-4	Proposed method by Takada (2001) …….…….…….……	12
2-5	Shell model with equivalent boundary condition…….…….……..	13
2-6	Equivalent boundary condition for buried pipelie (Liu et al. (2004)……	14
2-7	Existing Newmark-Hall Model (Duan et al. (2011)) …….……...……...	16
2-8	Elastic Plastic Interaction ((Duan et al. (2011)) …….…….……	16
2-9	Post-test surface condition for moist and dry sand tests (test T-3 and T-11) (Abdoun et al. (2009) …….…….…….…….……..	18
2-10	Discretization of pipeline (Takada et al. (1998)) …….…….……...	21
2-11	The model (Takada et al. (1998)) …….…….…….…….……	22
2-12	Z- shape buckling (Guo et al. (2004)) …….…….…….…….....	23

2-13 Strain distribution of deformed pipe (Guo et al. (2004)) ……. 23

2-14 Schematic drawing of finite element model (Liu et al. (2008)) ……..... 24

2-15 Schematic drawing of finite element model (Liu et al. (2008)) …….. 24

2-16 Effect of wall thickness and Luder's extension on maximum strain of pressurized pipeline (Liu et al. (2008)) ……. 25

2-17 Effect of intersection angle on axial strain for pressurized and non pressurized pipeline (Liu et al. (2008)) ……. 26

2-18 Geometry of the proposed model by Joshi et al. (2011) ……. 27

2-19 Finite Element Model by Zhang et al. (2014)…….. 28

2-20 Deformed Pipeline axial strain contours by continuum model (Odina et al. (2009)) ……. 29

2-21 Finite Element Model by Kokavessis et al. (2006) ……. 30

2-22 Finite Element Model by Kokavessis et al. (2006) ……. 31

2-23 Finite Element Model (Plan View) by Zhao et al.(2010) ……. 32

2-24 Finite Element Model by Vazouras et al. (2010) ……... 33

2-25 Proposed finite element model for buried pipeline (Chaudhary et al. (2013)) 35

2-26 Model after application of strike-slip fault and reverse-fault (Rahman et al. (2015)) ……. 36

2-27 Mises stress distribution and stress change of points A and B (Jiao et al. (2009))… ……. 38

2-28 Finite element model suggested by Vasileiadis et al. (2012) ….....…… 38

3-1	The 2D fault propagation model……..……..……..……...	40
3-2	a)Mohr Coulomb circle in 2D and b) in deviatoric plane (Abaqus documentation)…..……	43
3-3	Yield surface in meridional plane (a) and deviatoric plane (b) (Abaqus documentation)……..	44
3-4	Mohr Coulomb in Meridional plane (Abaqus documentation)…….	45
3-5	Typical variation of stress ratio and volume change with repsect to horizontal displacment in direct shear test for dense Toyoura sand (Shibuya et al. 1997) ……	47
3-6	Reduction of peak friction angle and peak dilation angle with plastic deviatoric strain……..……..……..……..……	48
3-7	Peak Friction Angle and b) dilation angle variation with depth……..	49
4-1	Schematic presentation of the fault rupture procedure and the parameters studied in the following thesis……..……...……..……	52
4-2	Ground surface deformation profile for sand under normal fault……	53
4-3	Plastic shear strains corresponding to the above normal fault cases at a vertical bedrock displacement of 10%H……..……..……..……	53
4-4	Ground surface deformation profiles for reverse fault case…….	58
4-5	Plastic shear strains for reverse fault above cases……..……..…….	58
4-6	Location of shear bands at a)U2=2.75%H &b) 10%H……..……	59
4-7	Critical bedrock displacement for the rupture to reach the surface…….	62
4-8	Normalized Length (L/H) and b) center (C/H) of distorted zone for saturated sand subjected to normal fault (30°, 45°, 60°) for dense, medium dense, and loose sand……..……..……..……	64

4-9 Normalized Length (L/H) and center (C/H) of distorted zone for saturated sand subjected to normal fault for dense, medium dense, and loose sand vs. vertical bedrock displacement……. 67

4-10 Normalized Length (L/H) and center (C/H) of distorted zone for saturated sand subjected to reverse fault for dense, medium dense, and loose sand vs. vertical bedrock displacement……. 69

4-11 Ground surface deformation profile for dense sand layer subjected to normal fault under different fault shearing widths……. 72

4.12 Plastic shear strains for normal fault case under different fault widths…….. 73

4-13 Ground surface deformation profile for dense sand layer subjected to reverse fault under different fault shearing widths. ……. 75

4.14 Plastic shear strains for reverse fault case under differnet dip angles and widths……. 75

4.15 Normalized shear band locations for dense, medium dense, and loose sand for different fault shearing widths vs. the fault dip angle. ……. 77

4-16 Critical bedrock displacement for the shear band to propagate to the surface for dense, medium dense, and loose sand under different fualt widths and dip angles……. 79

4-17 Normalized length and center of distorted zone for dense, medium dense, and loose sand for different fault shearing widths vs. dip angle……. 80

4.18 Normalized length and center of distorted zone for dense, medium dense, and loose sand for normal fault with different fault shearing widths vs. the vertical bedrock displacement……. 82

4.19 Normalized length and center of distorted zone for dense, medium dense, and loose sand for reverse fault with different fault shearing widths vs. the vertical bedrock displacement……. 84

4-20 Normalized ground surface deformation profiles for dense sand subjected to normal fault of dip angles 30° and 45°……. 85

4-21 Normalized length and center of distorted zone for dense, medium dense, and loose sand for normal fault with different fault shearing widths vs. the vertical bedrock displacement…….. 86

4-22 Plastic shear strains for reverse fault case of different dip angles and soil layer thickness……. 87

4-23 Normalized locations of shear bands vs. dip angle for different overlying soil thickness……..……. 88

4-24 Critical bedrock displacement for shear band to reach the surface for different dip angles and soil layer thicknesses……. 90

4-25 Normalized locations of shear bands vs. dip angle for different overlying soil thickness……..…… 91

4-26 Normalized Length and center of distorted zone for different soil layer thicknesses for normal fault case…….…… 92

4-27 Normalized Length and center of distorted zone for different soil layer thicknesses for reverse fault case……..…… 93

TABLES

Table 1 Saturated Sand Properties 49

CHAPTER 1

INTRODUCTION

1.1 Introduction

Historically, earthquakes have caused significant damage to structures, infrastructures, human lives, and the environment. Such damage was observed in the San Fernando Earthquake (1971), Kobe earthquake (1995), Chi-Chi earthquake (1999), Kocaeli earthquake (1999), and the Mid-Nigata earthquake (2004). An earthquake consists of two parts: the seismic waves and the permanent ground deformation. The seismic waves impose threats to structures in areas that lie in the vicinity of, as well as areas that are distant from, the fault as these waves travel long distances. The permanent ground deformation poses danger to overlying structures particularly for cases where the fault deformations propagate to the ground surface.

With the increasing demand on oil and gas, electricity, and other resources, exploration of new offshore resources of oil and gas has generated engineering developments and posed a number of challenges particulat to that environment. As these structures expand over large areas, they are likely to cross through seismic zones. This subjects them to several seismic geohazards like liquefaction, landslides, seismic waves, and permanent ground deformation. Typically, offshore structures are designed to be located away from zones that are susceptible to geoahazard. However, in some cases, whereas exploration and expoitation platforms may be located /designed with such geohazards in ming, the route of offshore pipelines connecting them to the shore and/or other facilties may cross fault zones. This will require special design consideration with

regards to possible fault-induced surface deformations that could affect the structural integrity and stability of the pipelines.

A realistic assessment of the risk imposed by fault rupture to offshore pipelines requires an investigation of the phenomenon of fault propragation through overlying soil deposits under different fault and soil conditions. A thourough literature review that involves experimental, theoretical, and numerical studies on fault propagation (see Chapter 2) indicates that that the fault proprgation mechanism is affected by the type of the fault (strike-slip, normal, or reverse), fault angle, magnitude of fault movement (relative to the thickness of overlying soil), and soil properties (type, density, constitutive model, etc.).

Interestingly, the review of the literature indicates that the majority of the studies targeted the behavior of the pipelines under strike-slip fault conditions with very limited studies that were focused on the cases involving vertical movements produced by normal and reverse faults. Moreover, the majority of the studies related to the response of pipelines to fault displacements or permanent ground deformations considered onshore pipelines with very limited cases involving offshore pipelines. Unlike the case involving onshore pipelines, fault propagation in the offshore environment involves soils that are fully saturated with reduced effective stress conditions that are governed by the submerged unit weight of the soil. Cole et al. (1984) demonstrated that the fault rupture propagation angle is a function of the dilation angle of the soil. Lin et al. (2006) and Bray et al. (1994b) proved that the stiffness and dilation angle of the soil are critical parameters for fault propagation as well. In the presence of water, the effective stresses are reduced to half compared to dry soil conditions. As a result, the friction angle, the dilation angle and the sand stiffness, which are highly dependent on the effective stresses, are expected to be

reduced in comparison to the onshore case, possibly leading to differences in the fault propagation mechanism in the overlying soil.

1.2 Thesis Objective and Scope of Work

Given the significant influence of fault propagation on the economic, environmental, and human losses during an earthquake event, the research work presented herein aimed at investigating the mechanism of fault propagation for the specific case of dip slip faults (normaland reverse) in the offshore environement. The objective was to add to the available literature on the physics of fault propagation, in an attempt to aid the design of offshore pipelines and structures in areas that are susceptible to surface deformations due to fault propagation. In the study, the offshore fault propagation problem was realistically investigated through a numerical finite element analysis that accurately depicted the geometry, boundary conditions, and soil properties, while ensuring that the proper effective stress state iwas properly considered through the incorporation of pore stress-elements.

Unlike other published studies that are generally restricted in their scope to one relative density (Johanson et al. 2007) or limited fault displacements (Loukidis et al. 2009), the analyses in this study targeted fault propagation in saturated offshore sand deposits with different relative densities (dense, medium dense, and loose sand), different dip-slip faults and dip angles (30˚, 45˚, 60˚) for both cases of normal and reversefaulting), and a wide range of fault displacements (1% to 10% of the overlying sand layer thickness). However, the main contribution of the study was in studying the effects of (1) the overlying sand layer thickness (H=20m, 40m, and 80m) and (2) the width of the fault zone or fault breccia thickness which was taken as w=1m, 3m, and 10m. These were considered as the two major

factors that could affect the mechanism of fault propagation to the surface and which have been not adequately investigated by previous researchers.

The presence of fault zones or breccia zones with variable widths or thickesses is a result of crushing that generally accompanies excessive stresses acting on the walls of the fault plane changing the soil intact rock at the fault plane to a fine rock paste that is generally refered to as fault gouge or a course grained rock material denoted as fault breccia. The width of the fault breccia ranges from 0.1m to 100m across the fault plane (Waltham 1994). Fault gouge and breccia zones were observed in several case histories like the Mattinata fault (Brankman et al. 2004), and the Pirgaki and Helike faults in Gulf of Corinth, Greece (Micarelli et al. 2003). Previous investigations on fault propagation considered the fault to rupture within a grain-sized width, which we considered as un-realistic and "limiting". In the work presented in this thesis we aimed at extending published work to include the effect of the width of the brecciated fault zone on the overall fault propagation mechanism.

1.3 Significance of the Proposed Research

With the continued and expanding exploitation of existing/new offshore oil and gas reserves, it is inevitable that such activity will be associated with additional hydrocarbon storage and transport/devliery systems including enxtensive offshore pipeline networks. Given the risk associated with pipeline failures and the resulting environmental and economic losses, it is imperative that these systems be safely designed for all possible loading mechanisms, including thoses associated with faulting which may generate significant movement across/along the deforming crustal boundaries. These movements

maybe be vertical as in the cases explored int his thesis or lateral for strike-slip faulting. In previous earthquakes, pipelines have shown vulnerability to seismic faults where cases of severe damage have been recorded. Some of the examples include the case of the San Fernando earthquake (1971), Chi-Chi (1999), Izmit (1999), Northidge (1994), Hyogoken Nanbu (1995), and Chile (2010) earthquake among others.

The objective of this thesis is to supplement the few studies that were published in the literature on offshore pipelines under permanent ground deformation. The research work presented aimed at investigating the design parameters that alter the response of offshore pipelines under seismic faults and the parameters that effect the resulting ground deformations. The results of the research study may be considered as contributing to enhance the current understanding of the effect of the different soil conditions on the fault propagation mechanism and aid in the design of offshore pipelines.

1.4 Thesis Organization

The thesis is divided into 5 chapters including this introduction. Chapter 2 represents the literature review for experimental and numerical research related to fault propagation as well as analytical, experimental, and numerical work related to investigation of pipeline behavior when subjected to permanent ground deformation. Chapter 3 illustrates the finite element model and the methodology of the thesis work. The chapter includes the corresponding dimensions, boundary conditons, mesh elements, and the constitutive model considered as well as the materials used. Chapter 4 includes the results of the numerical analyses accompanied with a thorough interpretation and discussion of the findings. Conclusions and recommendations based on the thesis work are presented in Chapter 5

CHAPTER 2

LITERATURE REVIEW

2.1 Fault Propagation Literature Review

2.1.1 Experimental Work

There are several studies in the literature that present case histories of fault rupture propagation (Bray et al. (1989), Faccioli et al.(2008), Kelson et al. (2001), Lade et al. (1984), Lin et al. (2006), Bray et al. (1994a), Anastasopoulos (2007b)), Dong et al. (2003)).

From an experimental standpoint, several studies have investigated fault propagation since the 1950s using 1-g small scale tests, as well as centrifuge tests. Sanford et al. (1959), Belousov et al. (1961), Emmons et al. (1969), Horsfield et al. (1977), and Bray et al. (1993) conducted 1g small scale experiments to study the development of the fault movement in overlying soils. Cole et al. (1984) conducted a small scale fault test box experiment to study the fault propagation mechanism on dry, dense and loose, sand under different dip-slip angles, and at low confining pressures. They presented a simple theoretical model to predict the shape and location of the soil rupture surface due to fault movement as a function of soil depth, soil dilation angle, and fault dip-angle. Lade et al. (1984) extended the work of Cole et al. (1984) to predict the location and shape of the additional failure surfaces due to dip-slip faults. Roth el al. (1981) conducted a centrifuge experiment to study fault propagation in alluvial soil. Recently, Bransby et al. (2008a, 2008b) conducted several centrifuge experiments to investigate free field normal and

reverse fault propagation cases and compared them with the case of a strip footing overlying the soil subjected to normal and reverse fault.

Johansson et al. (2004) studied the effect of deformation buildup due to dip-slip faults for dry and saturated sand experimentally. The experiment allowed the modeling of a round fault in 2-D plain strain conditions. The experiments showed that deformations and loads change substantially with the presence of water. The authors concluded that the force to cause rupture is much higher for wet sand than dry sand. Deformations localize at a later stage in the case of wet sand. The deformations were also found to be more inclined.

2.1.2 Numerical Work

Several numerical studies targeted fault propagation as well. Duncan et al. (1973) studied the effect of fault propagation on structures in dry sand. Scott et al. (1974) simulated vertical fault propagation through 800m deep alluvium cohesionless dry soil. Roth et al. (1982) performed a finite difference numerical analysis to study the propagation of a normal fault in dry sand and compared the results with centrifuge test results. Scott et al. (1987), White et al. (1994), Nakai et al. (1995), Loukidis et al. (1999), and Erickson et al. (2001) modeled fault propagation using finite difference methods. Walters et al. (1982) simulated a reverse fault in cohesionless soil using a numerical analysis and proved that strain softening and non-associated flow are essential for modeling fault propagation.

Bray et al. (1994b) conducted a numerical analysis to study dip slip (normal, reverse, and vertical) fault propagation through normally consolidated clay at typical depths of 24m and 91m. He compared the results with clay box experiments and anchor pullout

experiments. Taniyama et al. (2000) performed a sandbox test and a plain strain FEM to investigate reverse fault rupture propagation through sand. Lin et al. (2006) presented a small scale FE model using Abaqus and conducted a small scale sandbox experiment to validate it. They conducted a large scale finite element model. They concluded that the most effective parameters are the flow dilation angle and young's modulus of the soil.

Anastasopoulos et al. (2007) conducted a non-linear finite element analysis to model dip-slip fault propagation in sand. They verified it with 4 centrifuge experiments (on dense and loose sand), and then conducted a parametric study for normal and reverse faults under dip angles of 45˚ and 60˚. They presented charts for the location of fault outcropping, ground surface deformation, and the minimum fault bedrock displacement for the deformation to reach the surface.

Johansson et al. (2007) presented a numerical code incorporating the hypoplastic constitutive model to study the fault propagation in dry and wet sand. The study showed that the soil compressibility should be taken into account in design. They concluded that the shear zones are wider for wet soil especially for the reverse fault case where the incompressibility of the pore water pressure prevents the horizontal compression and results in increased shear strains.

Loukidis et al. (2009) performed a numerical study on the propagation of dip-slip fault through uniform soil using the finite difference code FLAC. For the soil material, they considered dense sand, loose sand, NC clay, and OC clay under different fault dip angles and soil thicknesses. Quasi-static simulations were applied to model the fault under different dip-angles and soil thicknesses. Results for ground surface deformations,

inclinations, the lengths of distorted zone, bedrock displacement required for the fault rupture plane to reach the surface and the location of shear bands were addressed.

2.2 Literature Review for Unburied Pipelines Subjected to Seismic Faults

Kershenbaum et al. (2000) studied analytically the behavior of unburied snaked marine pipelines under seismic faults (strike-slip, normal and reverse (angle=45˚), longitudinal, and oblique) as shown in Figure 2-1. They studied the effect of operating temperature. They concluded that snaking doesn't magnify the longitudinal stress compared to straight pipeline and that the increase in ground displacement doesn't affect the longitudinal and bending stresses of as laid pipelines significantly. They recommended considering all as laid pipelines as snaked.

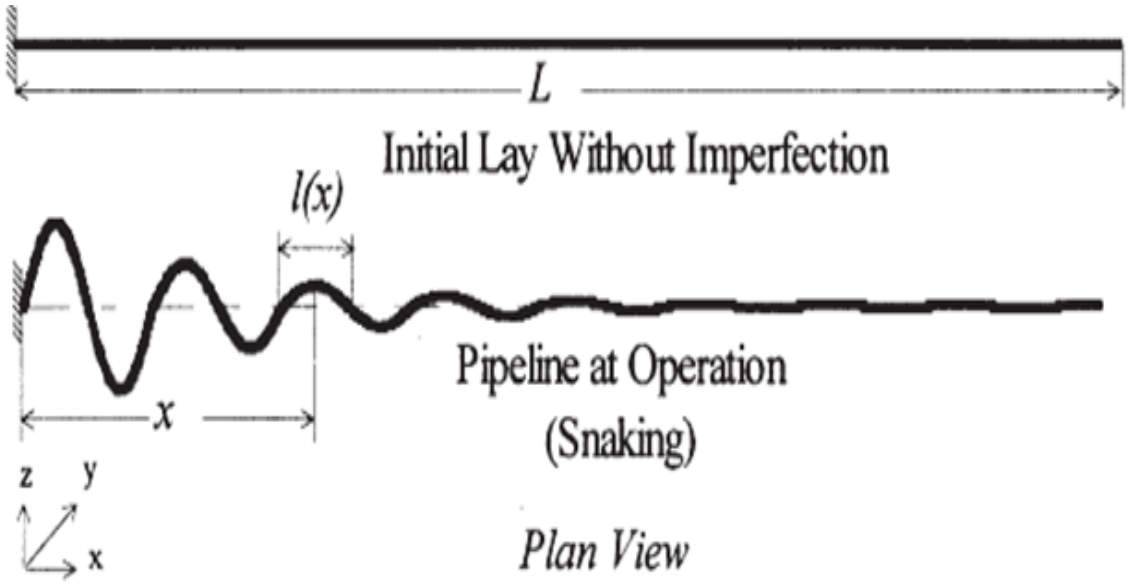

Figure 2-1 Pipeline Lateral Snaking Deflection (Kershenbaum et al. (2000))

2.3 Literature Review for Buried Pipelines Subjected to Seismic Faults

2.3.1 Analytical Work

The earliest analytical studies were done by Newmark and Hall (1975). Newmark represented an analytical method to analyze the pipeline response under strike-slip fault considering that the pipeline is subjected to tension only. They considered the pipeline ends to be fixed by anchors at the 2 sides of the fault. According to Newmark-Hall method the pipeline deforms as a straight line AC (Figure 20-2).

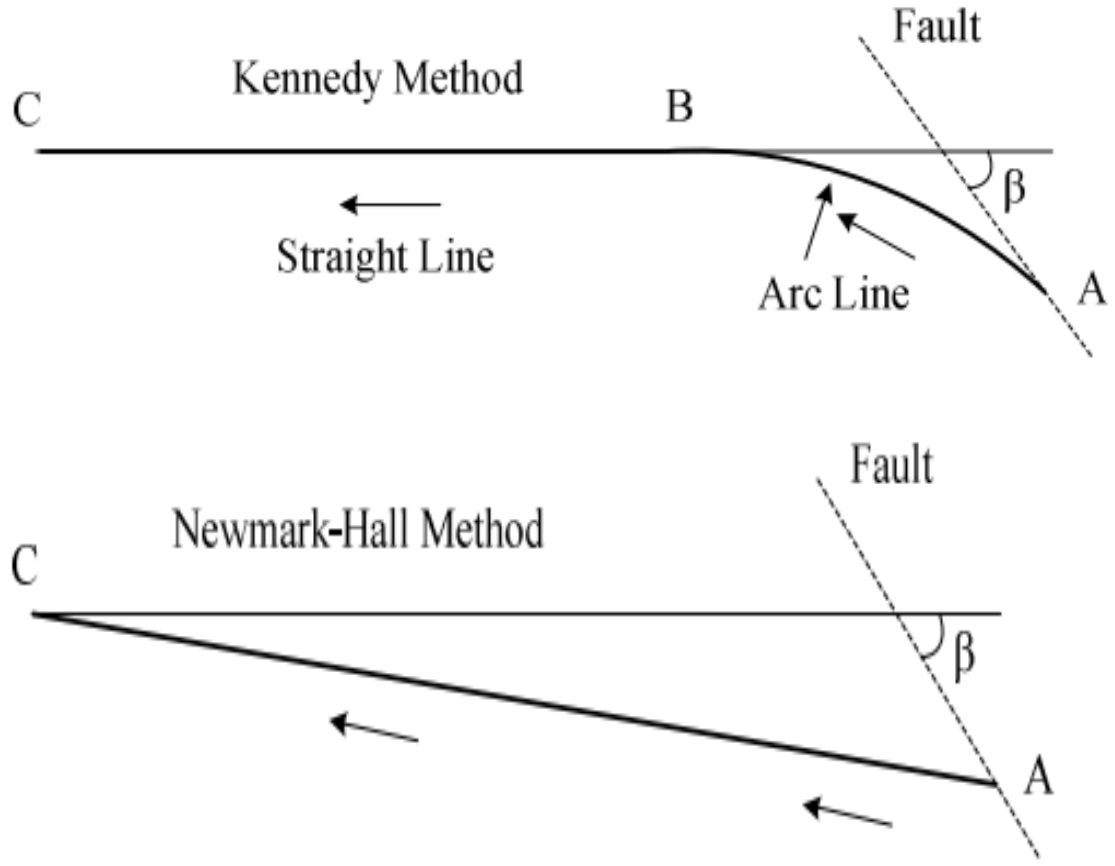

Figure 20-2 Newmark Model and Kennedy's method

Kennedy et al. (1977) extended the Newmark-Hall method to include the effects of large fault displacement (large deformation theory) and considered the effect of lateral earth pressure. They considered pipe-soil interaction in the longitudinal and transverse direction. They assumed the pipeline is a flexible cable deformed into a single constant curvature curve approaching asymptotically to the undeformed portion of the pipeline. They assumed that the high curvature zone of the pipe has undergone yielding ignoring the bending stiffness of the pipeline. Wang et al. (1985) extended the Kennedy method (1977) taking into account the bending stiffness of the pipeline and allowed analyzing the pipeline subjected to direct tension and direct compression. It was based on the assumption of uniaxial bending of the pipeline and it was only applicable to strike slip and reverse strike slip fault motion (figure 2-3).

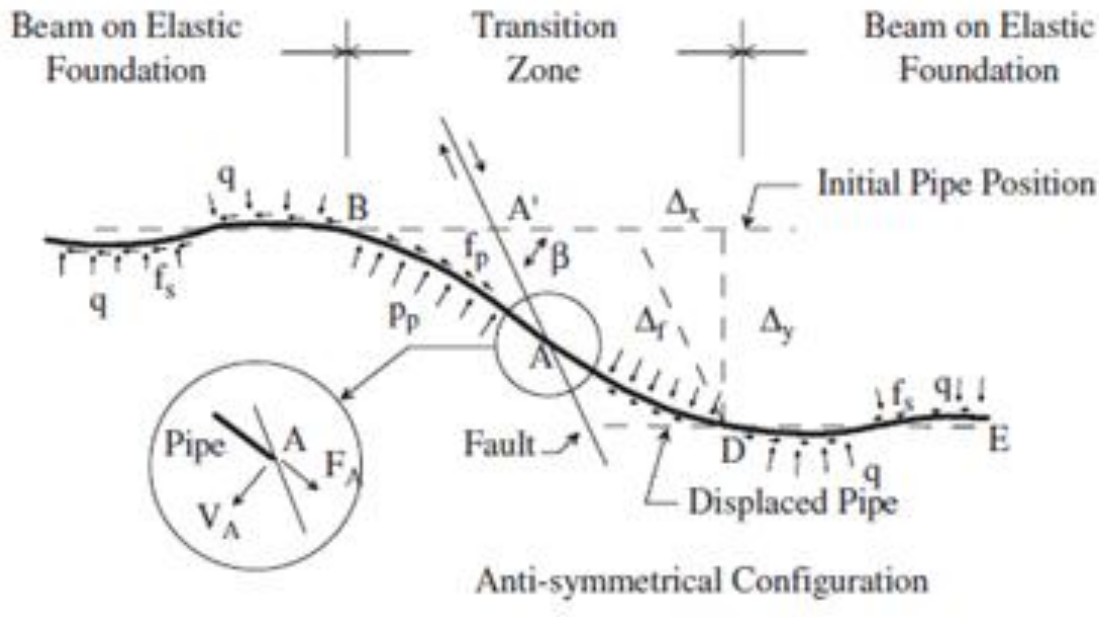

Figure 2-3 Pipe Analysis Model proposed by Wang and Yeh (1985)

Ariman et al. (1991) used shell mode to investigate analytically the tensile and bending behavior of pipeline under fault crossing. The tensions of the fault motion plus an additional extension due to geometric distortion resulting from transverse component of fault motion were investigated. A nonlinear shell theory considering soil effects and a simple flow theory of plasticity was introduced. They concluded that bending strains do not vary at small intersection angles. They conducted a parametric study and concluded that increase in pipe-fault intersection angle, burial depth, soil shearing resistance, and diameter increases bending strains.

Takada et al. (2001) proposed a new analytical method to get the maximum critical strains for a dip-slip fault crossing steel buried pipe including the sectional deformation of the pipeline (Figure 2-4). They related the longitudinal deformation computed from the Kennedy model to the sectional deformation of the pipeline via several shell analyses. They used a hybrid-shell model built in Abaqus that considered shell elements for the pipe in the region undergoing flexure and beam elements for the pipe in the region undergoing axial elongation.

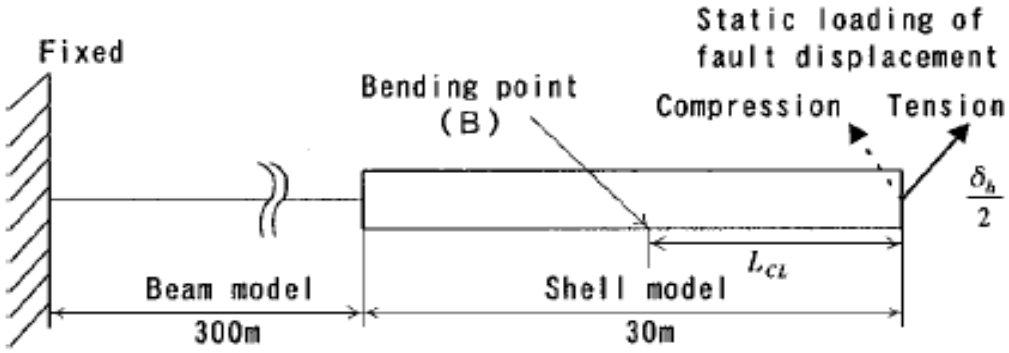

Figure 2-4 Proposed method by Takada et al. (2001)

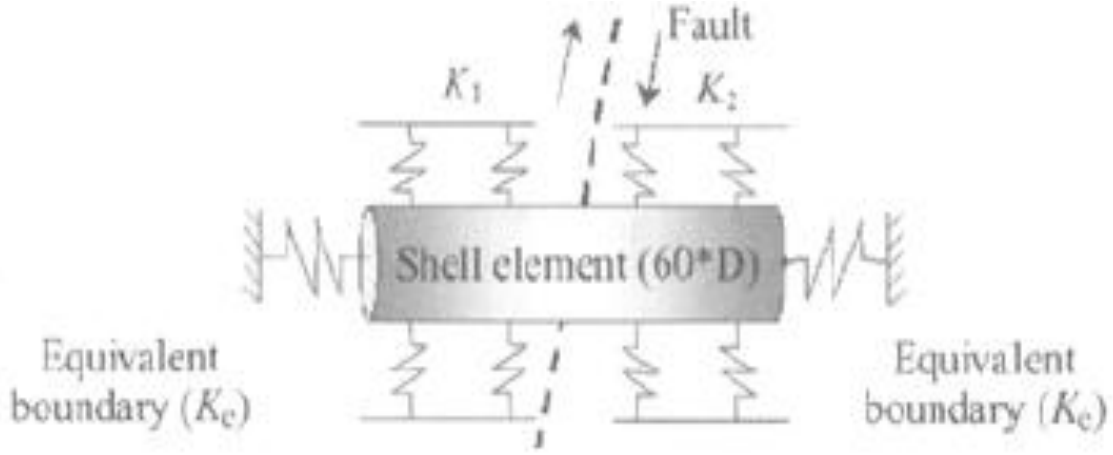

Figure 2-5 Shell model with equivalent boundary condition (Liu et al. (2004))

Liu et al. (2004) introduced an equivalent boundary method for the shell analysis of buried pipeline under large fault movement. In this method only the pipeline segment in the vicinity of the fault was modeled by plastic shell elements to study local buckling and large section deformation of the pipe. Considering the pipe material is elastic elsewhere, non-linear spring elements at equivalent boundaries were applied to the shell ends (**Error! eference source not found.**). The equivalent boundary condition is represented in figure 2-6. They presented an equation for friction force as a function of elongation with imposing conditions on the yield displacement (u_0). These equations are applied at the ends of the shell pipelines as inelastic springs.

Karamitros et al. (2007) introduced a new improved simplified method based on well existing methodologies (Kennedy method (1977) and Wang and Yeh (1985)) for a buried pipeline under strike-slip fault. The method proceeds to locate the most unfavorable combination of axial and bending strains on the curved part and considered the actual stress distribution on the pipeline cross-section to study the effect of curvature on axial strains and

get the maximum design strain. The method applies for pipeline-fault crossing angles <90˚ resulting in pipeline elongation and doesn't account for effects of local buckling and section deformation. This method is limited to allowable strains only.

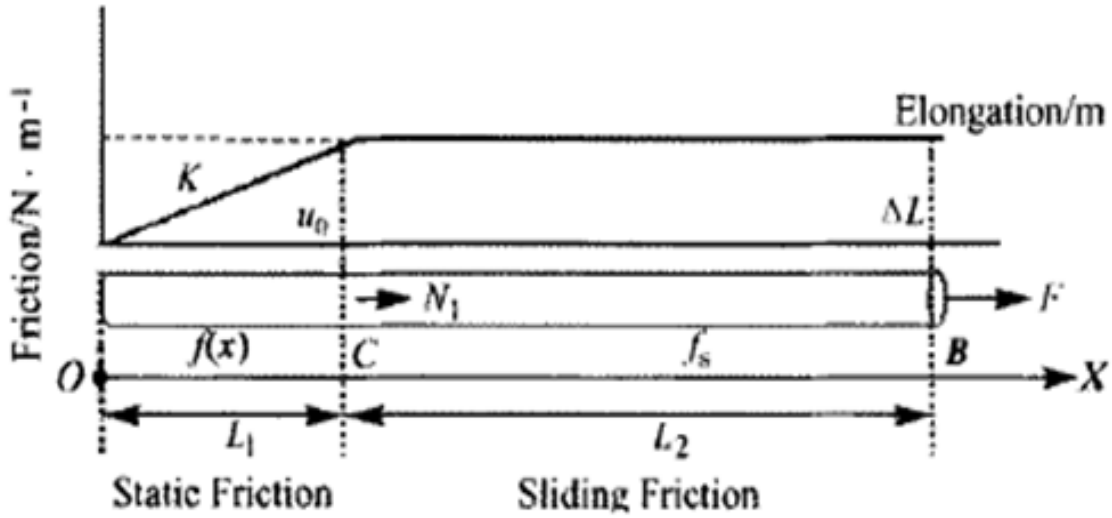

Figure 2-6 Equivalent boundary condition for buried pipeline Liu et al. (2004))

Karamitros et al. (2011) extended the analytical methodology presented by Karamitros et al. (2007) which was limited to strike-slip faults to apply it to normal faults and removed the symmetry. The modifications to the model were explored by a thorough examination of typical results from advanced 3D nonlinear finite element analyses and were then expressed by an easy to apply solution algorithm. By combining the results of this analysis with that for strike-slip fault by Karamitros et al. (2007) the response of pipeline under different pipeline-fault crossing angles can be predicted. As the previous method, this method doesn't extend beyond strain limits and it applies to fault displacements up to 1.25D. This method applies for the cases where tension and bending

are the prevailing modes of deformation, and the pipeline is considered straight and slippage is not restrained along the pipeline unanchored length.

Trifonov et al. (2010) introduced a semi-analytical method for non-linear stress-strain analysis of buried steel pipelines under strike slip-fault and normal slip faults introducing a number of refinements to existing methodologies extending to direct incorporation in design guidelines particularly analyzing fault crossings taking material nonlinearity, large displacement nonlinearity and pipe-soil interaction nonlinearity into account. They introduced the contribution of transverse displacements to the axial elongation.

Trifonov et al. (2012) extended the method presented by Trifonov et al. (2010) to account for service loads. The paper introduced an analytical model for stress-strain analysis of buried steel pipelines due to fault displacement taking into account internal pressure and temperature variation. They included the effect of hoop and axial stresses resulting from temperature and pressure to the combined bending and tension strains due to fault movement.

Duan et al. (2011) represented a new seismic design method for subsea pipelines against seismic faults by modifying the Newmark and Hall method (1975) (figure 2-7) considering elastic-plastic model for pipe-soil interaction (figure 2-8), and the bending stresses which caused the shape of the pipeline not to be straight at the transaction section at the vicinity of the fault. They included the real constraining of the subsea soil on the pipeline, the real elastic-plastic interaction process of subsea soil with pipeline, the plastic slippage of soil, and the elastic-plastic properties of the pipeline materials. The method predicts the length of the transition section of the pipe AB and its total elongation.

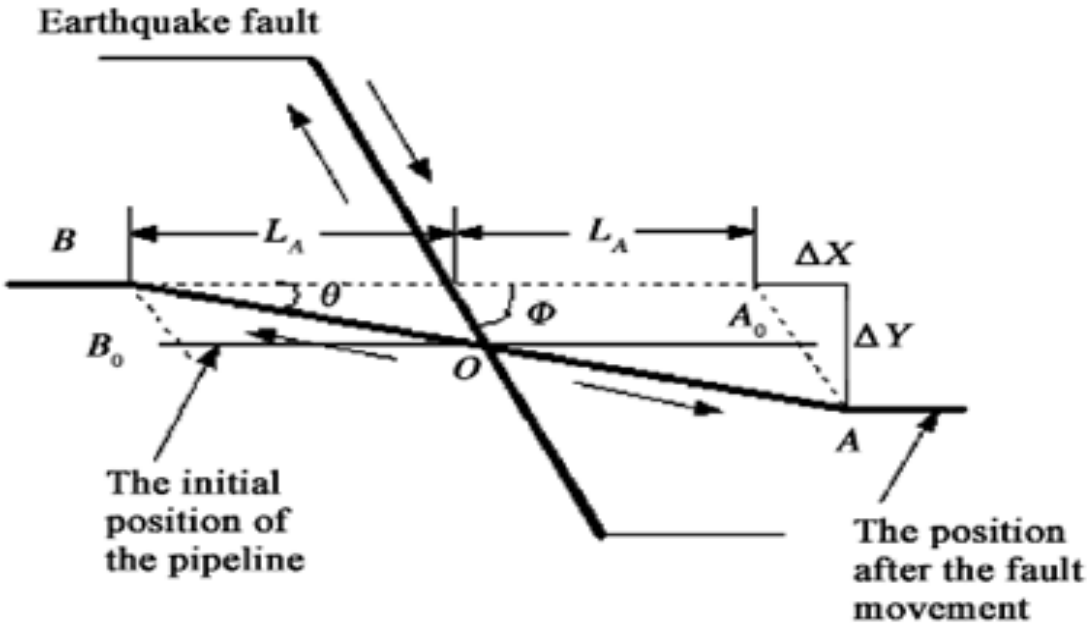

Figure 2-7 Existing Newmark-Hall Model (Duan et al. (2011))

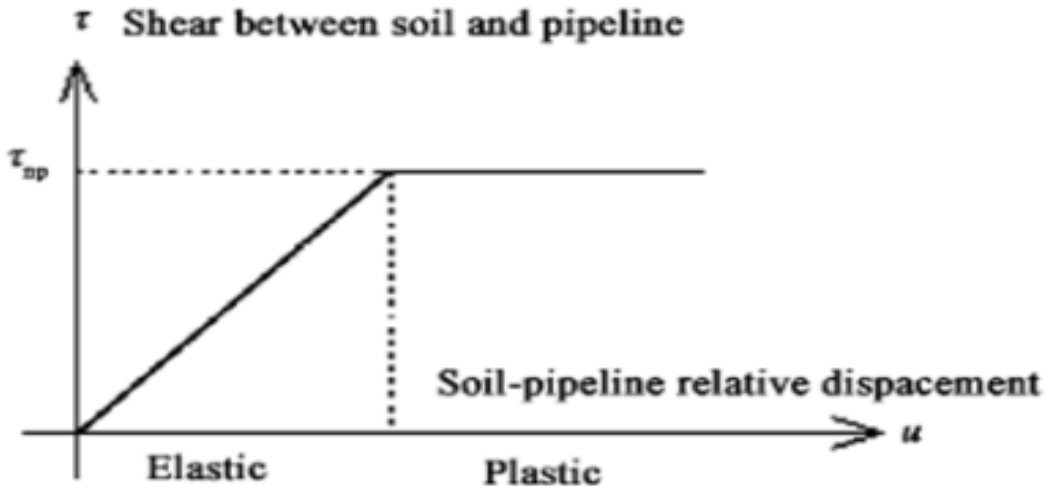

Figure 2-8 Elastic Plastic Interaction ((Duan et al. (2011))

2.3.2 Experimental Work:

O'Rourke et al. (2005) made the first attempt to use centrifuge testing for modeling sand buried pipeline response under fault displacement. They conducted 2 centrifuge tests considering different pipeline diameters and compared the results of axial and bending strains along the pipe with the corresponding finite element analysis models and they agreed at small offset where the pipeline was in the elastic range.

Bransby et al. (2007) conducted 3 centrifuge tests to study the response of buried pipeline (in Fontainebleau sand) subjected to reverse fault of dip angle β=60˚. They represented the results of the maximum hogging and sagging bending strains vs. fault offset. They conducted a parametric study to investigate the effects of cover depth, pipe diameter, and pipe stiffness on the pipeline response due to reverse fault. They concluded that relative pipe-soil rigidity affects the deformation pattern. Pipelines that are flexible relative to the soil are subjected to localized deformation and larger curvatures or bending strains than rigid ones. Shallow pipelines are less susceptible to fault damage than deeper pipelines.

Ha et al. (2008a) conducted centrifuge tests to investigate buried HDPE pipeline behavior subjected to strike-slip fault movement under different pipe-fault crossing angles (-63.5˚, -85˚). The pipes were buried in glacio-fluvial well graded sand with water content 4-5%. They concluded that the pipe axial strains are highly influenced by crossing angle whereas bending strains are less influenced. They produced force displacement relationships of pipe soil interaction for fault offsets less than and greater than 1.5m. The results show that the p-y relationships are stiffer near the fault and softer at points far from the fault. The centrifuge results were compared with the results given by the Kennedy

model and showed good agreement. So the results of the centrifuge were extrapolated to be applied to longer unanchored lengths.

Ha et al. (2008b) conducted 2 centrifuge tests to investigate the response of HDPE pipelines to normal and strike-slip fault. They used the same soil conditions (backfill sand) as Ha et al. (2008a). The results showed symmetric behavior of pipeline under strike slip fault and asymmetric behavior under normal fault for axial strains and pressure distribution at pipe-soil interface. Force displacement relationships (peak force vs. relative displacement) were obtained for both normal and strike slip considering pipe-soil interface friction μ=0.4 and compared with ASCE guidelines where strike-slip fault p-y curves showed good agreement whereas experimental p-y curve for normal fault showed much softer than ASCE guidelines.

Abdoun et al. (2009) conducted 10 centrifuge tests (figure 2-9) to investigate the factors that influence the behavior of HDPE pipelines subjected to strike-slip faulting under pipe-fault crossing angle (α=63.5˚).

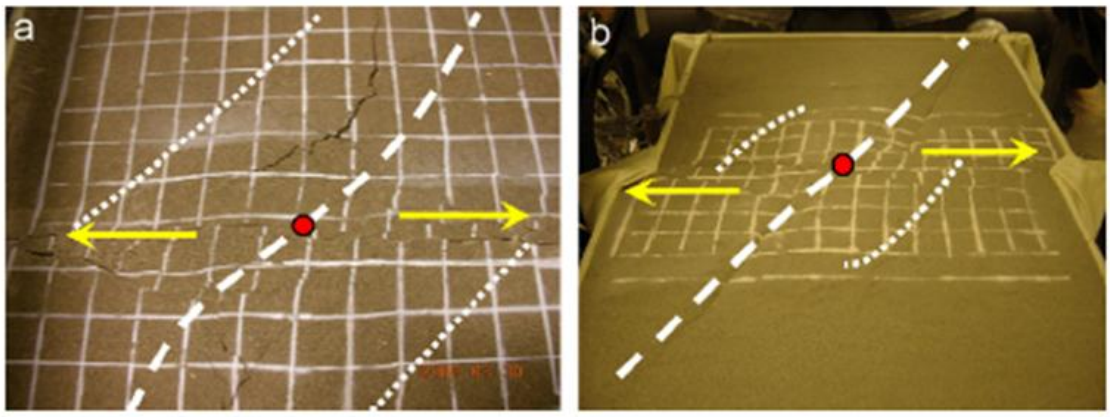

Figure 2-9 Post-test surface condition for moist and dry sand tests (test T-3 and T-11) (Abdoun et al. (2009)

The parameters considered are the soil water content (0 and 4%), the fault offset rate, the relative burial depth (H/D), and pipe diameter (D). They considered the same sand properties as Ha et al. (2008a, 2008b). They represented the axial and bending strains, the peak axial and bending strains vs. fault offset, and the pipe lateral force vs. distance for μ=0.4 under each of these parameters. They concluded that the fault offset rate and soil moisture content do not have a significant effect on magnitudes and locations of peak strains and peak lateral forces on the pipe. The pipe burial depth H/D significanlty affects the magnitudes and locations of peak strains and the pipeline diameter to thickness ratio is an important parameter affecting soil-pipeline interaction.

Moradi at al. (2013) conducted 3 centrifuge tests to investigate the behavior of buried steel pipelines under normal faulting (dip angle=60˚). They used Firoozkooh-191 sand (RD=85%) with moisture content (4-4.5%). They studied the effects of fault offset, burial depth, and pipeline diameter on axial and bending strains, on ground soil failure, pipeline deformation patterns. Tensile rupture due to fault movement is investigated.

Rojhani et al. (2012) conducted 4 centrifuge tests to study the behavior of buried continuous pipelines under reverse faulting (dip angle β=60˚). They used Firoozkooh-191 sand (RD=85%) with moisture content (4-4.5%). They investigated the effects of the following parameters fault offset, burial depth (H), pipe diameter (D) on axial strain and bending strains (center, footwall, hanging side), ground soil failure, and pipeline deformation pattern. The initial strain at the wrinkling point is compared with theoretical values and showed good agreement.

2.3.3 Finite Element Analyses

Takada et al. (1998) studied the shell model response of buried steel pipelines under normal (45 degree) and reverse (45 degree) faults (figure 2-10 and 2-11). They modeled the pipe (diameter D=0.762m, thickness=0.019m, L=30D) using 4 node thin shell elements and considering elastoplastic material behavior.

They modeled the surrounding soil as non-linear springs and concluded that the plastic strains predominate the total strains implying the importance of ductility. They deduced that in the normal fault case, axial tension strains govern and the maximum strain is at fault position whereas in the reverse fault case, axial compressive strains (equal to pipeline hardening strain 5%) govern the pipe behavior and the maximum strain is at buckling position. They concluded that pipelines are more vulnerable to reverse movements than normal. By comparing the allowable fault displacement of the shell model with those predicted by analytical models, different results were given for the reverse fault case. They recommended conducting shell mode analysis because beam models can't capture buckling. They also concluded a parametric study on the soil stiffness, fault type (normal or reverse), fault slip angle (30˚, 45˚, 60˚, 90˚), and diameter to thickness ratio.

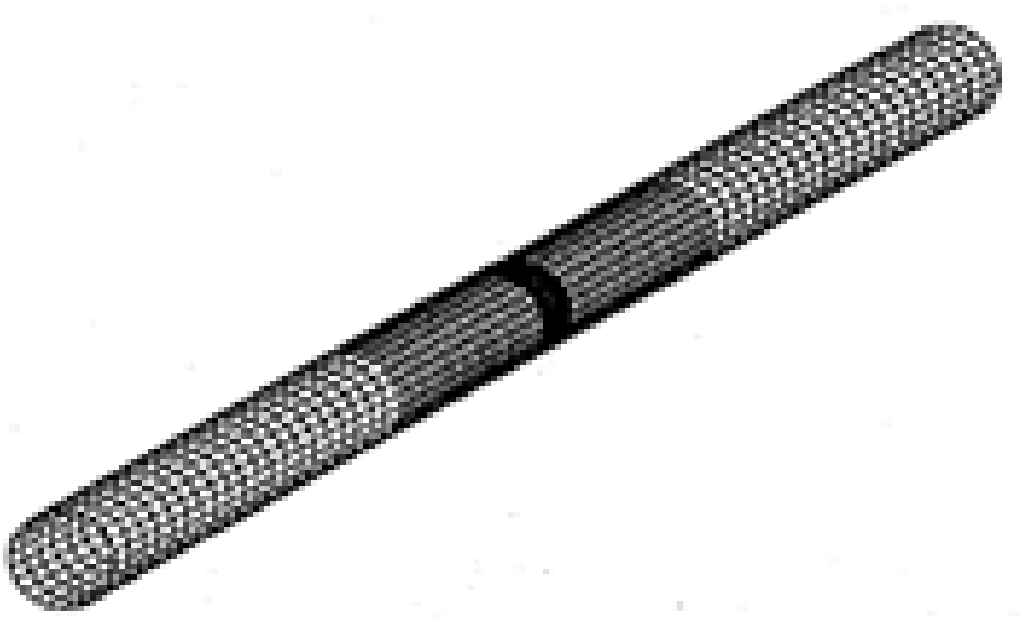

Figure 2-10 Discretization of pipeline (Takada et al. (1998))

Results indicated that the soil stiffness is very important. As the soil stiffness increases, the allowable fault displacement decreases and the buckling position for the case of reverse fault moves towards the fault plane. For the fault slip angle, in the normal fault case, a small angle is better for the pipe and 60 degrees is the most dangerous; whereas for the reverse fault, 45 degrees is the most favorable and 60 degrees is the most serious. As the D/t ratio increases, the allowable fault displacement decreases, so they recommended thicker pipelines.

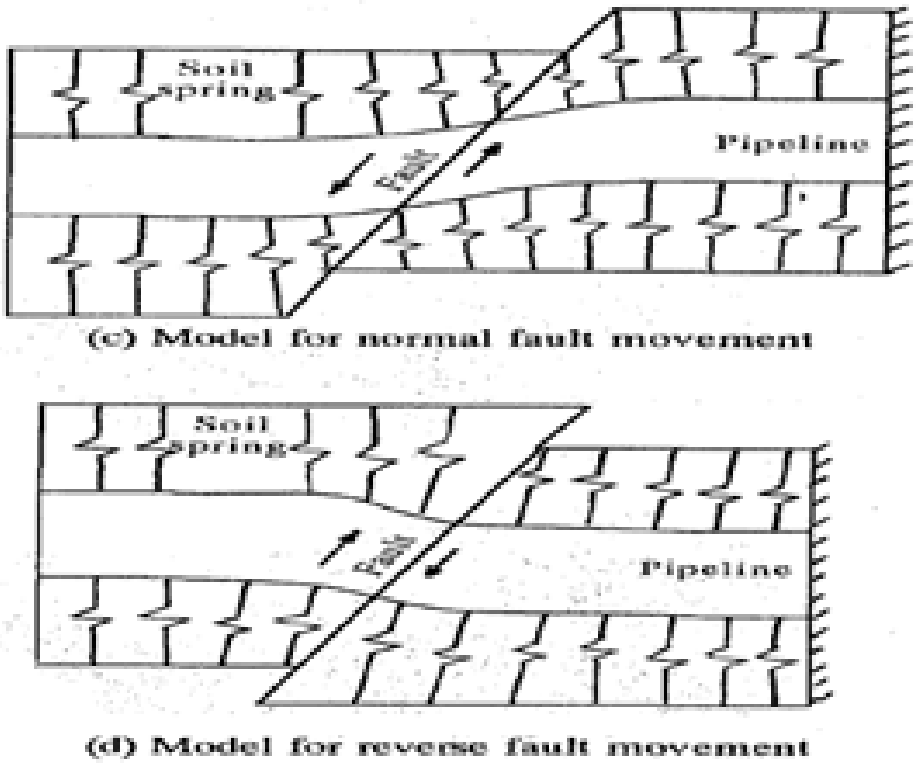

Figure 2-11 The model (Takada et al. (1998))

Guo et al. (2004) applied non-linear finite element analysis to study steel pipeline rupture under which has been damaged near Qinghai-Xinjiang border by the strike slip with reverse dip under earthquake of magnitude Ms=8.1 (revise sentence… not clear). They constructed a 3D finite element model using ANSYS software. They modeled the pipeline as a 3D shell and the surrounding soil by spring elements. They conducted this analysis to find the main features of damage of the pipeline. They represented the strain distributions (Figure 2-13) on the deformed shape of the pipeline and the buckling shape. A Z-shape was observed (figure 2-12) and the buckling position was in agreement with the post-earthquake investigation.

The authors also conducted a parametric study on the pipe material property (initial elasticity modulus), soil stiffness (initial modulus of elasticity of the soil), pipe diameter, and fault dip angle of the normal and reverse faults on the maximum pipe strains. They recommended using larger diameter pipelines with thicker walls, burying pipelines in softer fill, using pipelines with higher strength, and adjusting the pipeline direction to avoid the compressive state.

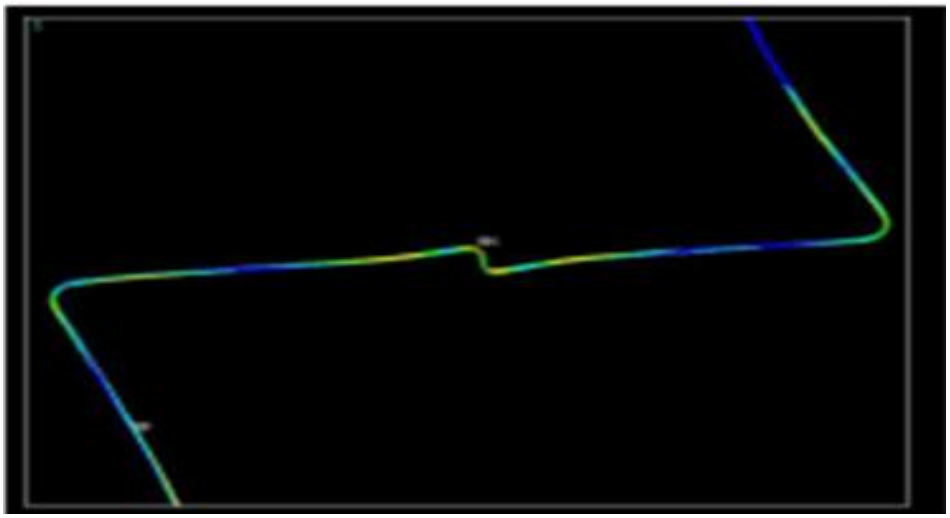

Figure 2-12 Z- shape buckling (Guo et al. (2004))

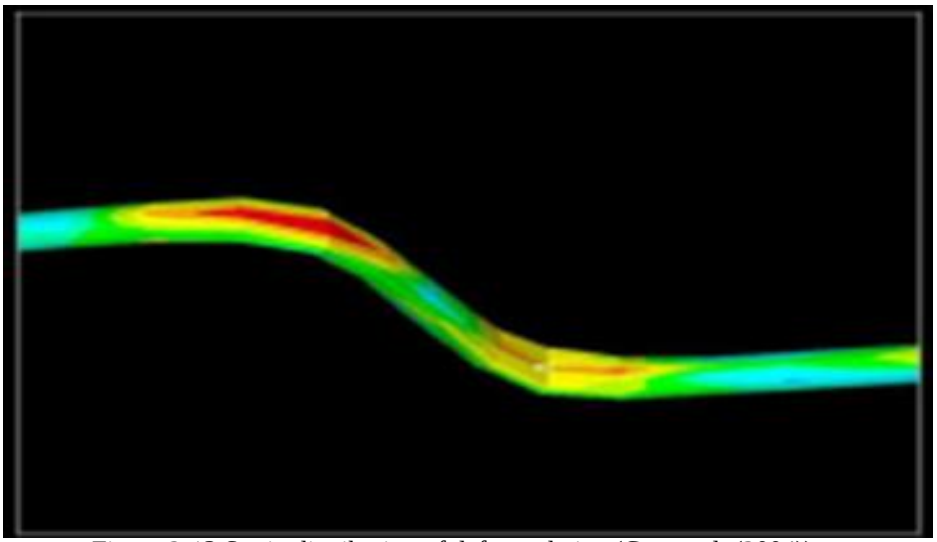

Figure 2-13 Strain distribution of deformed pipe (Guo et al. (2004))

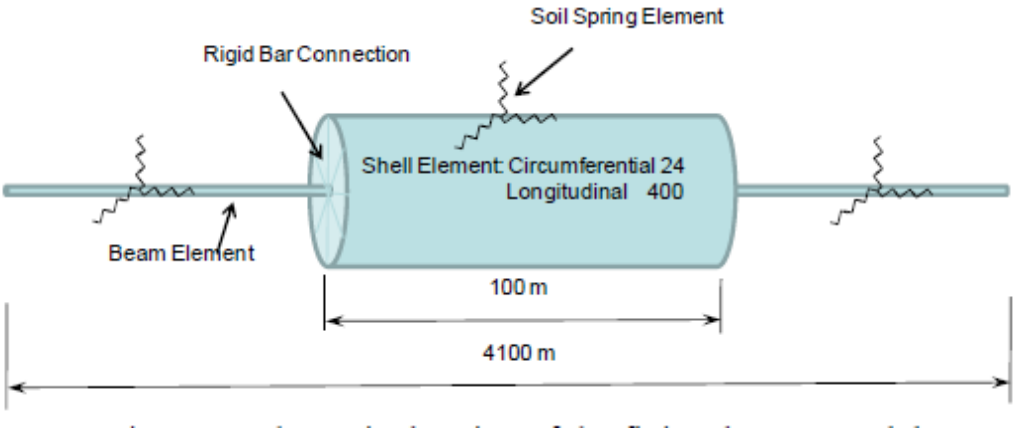

Figure 2-14 Schematic drawing of finite element model (Liu et al. (2008))

Liu et al. (2008) investigated the axial tensile and compressive strains of buried pipelines under oblique fault crossing by a 3D FEM using Abaqus and the factors affecting the strain. They modeled the pipe with shell elements near the fault crossing and beam elements elsewhere using true material properties (figure2-14).

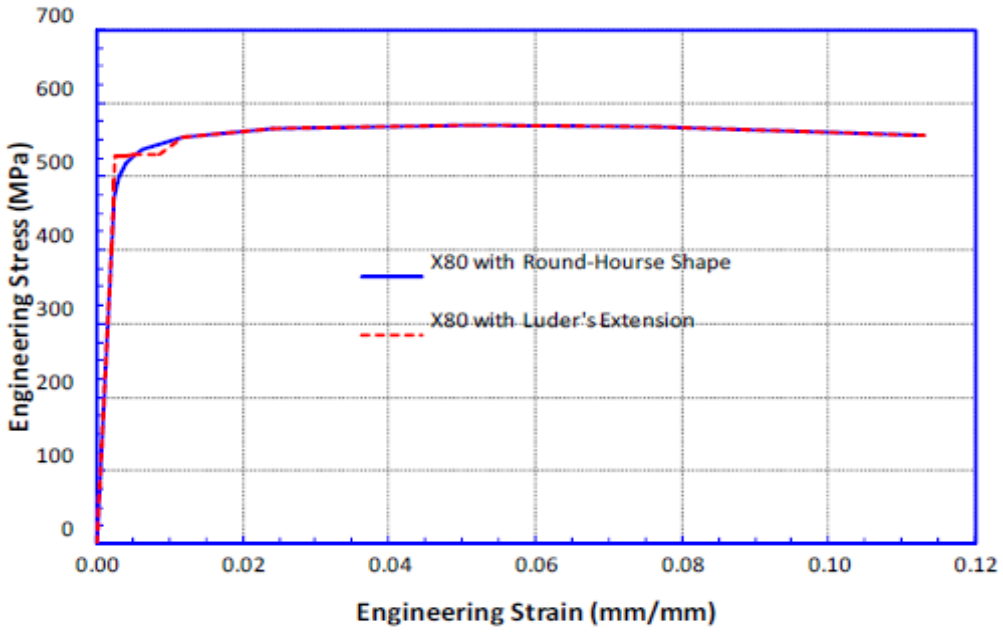

Figure 2-15 Stress strain curve of grade X80 steel with and without Luder's Extension (Liu et al. (2008))

The pipe soil interaction was modeled with soil-spring elements based on the ALA-ASCE Guidelines (2001). They considered that coating can alter the material stress-strain response and related the maximum strain to the pipe-fault intersection angle. They investigated the effects of material properties (with and without Luder's Extension (figures 2-15, 2-16, and 2-17) and wall thickness (22mm and 26mm), and internal pressure (P=0, 12Mpa) on maximum axial tensile and compressive strains vs. intersection angle.

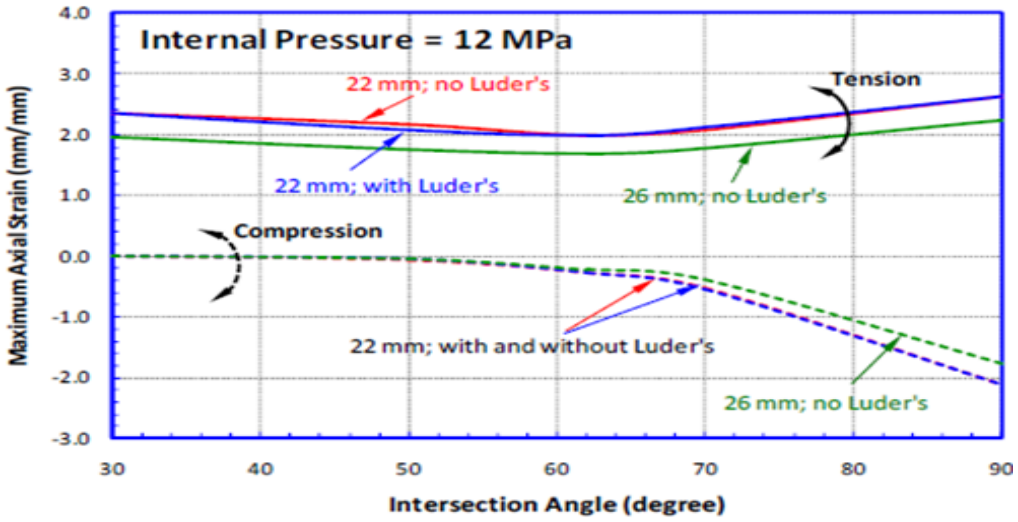

Figure 2-15 Effect of wall thickness and Luder's extension on maximum strain of pressurized pipeline (Liu et al. (2008))

The authors concluded that fault movement creates localized strains at early stages of loading and the location of the strain localizations depends on the loading mode. They also concluded that tensile strains are formed at low intersection angles at the region of the fault. As the intersection angle increases the loading module changes to bending and the localization of the strain moves away from the fault. For a 3D fault movement, there exists a crossing angle where maximum tensile axial strain is minimum. The maximum

compressive strain is at 90 degrees intersection angle and pipe internal pressure increases the compressive strain and it increases or decreases tensile strain according to pipe-fault crossing angle.

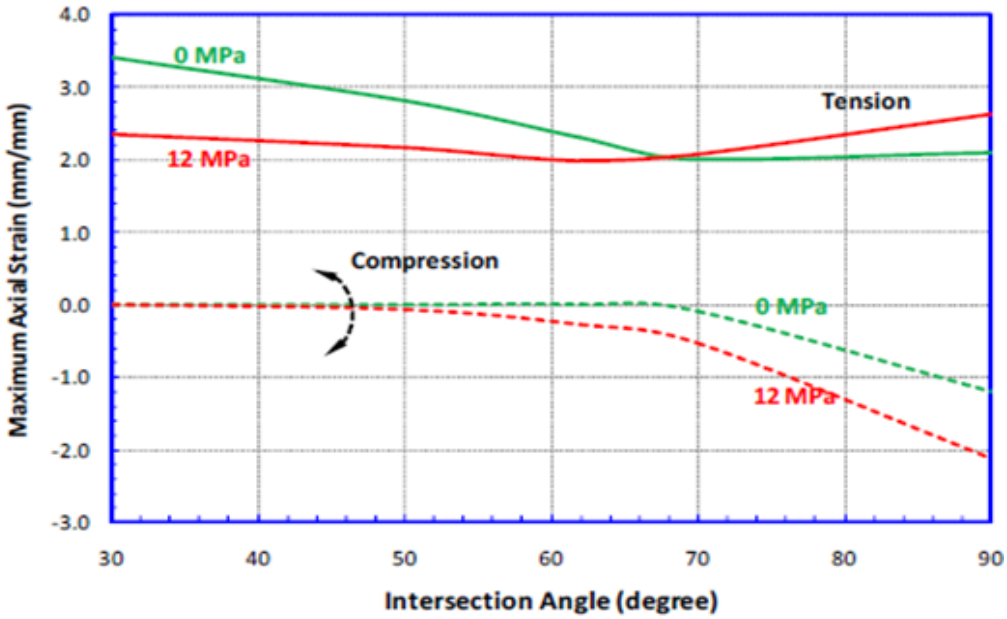

Figure 2-16 Effect of intersection angle on axial strain for pressurized and non pressurized pipeline (Liu et al. (2008))

Joshi et al. (2011) proposed a simple 3D FEM (figure 2-18**Error! Reference ource not found.**) to analyze buried pipeline behavior under reverse fault using 3-D beam elements for pipe and nonlinear soil springs for the soil. They considered nonlinear material for the pipe associated with a bilinear stress-strain curve and pipe soil interaction by associating soil springs to each pipe node and soil material non-linearity was modeled by elastic-perfectly plastic force deformation curves for each spring.

Complex 3D reverse fault motion was applied to the fault by applying fault offset to the free ends of soil springs at half length of the pipeline in a quasi-static mode using

Abaqus explicit solver. Nonlinear geometry was considered and buckling positions were predicted on regions of maximum compressive strain while beam buckling was captured in the simulation. Pipe-soil interaction was modeled by connecting each pipe node to 3 mutually nonlinear springs.

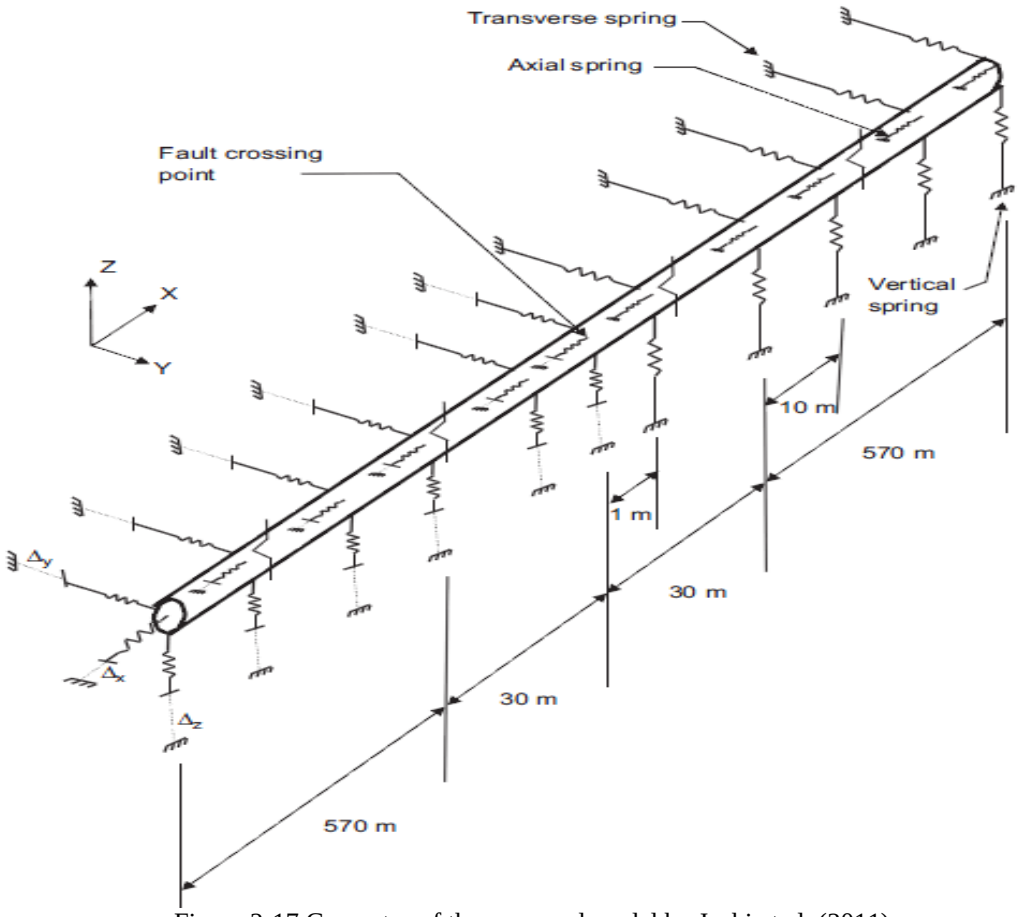

Figure 2-17 Geometry of the proposed model by Joshi et al. (2011)

A parametric study was conducted to investigate the effect of fault offset, pipeline crossing angle, fault dip-angle, native and backfill soil type, burial depth, pipe diameter and thickness, pipe material, and pipe surface characteristics on the maximum compressive strains. The internal pressure was ignored in this study.

The authors found that for pipelines subjected to reverse faults, the compressive strains are more critical than tensile strains. They stressed the necessity of using near parallel orientation of pipeline to the fault, choosing loose backfill, smooth or hard coating, and shallow burial. Pipelines are expected to fail in beam buckling at normal orientations.

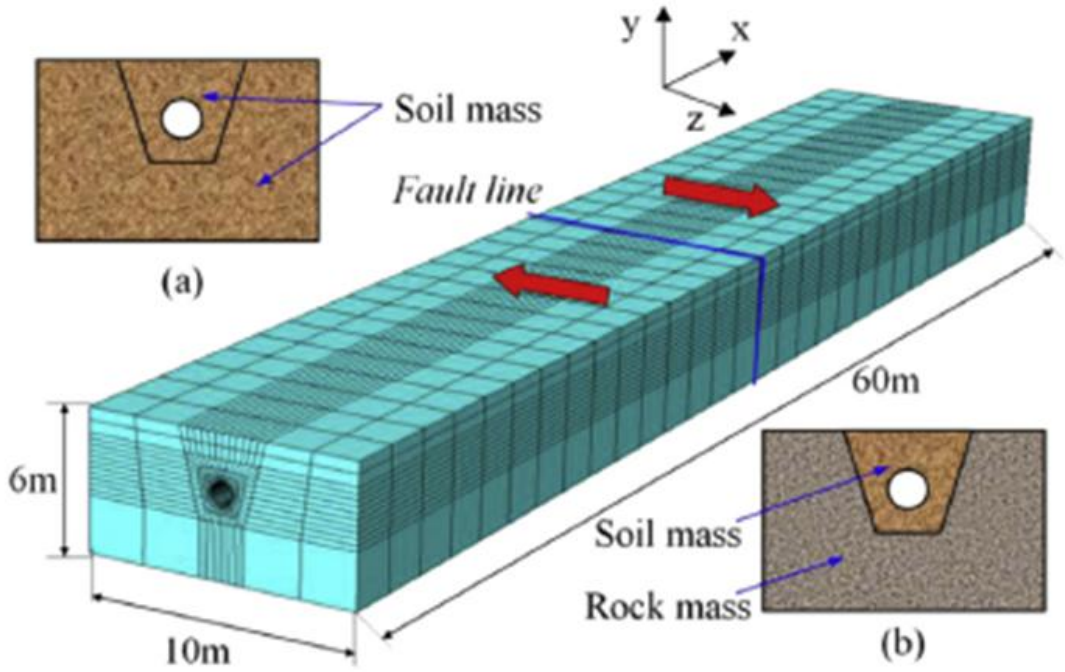

Figure 2-18 Finite Element Model by Zhang et al. (2014)

Zhang et al. (2014) studied the buckling behavior of buried gas pressurized and unpressurized pipelines under strike-slip fault by 3D FEM using Abaqus for buried steel pipelines buried in rock mass layer and soil mass layer (figure 2-19) . The pipeline is modeled with (S4R) shell elements and the soil with (C3D8R) brick elements. For steel pipelines, the large-strain elasticity model with isotropic hardening is considered. For the soil, the elastic-perfectly plastic Mohr-Coulomb model is considered. A contact algorithm is considered taking interface friction (μ=0.5) into account and allowing separation between

the pipeline and the soil. They studied the effects of internal pressure, diameter to thickness ratio, and fault displacement on buckling response (buckling position, buckling shape, buckling mode (wrinkling, local collapse, squishing..) and axial strain of the buried pipe.

Odina et al. (2009) discussed the application of continuum method instead of Winkler soil springs for modeling coupled pipeline-seabed (clay) interaction under fault movement which turned to be very conservative. They compared 2 models, the first using beam elements with winkler springs and the other using continuum elements (figure 2-20).

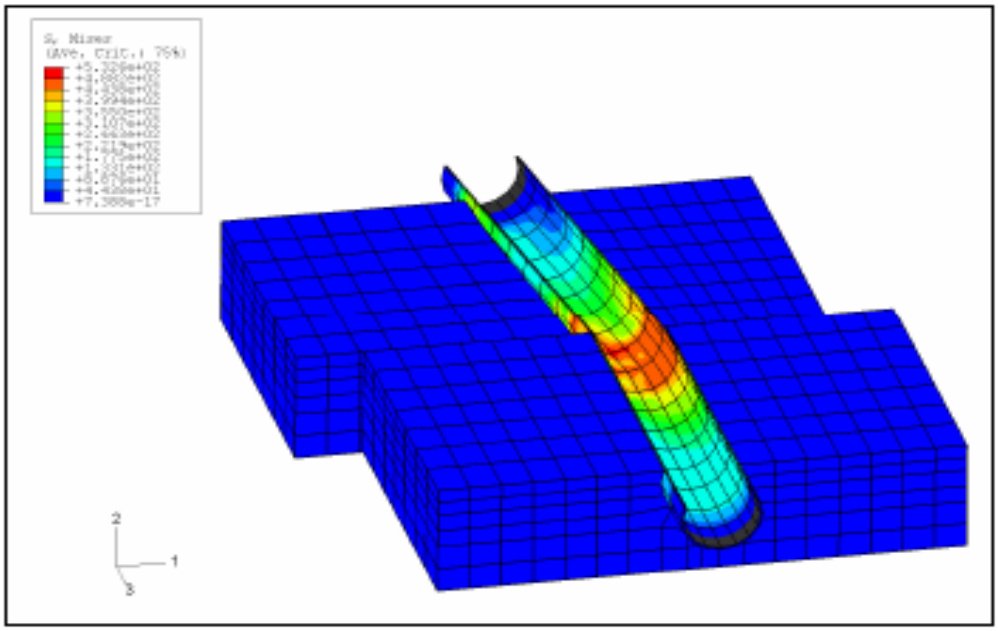

Figure 2-19 Deformed Pipeline axial strain contours by continuum model (Odina et al. (2009))

They constructed 2 models using Abaqus. The first model uses Winkler methodology and the other uses continuum approach under strike-slip fault movement and compared their corresponding results of axial strain and found that Winkler models predict strain values less than those predicted by continuum models. The authors recommended using the

Winkler models in preliminary design stages and rerouting only and then discussed the advantages and disadvantages of each model and concluded that Winkler springs need to be updated.

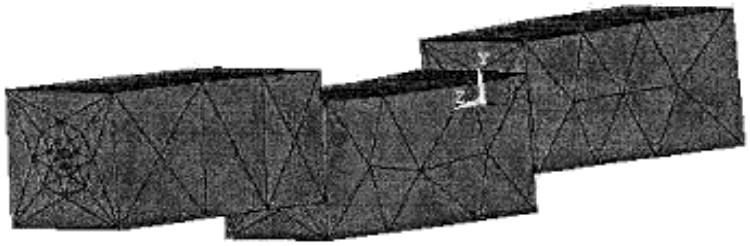

Figure 2-20 Finite Element Model by Kokavessis et al. (2006)

Kokavessis et al. (2006) reviewed the analytical stress methods of buried steel pipelines subjected to seismic loads and proposed the use of contact elements to model pipe-soil interaction. They introduced a 3D FEM using ANSYS software on a pressurized pipeline and used linear elastic material for the pipeline and the soil (figures 2-21 and 2-22). His model results agreed with analytical methods in the literature. They recommended the use of contact elements between the pipe and soil because it allows the imposed loads to follow the pipe as the pipe deforms which is not a feature of using spring elements. They explained that this method allows transmittal of forces from the soil to the outside diameter of the pipeline.

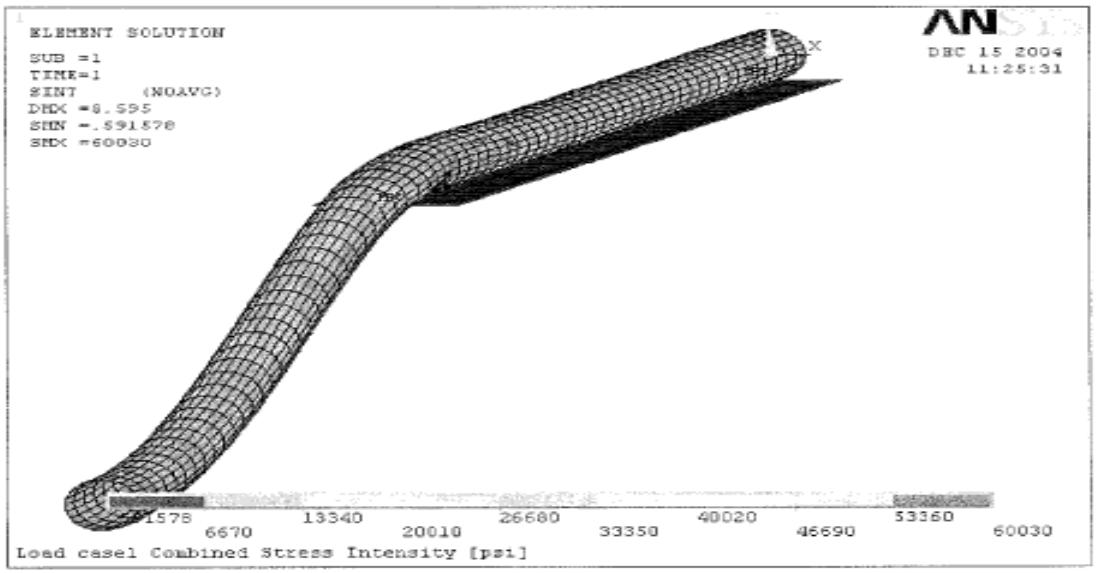

Figure 2-22 Deformed Pipeline axial strain contours by continuum model by Kokavessis et al. (2006)

Zhao et al. (2010) conducted a 3D finite element non-linear model in ANSYS software (figure 2-23) using contact elements to investigate the influence of the rupture mode (dip angle), the thickness (B=23,33m), and rigidity of overlying soil (represented by young's modulus or shear wave velocity) on the response of buried steel pipeline (X60 steel, L=200m, D=1m, t=0.001m). The pipe was modeled by shell elements, the soil by continuum elements, and the pipe-soil interaction was assumed to have non-linear behavior. The boundary of the pipe in the moving block is constrained by equivalent spring according to Liu(2002).

Fault displacement is applied slowly by Pseudo-dynamic method. The soil (sand and clay) constitutive relation is represented by a hyperbola function and the failure value of soil corresponds to 0.03m deformation. The Ramberg Osgood model is used to define the constitutive relation for steel pipeline.

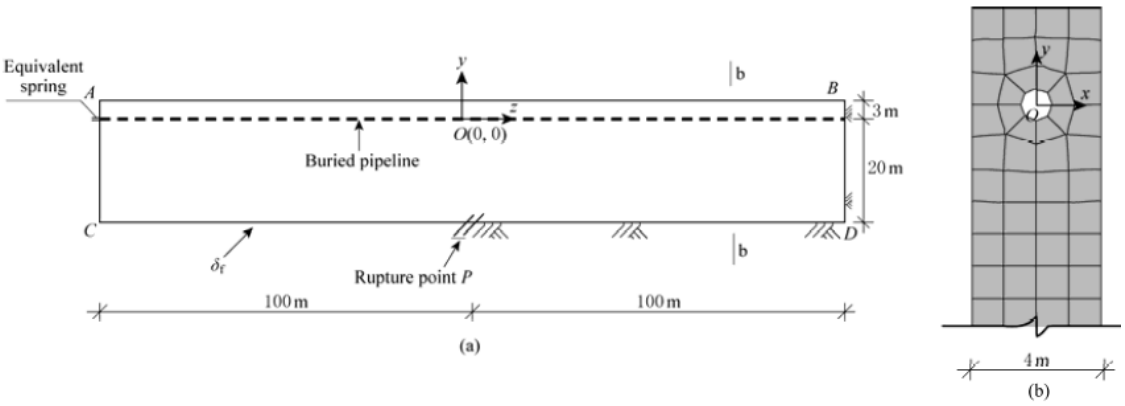

Figure 2-21 Finite Element Model (Plan View) by Zhao et al.(2010)

The authors concluded that the soil rupture mode or dip angle determines the location of the large plastic deformation of the pipeline and the extreme section of the pipe occurs follows the trace of the rupture and the large plastic deformation of rupture of overlying soil. For a fault dip angle of 90, the rupture trace is like letter "y" and 2 sections of plastic deformation appear at the intersection of the pipe and rupture trace "y" of soil. For a dip angle of 45, the rupture trace is an inclined line and one section of plastic deformation appears.

For a thicker soil layer, the plastic deformation section length is bigger and the maximum strains are lower. When the deformation appears in the soil, it also appears in the pipe and its strain value is determined by the strain value of soil. For higher rigidity of soil represented by shear wave velocity, the rupture angle is larger and therefore the rupture area is narrower and vice-versa. The positions of extreme strains are at the intersection of soil rupture trace and pipeline. The plastic deformation area in rigid soil is shorter and its maximum strains are higher.

Vazouras et al. (2010) incorporated a 3D finite element model using continuum elements (figure 2-24) to study the mechanical response of buried steel pipelines under strike-slip fault perpendicular to the pipeline direction in cohesive (soft and stiff clay) and non-cohesive soils (loose and dense sand).

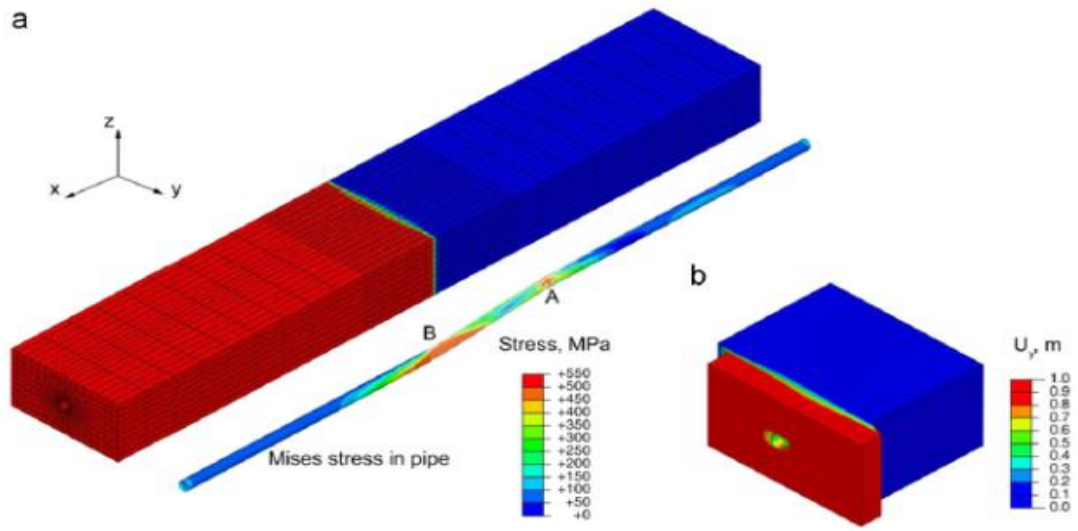

Figure 2-22 Finite Element Model by Vazouras et al. (2010)

Using Abaqus, they used 8-node reduced integration brick elements (C3D8R) to model the soil and 4-node reduced integration shell elements (S4R) to model the pipeline. Gravity loading is applied first and then fault movement is applied by displacement controlled loading. Elastic-plastic material behavior is considered for the steel pipeline with isotropic hardening calibrated by uniaxial stress-strain curve. An elastic perfectly plastic Mohr Coulomb model is employed for the soil. They considered surface-to-surface contact at pipeline-soil interface with a friction coefficient of μ=0.3 allowing separation between pipeline and soil. They noted that varying the friction coefficient between 0.2 and 0.4, the friction coefficient had a small effect on numerical results.

The authors also conducted an extensive parametric study on different soil and pipeline properties with particular emphasis on identifying the pipeline wall failure (wrinkling/local buckling or rupture). The soil factors considered are the soil shear strength, soil stiffness, horizontal fault displacement (20 to 100cm), width of fault slip zone (0.33m to 1m)(minor effect). The pipe property factors considered are the D/t ratio (40 to 140) and the steel material (API5L grades X65 (with and without hardening-no effect) and X80 (UOE and seamless)). They studied the effect of internal pressure (p=0, 0.28pmax, 0.56pmax) as well.

For each case of soil conditions the shape of deformed pipeline is obtained showing the wall failure as wrinkling (local buckling) or rupture. Then numerical results are represented by graphs of axial strains (at both compression side and tension side) vs. distance under different combinations of parameters. Most of the cases showed the formation of local buckling due to excessive compressive strains as the governing mode of failure.

The results indicated that loose sand and soft clay result in large deformation capacity of pipeline associated with lower critical fault displacement value than dense and stiff clay. The fault width has no significant effect on pipeline response. Internal pressures result in small decreases in deformation capacity due to early yielding of steel material. Diagrams for critical fault displacement and corresponding critical strains vs. D/t ratios under different parameter combinations are represented to be used for design purposes. The numerical results of critical strains are compared with provisions of ASCE MOP 119 AND EN-1998-4.

The authors concluded that X80 grade steel has greater deformation capacity than X65 grade steel. Cold UOE X80 pipelines exhibit better behavior against buckling than seamless X80 pipelines due to strain hardening. Thick-walled pipelines do not exhibit buckling; failure may be due to wall fracture as a result of high tensile strains. An analytical method is presented to illustrate this “no-buckling” behavior.

Chaudhary et al. (2013) investigated numerically using 3D models (figure 2-25) the performance of buried pipeline subjected fault motion using MATLAB by implementing displacement controlled arc-length technique to solve non-linear behavior. They compared his model with a 3D ANSYS finite element model. They considered both nonlinear geometry and nonlinear material behavior for the pipe and the soil. The hyperbolic model was employed for the soil (sand with E=50Mpa and ν=0.3) and nonlinear elastic-plastic material was employed for the pipe (API 5L X65, diameter =900mm). 0.5m long meshes were used at the vicinity of the fault, whereas 1m long meshes were used elsewhere. Near the pipe, a fine mesh was applied to the soil. The authors concluded that compression failure crucially depends on wall thickness.

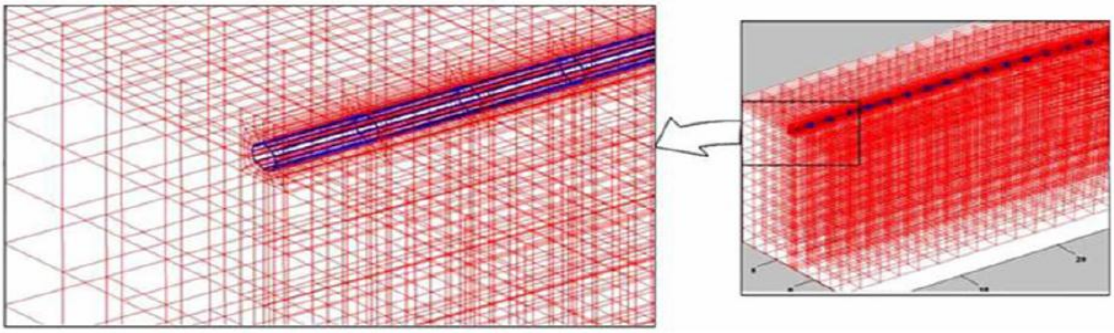

Figure 2-23 Proposed finite element model for buried pipeline (Chaudhary et al. (2013))

They conducted a parametric study on the effect of fault offset, pipeline fault intersection angle, wall thickness to diameter ratio, effect of burial depth on total strain along the pipeline for the case of strike-slip fault. They concluded that compression failure is catastrophic and leads to sudden buckling which depends on pipeline thickness. The effect of direct and bending strains is significant in case of strike-slip fault.

Rahman et al. (2015) simulated the dynamic behavior of buried pipeline (D=150mm, D/t=30) under strike-slip and reverse fault motion using a DEM and FEM analysis (figure 2-26) using a numerical code written in C language.

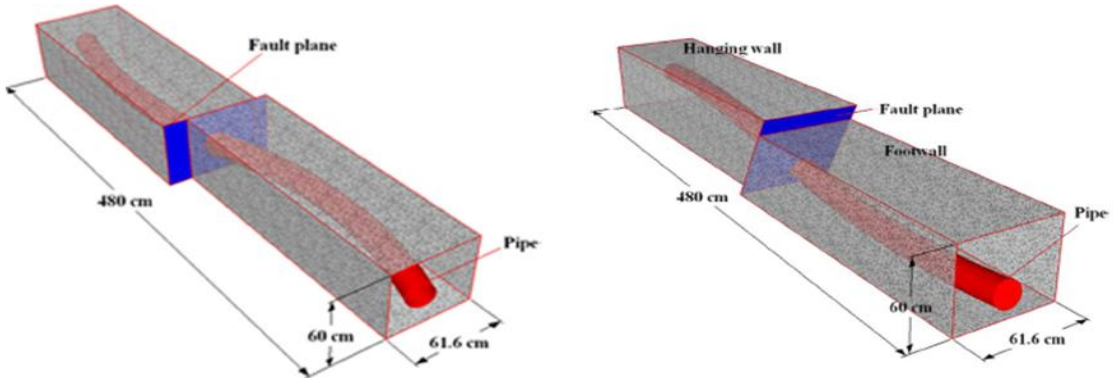

Figure 2-24 Model after application of strike-slip fault and reverse-fault (Rahman et al. (2015))

The soil was modeled by DEM considering 1.8 million spherical particles (each of D=1.1cm) whereas the pipe was modeled as a hollow cylinder using 3D beam elements and was considered elastic. The pipe is buried at shallow depth and the dynamic response of the pipeline (acceleration, velocity, and displacement) to the fault movement is analyzed by FEM.

The deformation response of the pipeline, the force response between the pipe and the soil, and force-displacement relations at different points on the pipe under different fault displacements were presented. It is shown that particles near the fault yield earlier than particles far from fault. The force response increases gradually with distance from rupture point, confirming critical points near the fault. The f-d curve shows the force increases with displacement and then enters a residual state after yielding of particles.

A parametric study is conducted to get the maximum axial strain, the pipe deformation, and the f-d relationships for different pipe materials (Steel, PVC, HDPE, and concrete) under same pipe dimensions. They concluded that increasing elasticity enhances the pipeline resistance to deformation. The fault displacement relationships are similar but have different yield points.

Jiao et al. (2009) studied the response of pipelines under strike-slip fault using finite element shell mode (figure 2-27) and considering depth, backfill soil compactness, and nonlinear pipeline-soil interaction. They considered extended Drucker Prager model in this analysis. They considered an equivalent boundary condition which was described by Liu et al. (2004). They represented the variation of the Von Mises stress along the path of point A along the pipeline length and the Mises stress distribution at cross section of pipeline considering inner and outer diameter. They concluded that the pipeline fault crossing angle is an important parameter that determines pipeline rupture mode, and that the backfill properties (compactness) and ellipticity couldn't be ignored in design.

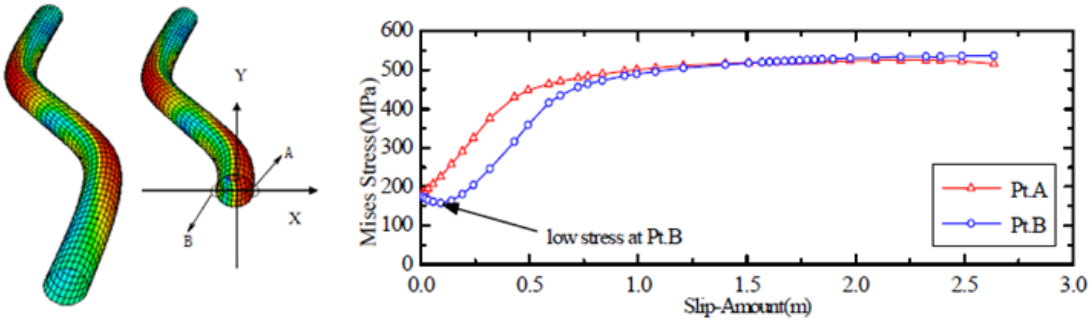

Figure 2-25 Mises stress distribution and stress change of points A and B (Jiao et al. (2009))

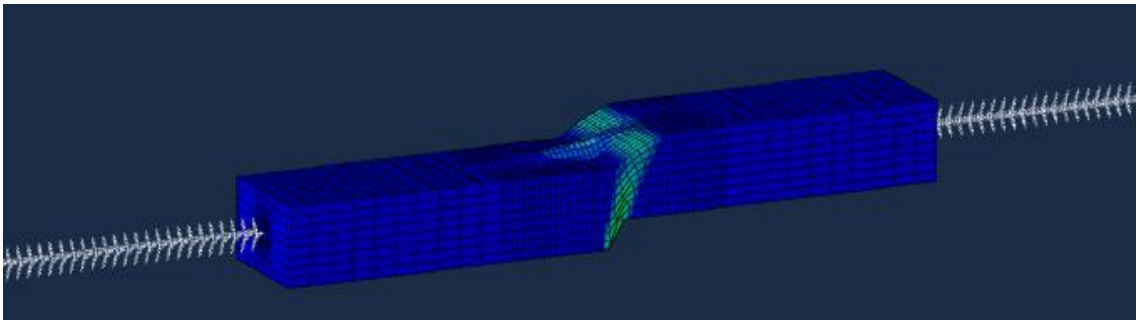

Figure 2-26 Finite element model suggested by Vasileiadis et al. (2012)

Vasileiadis et al. (2012) built a hybrid finite element model to study the behavior of buried pipeline in dense sand under normal and reverse fault using Abaqus (figure 2-28**Error! Reference source not found.**). The authors considered nonlinear geometry, nelastic behavior of pipeline and soil, and contact and friction at pipe-soil interface. Based on examining different approaches for modeling pipeline boundaries (fixed pipe ends, free pipe ends, hybrid model, spring edge model), they developed a hybrid model considering shell elements for pipe and continuum elements for soil at a length of 60D (60*diameter) and beam elements with soil springs in the regions where the pipeline undergoes expansion only. They generated graphs for critical fault displacement vs. D/t ratio under different performance criteria. They conducted a parametric study on the soil layer depth, the pipeline steel hardening properties, and the pipeline internal pressure.

CHAPTER 3

MODEL AND METHOD OF ANALYSIS

3.1 Finite Element Model

The response of offshore saturated sands under fault displacement is examined numerically using the general purpose finite element software Abaqus v.6.14. The following model simulates the behavior of the sand using effective stress analysis by considering 8 node plain strain quadrilateral, biquadratic displacement, bilinear pore elements (CPE8P) assuming drained conditions.

3.2 Model Geometry, Mesh, and Boundary Conditions

A 2D plain strain model is depicted to simulate the fault propagation mechanism in the offshore saturated sand. This model is shown in figure 3-1 representing the overlying soil of thickness H=20m susceptible to fault displacement and the corresponding finite element mesh. Bray (1994b) noted that a length of 4H is sufficient to adequately model the fault propagation. A short parametric study by the author demonstrated that a length of 140m=7H is adequate to remove the end effects of the boundary conditions. 0.5mx0.5m quadratic elements were employed in the region at the vicinity of the fault where the failure plane and maximum deformations are, and the mesh becomes coarser as we move away from the fault.

The following 2 steps have been adapted in the simulation: (1) application of the self-weight, (2) application of fault displacement. The self-weight is applied first to establish the

initial stresses in the soil. Subsequently, the external nodes of the moving part are subjected to displacement controlled loading in the direction of a pre-determined dip-slip angle at the bottom side and in the horizontal direction only at the vertical side (see figure 3-1). The fault displacement is increased gradually using a ramp function and the ground surface deformation and the corresponding plastic strains are recorded at each step. Free field conditions and rough bedrock-soil interface are assumed for the fixed part of the model. The bottom nodes of the right part are constrained in the vertical and horizontal directions whereas the vertical side nodes are constrained in the horizontal direction only.

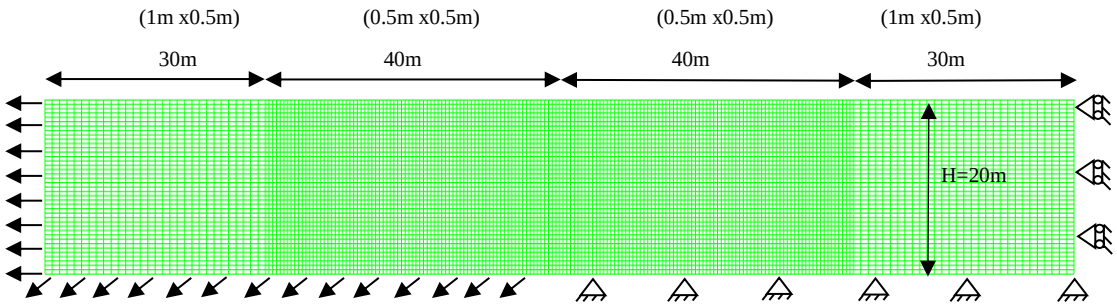

Figure 3-1 The 2D fault propagation model

The numerical analysis was performed for dip angles of 30˚, 45˚, and 60˚ for each of the normal and reverse fault cases for fault widths of 1m, 3m, and 10m with vertical bedrock displacement up to 10% of the overlying soil thickness. Additional runs were performed as well for overlying soil thicknesses of 40m and 80m subjected to reverse and normal faults.

3.3 Soil Constitutive Model

Elastoplastic material behavior that is based on a modified Mohr-Coulomb model that is capable of modeling straon softening is considered to model the sand. The soil softening

behavior has been found by previous researcher to be an essential factor in determining the fault rupture propagation and the associated deformation. For example, Cole and Lade (1984) generated formulas to predict the fault rupture surface taking into account the soil dilation angle, the fault dip angle, and the soil thickness. Lade et al. (1984) extended the work of Cole and Lade (1984) to determine the secondary fault rupture surface considering post peak soil behavior too. Scott et al. (1974) simulated numerically a vertical fault in deep alluvium using the Mohr-Coulomb elastic-perfectly plastic constitutive model but the results didn't match the experiments and reality.

Walters and Thomas (1982) simulated sandbox tests where sequential development of failure surfaces due to local uplift from a vertically rigid moving block was studied. They pointed to the importance of employing a constitutive model that incorporates strain softening and non-associated flow to model to model the location and development and propagation of localized failure surfaces in granular material. Using such a model, they succeeded in predicting the behavior in the sandbox accurately. Anastasopoulos et al. (2007) modeled the dip-slip fault propagation using Mohr-Coulomb constitutive model with strain softening in Abaqus. The numerical investigations modeled centrifuge experiments adequately. Bray et al. (1994b) conducted a numerical analysis to study thrust fault propagation through NC to slightly overconsolidated saturated clay with considering a hyperbolic constitutive model and undrained total stress analysis**.** They showed that FEM could model the experimental results qualitatively knowing that the soil's non-linear stress strain relation is modeled adequately.

Several other studies considered finite difference methods with Mohr coulomb strain softening and captured the normal and reverse fault propagation adequately (Roth et al.

(1982), White et al. (1994), Nakai et al. (1995), Loukidis (1999), Erickson et al. (2001), Loukidis (2009)). The Mohr coulomb model that incorporates strain softening has also been proven to be successful in modeling fault propagation under earth dams and delayed collapse of cut slopes in stiff clay (Potts et al. (1990, 1997)).

In the proposed study, the Mohr Coulomb model with strain softening and non-associated flow is considered. The Mohr coulomb model requires linear isotropic elasticity.

Elastic Behavior:

The elasticity incorporated in the proposed model is linear isotropic defined by Young's modulus and Poisson's ratio.

Stress Invariants:

$$\sigma_{12} = \frac{\sigma_{11} + \sigma_{22}}{2} \pm \sqrt{(\frac{\sigma_{11} - \sigma_{22}}{2})^2 + \tau_{12}^2} \quad \textit{(3-1)}$$

$$tan2\theta = \frac{2\tau_{12}}{\sigma_{11} - \sigma_{22}} \quad \textit{(3-2)}$$

$$\sigma = S - PI \quad \textit{(3-3)}$$

Pressure stress: $p = -\frac{1}{3} trace(\sigma)$ *(3-4)*

Mises stress: $q=\sqrt{\frac{3}{2}(S:S)}$ *(3-5)*

Third invariant, $r = (\frac{9}{2} S.S:S)^{\frac{1}{3}}$ *(3-6)*

Mohr Coulomb Model in Abaqus:

The Mohr coulomb model is intended for simple granular materials like soil under monotonic loading. It does not consider rate dependence since linear elastic response is followed by non-recoverable perfectly plastic response. The yield behavior depends on the hydrostatic pressure, since the material becomes stronger as the confining pressure increases and the yield behavior may be influenced by the intermediate principal stress. The model includes isotropic hardening or softening. The inelastic behavior is accompanied by volume change; the flow rule may include inelastic dilation as well as inelastic shearing. The plastic flow is smooth and nonassociated. The material properties can be temperature dependent and tension cut-off can be used to limit tensile strength.

Mohr Coulomb Description:

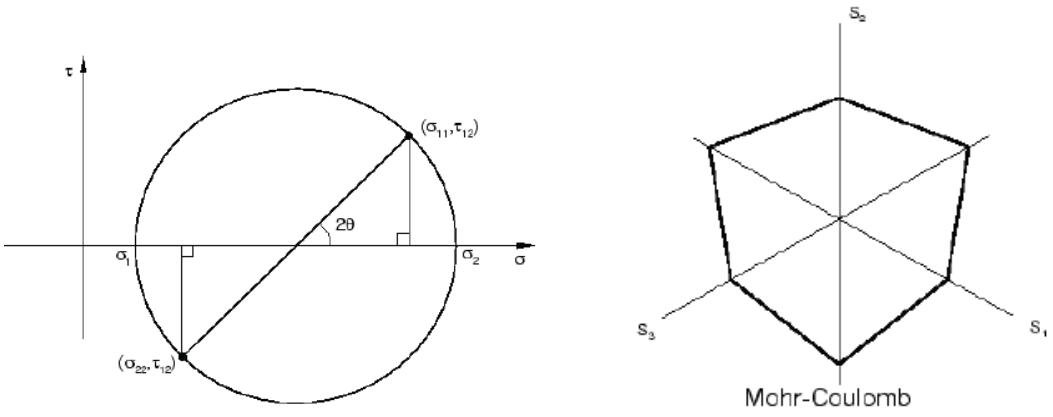

Figure 3-2 a)Mohr Coulomb circle in 2D and b) in deviatoric plane (Abaqus documentation)

The Mohr coulomb yield function is given by:

$$F = R_{mc}q - p\tan\Phi - c = 0 \qquad (3\text{-}7)$$

Where:

$R_{mc}q\ (\theta, \Phi)$ is a measure of the shape of the yield surface in the deviatoric plane (S11,S22,S33) (figure 3-2).

$$R_{mc} = \frac{1}{\sqrt{3}cos\Phi}\sin\left(\theta + \frac{\Pi}{3}\right) + \frac{1}{3}\cos\left(\theta + \frac{\Pi}{3}\right)\tan\Phi \qquad (3\text{-}8)$$

Where Φ is the slope of the Mohr-Coulomb yield surface in the $R_{mc}q - p$ stress plane, which is commonly referred to as the friction angle of the material, $0 < \Phi < 90^{\circ}$.

C is the cohesion of the material

Θ is the deviatoric polar angle defined by:

$$\cos(3\theta) = \frac{r^3}{q^3} \qquad (3\text{-}9)$$

The Mohr coulomb model defines hardening in terms of cohesion with the hardening being isotropic.

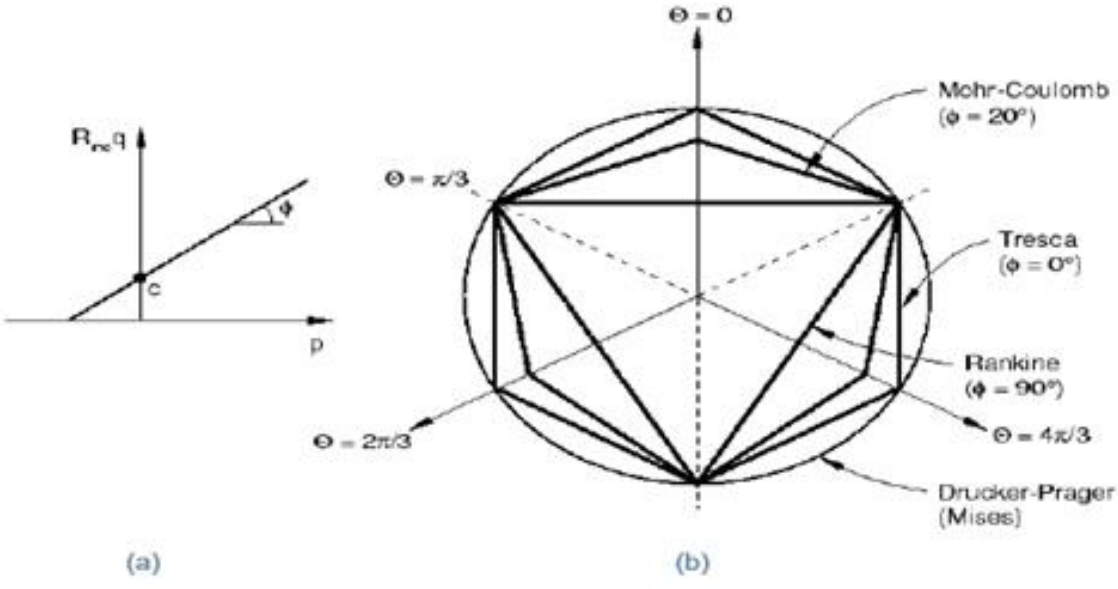

Figure 3-3 Yield surface in meridional plane (a) and deviatoric plane (b) (Abaqus documentation)

Plastic Flow:

The flow potential G is chosen as a hyperbolic function in the meridional plane (figure 3-4) and the smooth elliptic function proposed by Menetry and William (1995) in the deviatoric stress plane:

$$G = \sqrt{(\epsilon\, c|_0\, tan\psi)^2 + (R_{mw} q)^2} - p tan\psi \qquad (3\text{-}10)$$

Where $c|_0$ is the initial cohesion of the material ($\bar{\epsilon}^{pl} = 0$), Ψ: the dilation angle of the material , ϵ: the meridional eccentricity controls the shape of G in the meridional plane (p-q plane).

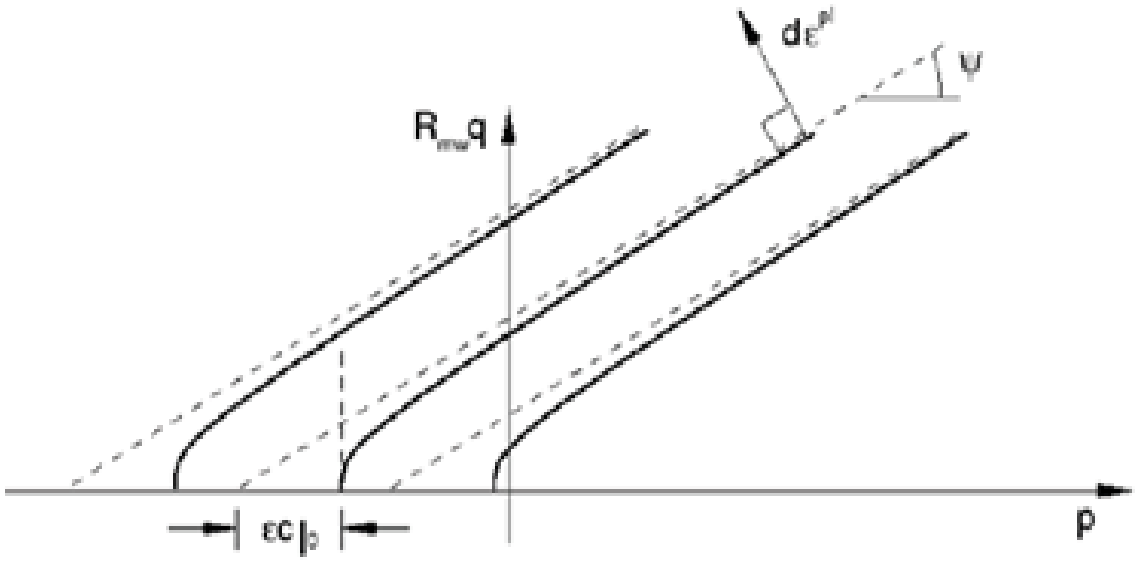

Figure 3-4 Mohr Coulomb in Meridional plane (Abaqus documentation)

$R_{mw}(\theta, e, \Phi)$ controls the shape of G in the deviatoric plane

$$R_{mw} = \frac{4(1-e^2)(cos\theta)^2 + (2e-1)^2}{2(1-e^2)cos\theta + (2e-1)\sqrt{4(1-e^2)(cos\theta)^2 + 5e^2 - 4e}} R_{mc}(\frac{\Pi}{3}, \Phi) \qquad (3\text{-}11)$$

The deviatoric eccentricity describes the "out-of-roundedness" of the deviatoric section in terms of the ratio between the shear stress along the extension meridian (θ=0) and the shear stress along the compression meridian (θ=Π/3).

The default value of the deviatoric eccentricity is

$$e = \frac{3 - sin\Phi}{3 + sin\Phi} \qquad (3\text{-}12)$$

e allows the Abaqus Mohr-Coulomb model to match the behavior of the classic Mohr-coulomb model in triaxial tension and compression. The plasticity flow in the Mohr coulomb model is always non-associated. An unsymmetric solver is always required in the Mohr coulomb model.

The Abaqus Mohr coulomb model uses smooth plastic flow potential and doesn't provide the same plastic behavior like the classical (associated) Mohr Coulomb which has faceted flow potential. With the value of deviatoric eccentricity, Abaqus matches the classical Mohr coulomb model (associated) with triaxial compression or extension.

Strain Softening:

The elastic-plastic Mohr coulomb constitutive material behavior with strain softening is chosen to model the soil behavior. Based on the literature of fault propagation (Anastasopoulos (2007), Loukidis (2009)), the use of the depicted constitutive model has proven that it is capable of capturing the fault rupture propagation behavior adequately. Strain softening behavior is incorporated by a subroutine file encoded to the finite element software Abaqus v. 6.13.

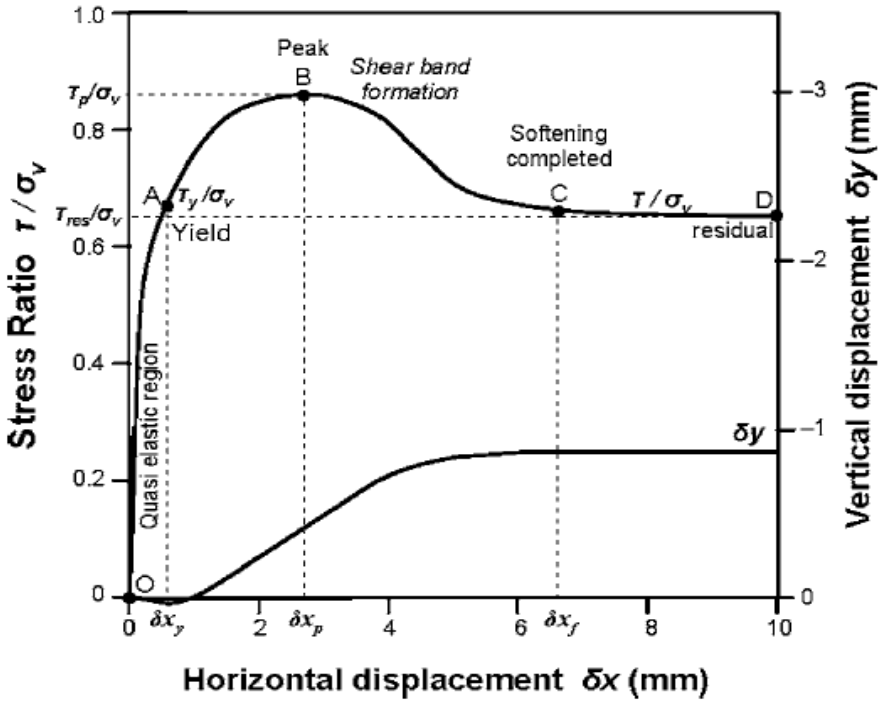

Figure 3-5 Typical variation of stress ratio and volume change with repsect to horizontal displacment in direct shear test for dense Toyoura sand (Shibuya et al. 1997)

The strain softening is introduced by the linear reduction of the mobilized friction angle ($\Phi_{mob.}$) and the mobilized dilation angle (ψ_{mob}), as a function of deviatoric plastic shear strain (γ_{dev}^{p}) until critical state conditions are reached at a certain value of deviatoric plastic shear strain (γ_{f}^{p}) (Anastasopoulos et al. (2007)) (figure 3-6)

$$\Phi_{mob} = \begin{cases} \Phi_p - \dfrac{\Phi_p - \Phi_{res}}{\gamma_f^P}\gamma_{dev}^P & for \quad 0 \le \gamma_{dev}^P < \gamma_f^P \quad (3\text{-}13) \\ \Phi_{res} & for \quad \gamma_{dev}^P \ge \gamma_f^P \quad (3\text{-}14) \end{cases}$$

$$\psi_{mob} = \begin{cases} \psi_p(1 - \dfrac{\gamma_{dev}^P}{\gamma_f^P}) & for \quad 0 \le \gamma_{dev}^P < \gamma_f^P \quad (3\text{-}15) \\ \psi_{res} & for \quad \gamma_{dev}^P \ge \gamma_f^P \quad (3\text{-}16) \end{cases}$$

Where:

Φ_P : ultimate mobilized friction angle

Φ_{res}: residual (for critical state) friction angle

ψ_P: ultimate dilation angle

γ_f^P: plastic octahedral shear strain at which softening is completed

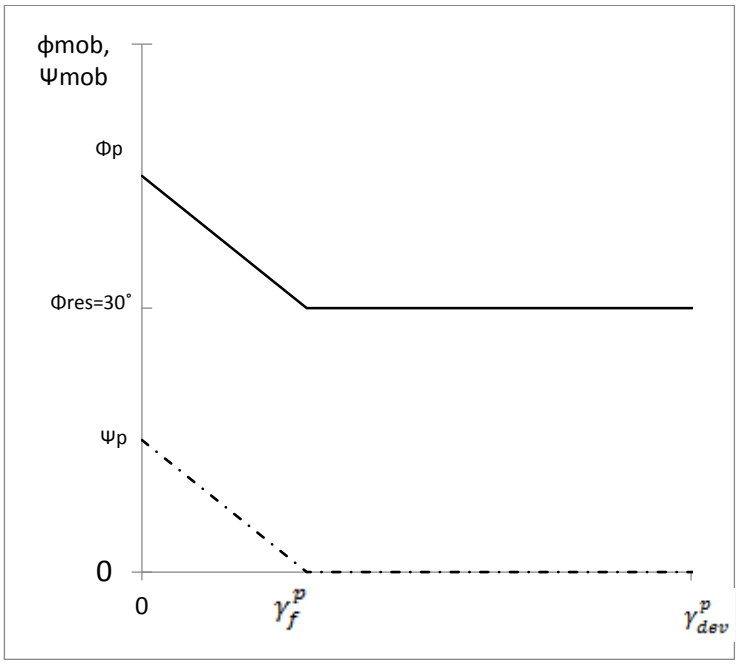

Figure 3-6 Reduction of peak friction angle and peak dilation angle with plastic deviatoric strain

3.4 Soil Properties:

Sands at three relative densities are considered in the numerical analysis. The relative densities reflect dense (D), medium dense (MD), and loose (L) saturated sand. The constitutive model parameters for the following soil types are characterized by the soil cohesion c, Young's modulus E, Poisson's ratio (υ), peak friction angle Φ_{peak}, peak dilation angle ψ_{peak}, residual friction angle Φ_{res}, and the residual deviatoric plastic shear strain

(γ_f^p) and are presented in the Table 1 and Figure 3-7. The sand characteristics were estimated based on EPRI design manual.

Table 1 Saturated Sand Properties

	D	MD	L
γ' (KN/m3)	11.6	11	10.5
E (KPa)	$11209\sqrt{z}$	$7300\sqrt{z}$	$5063\sqrt{z}$
C	0	0	0
Φ_{res} (˚)	30	30	30
(γ_f^p)	0.1	0.1	-

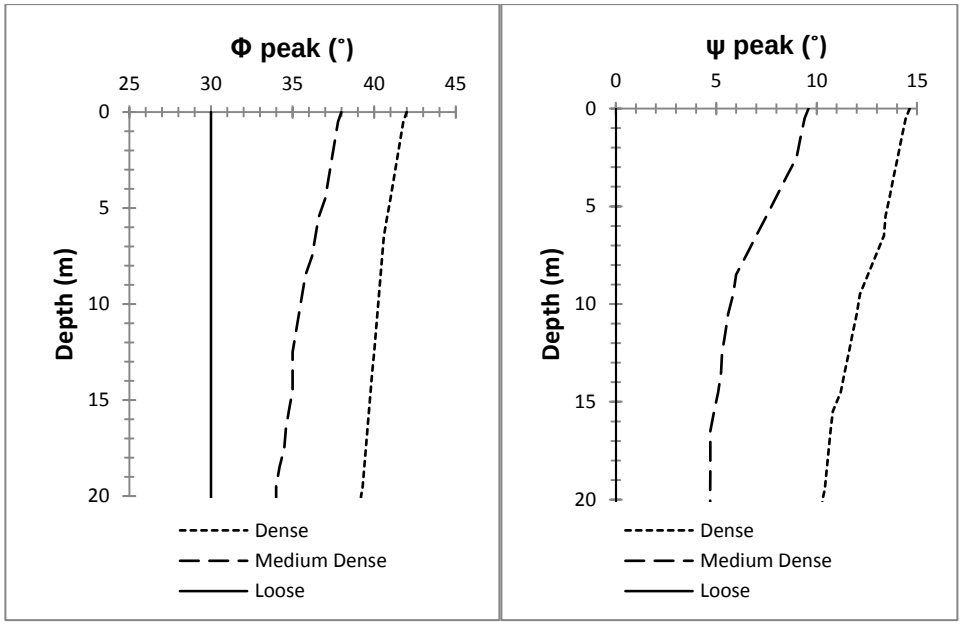

Figure 3-7 Peak Friction Angle and b) dilation angle variation with depth

The values represented in the graphs are assigned to input parameters of the constitutive model. The young's modulus (E), peak friction angle (Φ_{peak}), peak dilation angle (Φ_{peak}), and Poisson's ratio (υ) are assumed to vary with depth as the confining

pressure increases. The young's modulus of the sand is assumed to be a linear function of the square root of the confining pressure $\sqrt{\sigma_{vo}'}$ and therefore a linear function of $\sqrt{z}$ (Loukidis et al. (2009)).

Dense sand has a modulus of elasticity of E=11209$\sqrt{z}$ Kpa (Table 1). The dense sand considered is characterized by a peak friction angle (Φ_{peak}) of 42˚, a dilation angle (Φ_{peak}) of 15˚, a Poisson's ratio (υ) of 0.36 that decrease with decreasing depth as shown in the above graphs to values of 39˚, 11˚, and 0.31 respectively (figure 3-7) at 20m.

Medium Dense sand has a modulus of elasticity having the following equation E=7300$\sqrt{z}$ kPa (Table 1). The peak friction angle (Φ_{peak}), the peak dilation angle (ψ_{peak}), and the Poisson's ratio (υ) are 38˚, 10˚, and 0.3 at the ground surface and are reduced with depth to values of 34˚, 5˚, and 0.24 respectively at 20m (figure 3-7).

The loose sand has a friction angle and dilation angle equal to the residual values of $\Phi_{peak} = \Phi_{res} = 30^{\circ}$ and 0˚. The modulus of elasticity has a general form of 5063$\sqrt{z}$ kPa and a Poisson's ratio of 0.18 (Table 1).

The friction and dilation angle of dense and medium dense sand are reduced with increasing deviatoric plastic strain to a residual values of Φ_{res}=30˚ and $\psi_{res} = 0^{\circ}$ at critical state reached at $\gamma_f^p = 0.1$). The model for loose sand doesn't incorporate any softening behavior and the friction and dilation angle of loose sand are equal to the residual values.

CHAPTER 4

NUMERICAL RESULTS AND DISCUSSION

4.1 Introduction:

FE analyses were performed for dense, medium dense, and loose sand under reverse and normal faults having dip angles of 30˚, 45˚, and 60˚ and using different fault widths of 1m, 3m, and 10m. The height of the overlying soil was varied as well from the base case of H = 20m to values of H=40m and 80m and the influence of each parameter was examined. Fault displacements up to 10% of the soil layer thickness were enforced. Figure 4-1 depicts a schematic representation of the model and the parameters investigated in the thesis.

In Section **Error! Reference source not found.**, a soil model of height 20m, length 40m, and a fault width of 1m is analyzed for different sand relative densities (Dense, Medium Dense, and Loose sand) and dip angles for both normal and reverse fault cases. In Section 0, the fault breccia zone thickness is varied to values of 1m, 3m, and 10m and the corresponding response is compared for both normal and reverse fault cases. Finally in Section 0, models of varying overlying soil layer thickness (20m, 40m, 80m) are investigated.

4.2 Effect of Relative Density

4.2.1 Ground Surface Deformation Profile

Ground Surface Deformation Profile in figures 4-2 to 4-4 depict the variation of the vertical normalized ground surface deformation (y/H) and plastic strains for dense, medium

dense, and loose sand under normal and reverse faults of different dip angles (30˚, 45˚, 60˚) subjected to vertical bedrock displacements ranging from 2% to 10% of the soil layer thickness (H). The graphs are centered with respect to the midpoint O of the fault displacement zone and are normalized with respect to the overlying soil layer thickness (H). The curves plotted in figures 4-2 to 4-4 provide essential input for mitigating the fault rupture geohazard which requires accounting for fault-induced ground surface deformation (Kelson at al. (2001)).

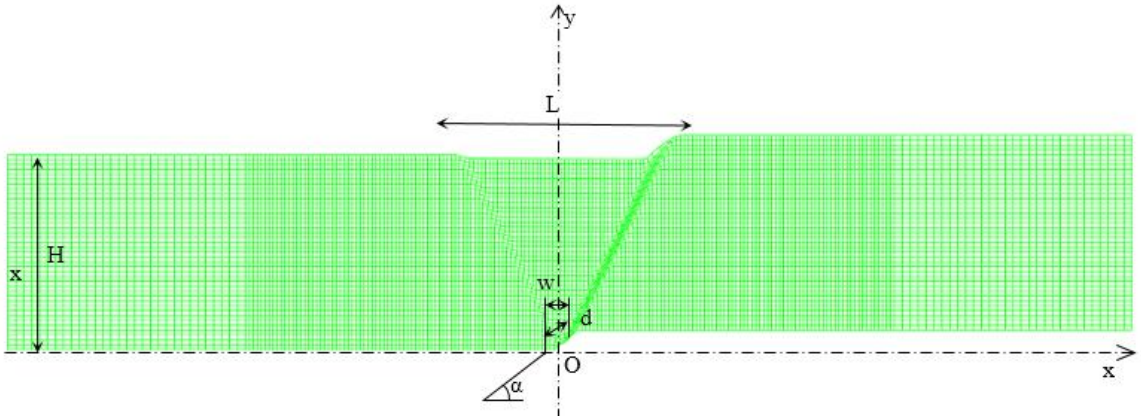

L: Length of distorted zone / the distorted zone is located by two points' horizontal distance from the center of the fault (O). The first point is located by the first point starting from the left side towards the x'x direction where the ground surface inclination is greater than 0.02% and the second point is determined by the same way but starting from the left side and in the backward direction.
C: center of the distortion zone determined by the midpoint of the two located points indicated above.
W: width within which fault displacement occurs
d: inclined distance of the bedrock displacement
α: dip angle represented by the angle with the horizontal in the $\overrightarrow{x'x}$ direction

Figure 4-1 Schematic presentation of the fault rupture procedure and the parameters studied in the following thesis

Normal Fault Case:

For the case of a normal fault with a soil thickness of 20m and a fault width of 1.0m, the curves on figure4-2 indicate ground surface deformations that are dependent on the dip angle of the normal fault and the density of the sand. It is observed that the steepness of the ground surface deformation profile in the shearing zone is greater for the

case of dense sand than medium dense sand and loose sand respectively. Similar results have been reported in Loukidis et al. (2009). The higher inclination angles for dense sands could be attributed to the higher soil stiffness. For dense sands, shearing occurs over a narrower zone and propagates to the surface at lower bedrock displacement values.

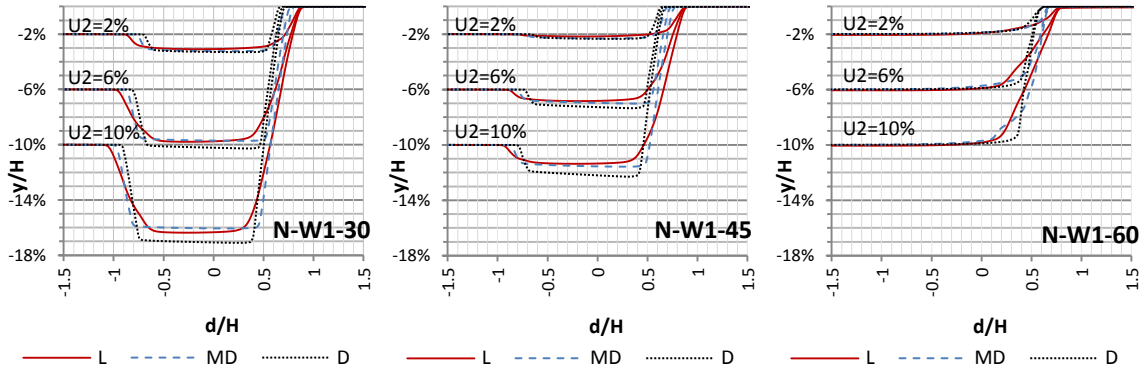

N: Normal fault; R: Reverse fault
D: Dense Sand; MD:Medium Dense Sand; L: Loose Sand
W: W1: width 1m; W3: width 3m; W10: width 10m

Figure 4-2 Ground surface deformation profiles for normal fault case.

A general analysis of the distribution and concentration of plastic shear strains in figure 4-3 indicates that the plastic strains for normal faults are distributed around a wider zone for the case of loose sand than dense sand. This agrees with results from previous research by Loukidis et al. (2009) and Lin et al. (2006). Shearing zones are wider for loose sand than medium dense and dense sand respectively (Loukidis et al.(2009) and Anastasopoulos et al. (2007)). The shear bands shift from linear to spiral as the relative density of the sand decreases and their shapes and locations agree with previous case studies (Bray et al. (1994a)), and experiments (Cole et al. (1984), Lade at al. (1984), Loukidis et al.(2009), Anastasopoulos et al. (2007), Bransby et al. (2008a)).

A more detailed analysis of the ground surface deformation profiles and plastic strains for the case of a **normal fault** leads to the following conclusions:

1. The shallower the dip angle, the more likely is the formation of a graben. A graben is formed when a secondary failure plane forms in the opposite direction of the major failure plane. The formation of a graben in the case of normal faults was observed in previous case histories and experimental studies (Kelson et al. (2001)), Bray et al. (1994a), Cole et al. (1984), Lade et al. (1984), Anasatasopoulos et al. (2007)), and numerical investigations (Anasatasopoulos et al. (2007), Loukidis et al. (2009), and Bransby et al. (2008a)). For the case of the shallower dip angle of 30˚, the graben forms at small bedrock displacements in the order of about 0.5%H. As the dip angle becomes steeper (ex. 45˚), a higher bedrock displacement (greater than 2.0%H) is required before the graben forms. For steeper dip angles (60˚) only a primary failure plane forms.
2. The width of the graben is observed to be larger for the case of loose sand (~2H for dip angle of 30˚ and ~1.8H for a dip angle of 45˚) than for medium dense sand (~1.7H for dip angles of 30˚and 45˚) and dense sand respectively (~1.6H for dip angle of 30˚and ~1.5H for dip angle of 45˚). As shearing occurs over wider zones in loose sand, the corresponding distorted zones are wider as well.
3. The location of the surface fault outcrop when measured from the center of the fault is observed to be farther from the center for loose sand (distance of ~ 0.9H for dip angles of 30˚ and 45˚, and 0.8H for dip angle of 60˚) than medium dense (~0.8H for

dip angle of 30˚, 0.75H for dip angle of 45˚, and 0.7H for dip angle of 60˚) and dense sand (0.7H for dip angles of 30˚ and 45˚, and 0.6H for dip angle of 60˚).

4. The height of the scarp is larger for shallow dip angles 30˚ (at U2=10%H, 0.7%H for dense, 0.6%H for medium dense and loose sand) than steep dip angles 45˚ (at U2=10%H, 2%H for dense and medium dense, and 1.5%H for loose sand). At shallower dip angles considering a certain vertical bedrock displacement the inclined bedrock displacement distance is larger than for steeper dip angles.

Reverse Fault Case:

For the base case (H = 20m, and w = 1m) of a **reverse fault** (figures 4-4 and 4-5)), an analysis of the surface ground deformations and the distribution and concentration of plastic shear strains indicates that:

1) At shallow dip angles, high relative densities, and large bedrock displacements, a back-thrust forms leading to a "pop-up structure" that is characterized by a central uplifted zone that exhibits upward displacements exceeding the applied bedrock displacement. The deformation mechanism is characterized by an initial formation of a primary failure plane at relatively low bedrock deformations followed by a secondary failure plane that forms in the opposite direction and propagates to the surface. A back-thrust was formed in Taiwan city Chelungpu thrust Fault during the 1999 Chi-chi earthquake (Kelson (2001)).
2) Unlike the case of a normal fault, the scarp height of the pop-up structure is smaller for the case of loose sand (1.3%H for dip angle of 30 º at fault displacement of

10%H), than medium dense sand and dense sand (2%H for dip angle of 30º). This is explained by the fact that in loose sand the shear band requires a higher bedrock displacement to migrate to the surface inducing a smaller pop-up height than medium dense and dense sand.

3) The width of the pop-up zone is larger for the case of dense sand (3.1H for dip angle of 30 º at fault displacement of 10%H) than medium dense sand (2.7H for dip angle of 30 º) and loose sand (2.4H for dip angle of 30 º) since the locations of the shear bands are farther for dense sand.

4) For the cases involving dense sands, a single primary shear band is formed at small bedrock displacements, irrespective of the dip angle of the fault. This single shear band propagates to the surface as the bedrock displacement increases. For cases involving medium dense sands, the fault propagation mechanism is observed to be sensitive to the dip angle of the fault and is a function of the magnitude of the fault displacement, particularly for the cases involving the steeper dip angles of 45˚ and 60˚ where multiple secondary shear bands form on the side of the fixed wall resulting in a more-or-less 2 step ground displacement profile. In these cases, the first primary shear band (the one to the left) reaches the surface at relatively small displacements. At higher fault movements (around 3%H), secondary shear bands form to the right of the primary shear band. For the case of loose sand, multiple shear bands are observed for all dip angles resulting in a relatively wide shear zone that originates from the bedrock and reaches the surface over a relatively continuous and wide area.

5) The formation of multiple shear bands in medium dense sand and loose sand as the bedrock displacement increases is the direct result of the mobilization of excessive shear strains in the soil. In dense sand, even at vertical bedrock displacements as high as 10%H, the resulting shear strains were not sufficient to cause failure and shearing in a secondary direction. For medium dense sand, the formation of secondary failure planes is illustrated in the form of a 2 step displacement on the ground surface deformation profile. The secondary shear band is at a farther location from the center than the primary shear band, rendering the location of the fault outcrop farther from the center. In the case of loose sand, a continuous band of shear planes form and propagate to the surface resulting in a more continuous surface deformation profile in comparison to the two-step profile witnessed in medium dense sand. However, the formation of multiple continuous shear surfaces in loose sands seems to have formed closer to the primary shear band rendering the right boundary of the shear band closer to the center compared to the medium dense case with the 2-step deformation mechanism.

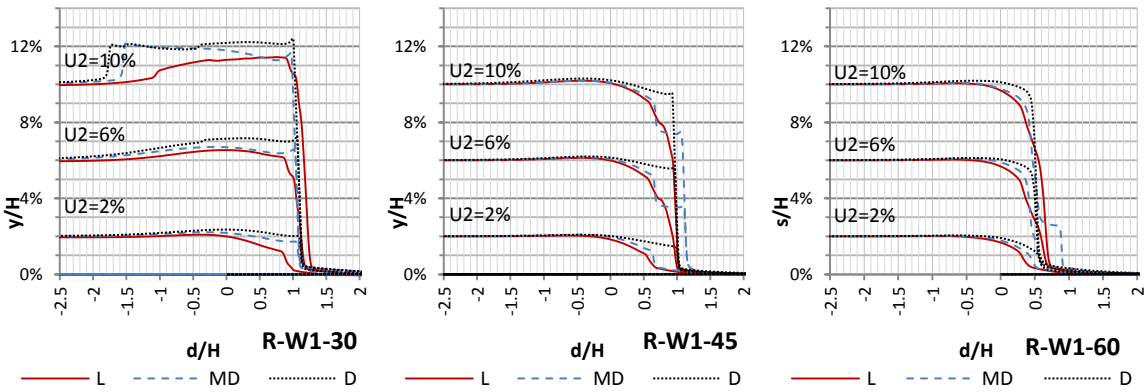

Figure 4-4 Ground surface deformation profiles for reverse fault case.

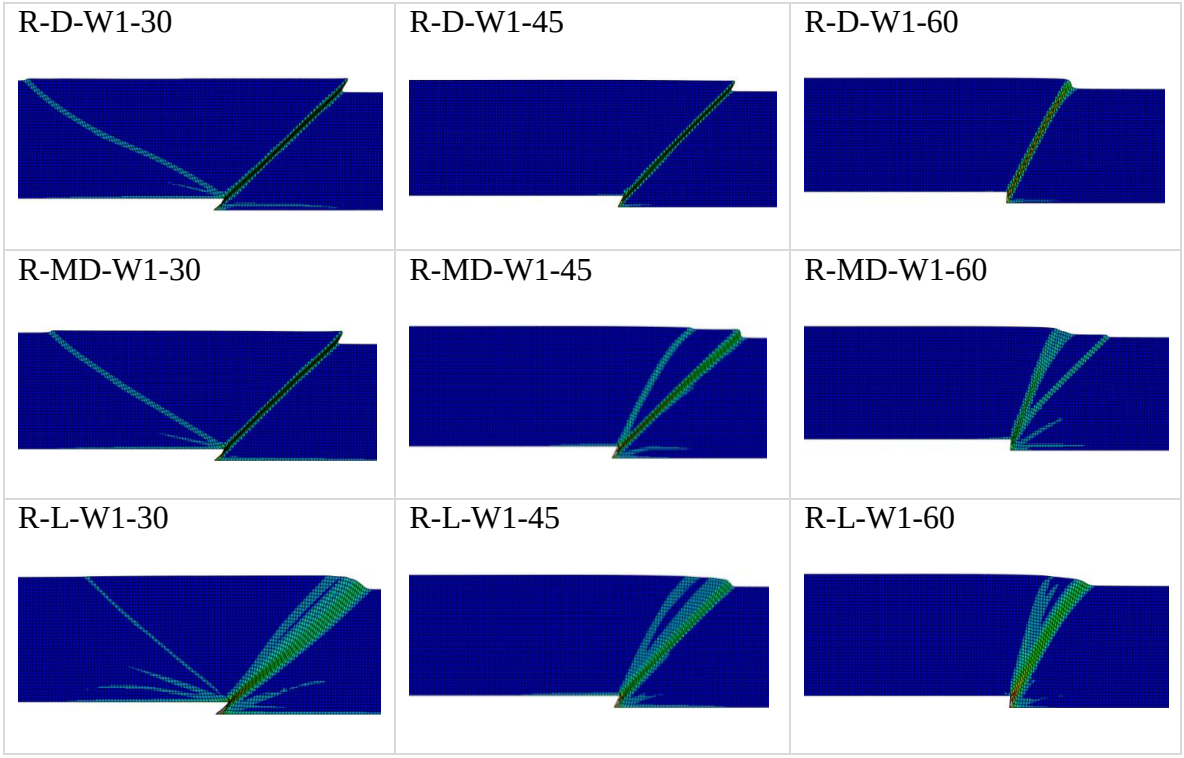

Figure 4-5 Plastic shear strains for reverse fault above cases

4.2.2 Extent and Location of the Shear Surface/Band

To facilitate the analysis of the FE results presented in figures 4-2 to 4-5 , the distance from the center of the fault zone to the primary shear surface/band was defined as "S" and calculated for all the cases analyzed. The distance "S" was then normalized by the soil thickness "H" and plotted on figure 4-6 for both normal and reverse faulting conditions. The results on 4-6a correspond to the normalized locations of the primary shear surfaces/bands at a vertical bedrock displacement of 2.75%H, while the results on figure 4-6b correspond to a normalized displacement of 10%H. These values of fault displacement were chosen to represent intermediate and large displacements, respectively and to allow for comparison with other published data from previous experimental and numerical

investigations. In figure 4-6b, data represented by dotted symbols were added to the figure to reflect the normalized location of the right-most secondary failure surface/band, if present

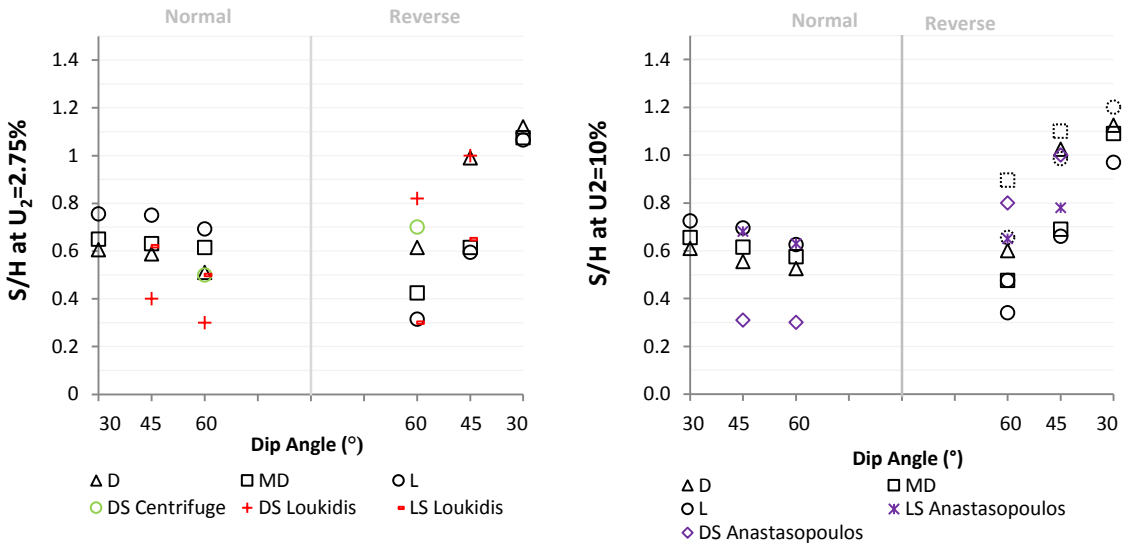

L: Loose, M: medium dense, D: dense

Figure 4-6 Location of shear bands at a)U2=2.75%H &b) 10%H

By comparing the the results in Figure 4-6 a) and b) it is concluded that as the bedrock displacement increases, the locations of the initial primary shear bands do not vary. At large bedrock displacements, additional secondary shear bands form in the reverse fault case, resulting in a 2-step displacement or a continuous displacement at the surface. The location of the right boundaries of these secondary shear bands are farther from the center in the case of a reverse fault.

When comparing the cases of normal faults with different sand densities, it is observed that the locations of the primary shear bands are farther for loose sand than medium dense sand and dense sand, respectively. The normalized locations vary from 0.6H

to 0.8H for the case of a shallow fault angle of 30^{o} with the range decreasing to 0.5H to 0.7H for the steepest dip angle of 60^{o}.

On the other hand, the normalized locations of the primary shear bands for the case of reverse faults seem to be more sensitive to the sand density and the dip angle of the reverse fault. In fact, the normalized locations of the shear bands from the center of the fault tend to be the highest for dense sands, with differences between the loose and dense cases being the highest for the steeper dip angles of 45 and 60 degrees. For example, S/H is observed to vary from 0.3H to 0.6H (for dip angle of 60 degrees) and from the 0.6H to 1.0H (for dip angle of 45 degrees) as the soil density is increased from loose to dense. For the shallowest dip angle of 30 degrees, the effect of relative density is minimal with S/H values in the order of 1.1H, irrespective of relative density.

The locations of the secondary shear bands that were observed in the reverse fault cases involving loose and medium dense sands are reflected in figure 4-6 b) using dotted markers. The secondary shear bands form at high bedrock displacements and appear in the form of a 2 step displacement or a continuous displacement. The locations of the secondary shear bands are farther from the center for the case of medium dense sand than loose sand.

It is worth noting that the normalized shear band locations that were determined in this study for sands of different relative densities compare well with results from previous numerical and experimental investigations as reported in Loukidis et al. (2009) and Anastasopoulos et al (2007) at a vertical bedrock displacement of 2.75% of the overlying soil layer thickness H as shown in figure 4-6. Multiple shear bands appeared as well for dip angle 60 with Loukidis et al. (2009) for loose sand and Bray et al. (1989) for clay box

experiment. In our model the strain softening is defined by decreasing the friction angle and dilation angle as a function of the deviatoric strain. A residual dilation angle of 0.1 degrees instead of 0 degrees was input into the Abaqus model to avoid numerical errors and convergence problems.

The locations of the shear bands coincide with the locations of shear bands obtained by the FE models by Anastasopoulos et al. (2007) and Loukidis et al. (2007) in case softening was applied as a function of varying plastic strain in the global direction xy (denoted by PE12 in Abaqus) approximately along the direction of the shear plane and by applying a residual dilation angle of 2 dgrees instead of 0.1 degrees.

4.2.3 Bedrock Displacement Required for Rupture to reach the Surface

Ground deformations in soils overlying a fault are not considered dangerous unless the rupture propagates to the ground surface. Let d_{cr} denote the inclined fault bedrock displacement required for the rupture to propagate to the surface (figure 4-1). Values of d_{cr} were calculated for all the cases analyzed and the normalized critical distance d_{cr} /H was plotted on figure 4-7 for dense, medium dense, and loose sand cases under different fault dip angles α considering an overlying soil thickness of 20m and a fault width of 1m. The critical bedrock displacement is determined by the inclined distance of the bedrock displacement for the shear band yield points to reach the top surface.

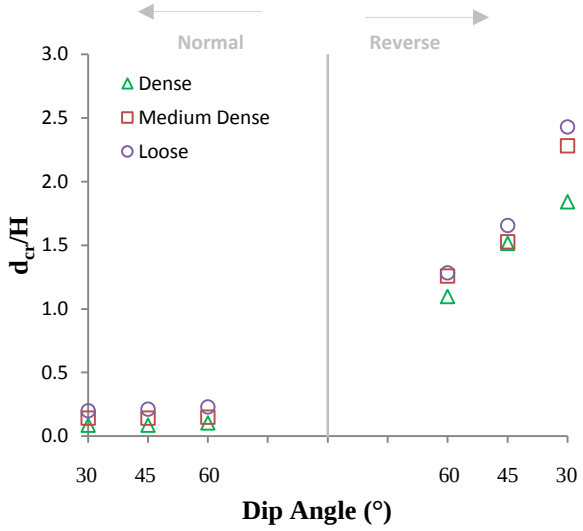

Figure 4-7 Critical bedrock displacement for the rupture to reach the surface

Results on figure 4.7 indicate that d_{cr}/H is larger for reverse fault than the normal fault cases. These findings are in line with results by Bray et al. (1994b) and Loukidis et al. (2009) who state that the deformation mechanism in normal fault cases is analogous to that governing the mobilization of active earth pressures while the deformation mechanism in reverse fault cases is analougous to the passive earth pressure case.

For the case of normal fault, results indicate that the required bedrock displacement for the rupture to reach the surface is small, insensitive to the relative density and fault dip angle, and falls in the narrow range of 0.1%H for dense sands to 0.2%H for loose sand (Figure 4-7). For the case of reverse fault, the normalized critical displacements are larger and are sentive to the density and the dip angle. For loose sand, d_{cr}/H is 1.3% at a dip angle of 60˚, 1.7% at 45˚, and 2.45% at 30˚. These numbers decrease for medium dense sand (1.25% at 60˚, 1.5% at 45˚, and 2.3% at 30˚), and dense sand (1.1% at 60˚, 1.5% at 45˚, and 1.85% at 30˚). The higher bedrock displacements that are required for the shear bands to reach the

surface in loose sands could be attributed to the fault propagatiom mechanism that is characterized by the formation of wider multiple shear bands and to compressive volume changes that would accompany the shearing mechanism necessitating larger fault movements at the source to push the failure mechanism to the surface.

The higher required bedrock displacements that were observed for the shallower dip angles in the reverse fault case could be related to the relatively larger distance that the shear band has to traverse to reach the ground surface. It could also be related to the presence of relatively higher passive pressures resulting from the larger volume of soil overlying the shear band.

4.2.4 Length and Center of Distorted Zone

The length of the distorted zone is essential to determine the lateral extent of the zone that would be affected by the fault displacement and to define setback limits that would ensure minimal interference with the fault propagation mechanism. The length of the distorted zone was defined by Loukidis et al. (2009) as the length of the zone within which the ground surface inclination (slope) exceeds 0.2%. In this zone, it could be argued that the soil would have suffered from distortion, softening, strength loss, etc., resulting in reductions in bearing capacity and stiffness (Loukidis et al. (2007)).

The length of the distorted zone (L) was calculated and used to define the horizontal distance from the fault origin to the midpoint of the distorted zone (C). Both L and C were normalized by the height of soil H and the normalized length (L/H) and location of the center of the distorted zone (C/H) were plotted as a function of the fault type and dip angle

on Figs. 43a and 43b, respectively for the cases of dense, medium dense and loose sands. All values are calculated for the case with a maximum fault movement of 10%H.

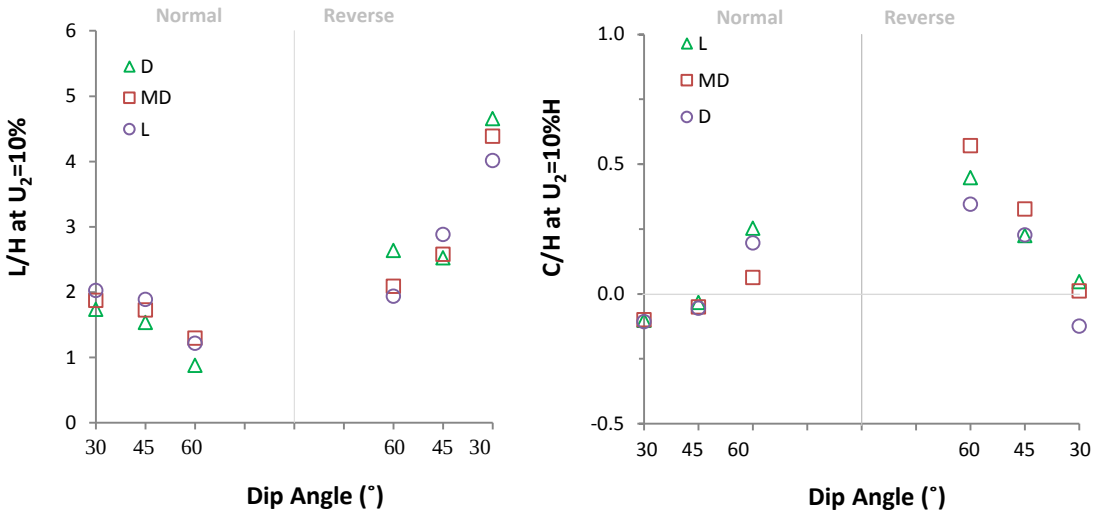

Figure 4-8 Normalized Length (L/H) and b) center (C/H) of distorted zone for saturated sand subjected to normal fault (30°, 45°, 60°) for dense, medium dense, and loose sand

Results on figure 4-8 indicate that the normalized length of the distorted zone for both normal and reverse faults is more affected by the dip angle of the fault than it is affected by the density of the soil. The length of the distorted zone is larger for cases with shallower dip angles which are generally associated with wider shear bands. For a normal fault with a dip angle of 30˚, L/H ranges from about 1.7 to about 2.0 for the dense and loose cases, respectively. These numbers decrease as the dip angle of the normal fault increases, reaching values as low as 0.9 to 1.3 for dense and loose sand cases with a high fault dip angle of 60˚.

For the case of reverse faults, the length of the distorted zone is much larger with an L/H range of 4 to 4.65 for the case with a dip angle of 30˚, 2.6 to 2.96 for the case with a

dip angle of 45˚, and 1.9 to 2.6 for the case with a dip angle of 30˚. The L/H values are generally larger for dense sands compared to loose sands.

It should be noted that the larger values of L/H that are associated with the shallower dip angles for both normal and reverse faults are directly related to the formation of graben structures (for the case of a normal fault) and pop-up structures (for the case of reverse faults). The formation of these structures at larger bedrock displacements magnify the length of the distorted zone by a factor of about 2.0 compared to the cases where these structures do not form. The largest range of L/H occurs in reverse faults with a shallow dip angle of 30 degrees where a relatively shallow back-thrust forms resulting in a significant widening of the distorted zone.

The location of the center of the distorted zone is directly related to the length of the distorted zone and the formation of graben and pop-up structures. For cases with no graben formation or back-thrust formation (generally faults with the steeper dip angles), the center of the distorted zone is generally located to the right of the fault center (see figure 4-8). In such cases, results on figure 4-8b indicate that the location of the center of the distorted zone is farther from the center of the fault for reverse fault cases (C/H ranges from 0.35 to 0.57) compared to the normal fault counterparts (C/H ranges from 0.06 to 0.25). This is clearly exhibited for the steep dip angle of 60^{o}.

At shallower dip angles, the location of the center of the distorted zone tends to the center O of the fault since secondary shear bands that are of opposite direction to the primary shear band propagate to the surface. In these cases graben or pop-up structures

generally form. These results generally agree with previous research (Loukidis et al. (2009)).

The analysis presented in the previous section with regards to the length and center of the distorted zone pertain to a very large fault movements that are in the order of 10% of the overlying height of soil. The conclusions resulting from these analyses could differ with the magnitude of the applied fault displacement, given the sensitivity of the fault prepagation mechanism (single versus multiple shear bands, formation of grabens and back-thrusts, among others) to the magnitude of the fault displacement. For this purpose, the length of the distorted zone and the location of the distorted zone were calculated at different levels of bedrock fault displacement. The variation of L/H and C/H with the fault displacement is presented in figure 4-9 and 4-10 for the normal and reverse fault cases, respectively.

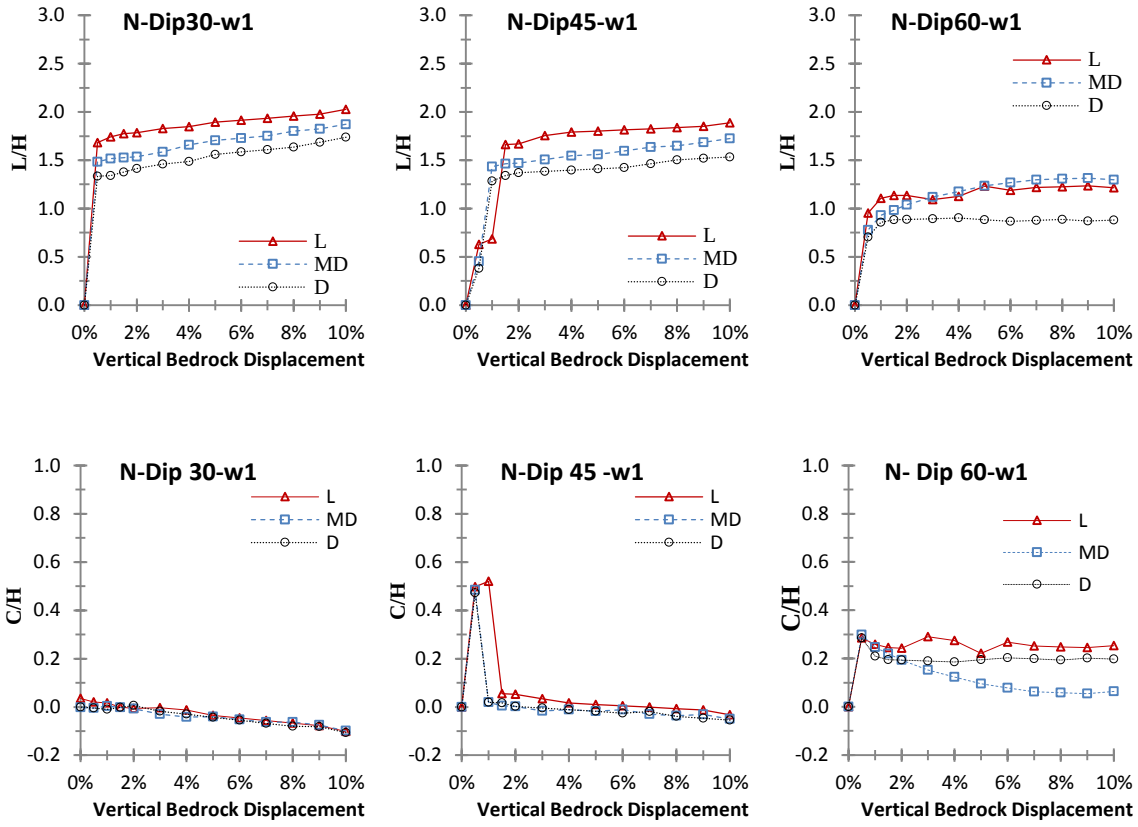

Figure 4-9 Normalized Length (L/H) and center (C/H) of distorted zone for saturated sand subjected to normal fault for dense, medium dense, and loose sand vs. vertical bedrock displacement

The results on figure 4-9 for the ***normal fault*** case lead to the following main observations in relation to the role that the imposed vertical bedrock displacement play in regards to the fault propagation mechanism:

1. For the case with a dip angle of 30˚, the fault propagation initiates with a more-or-less immediate formation of primary and secondary shear bands, resulting in a graben structure even at fault displacements that are less than 0.5%H. At a fault displacement of 1.0%H, the normalized length of the distorted zone ranges from 1.33 to 1.68 depending on the relative density of

the sand, and the center of the distorted zone conincides with the center of the fault as indicated by the C/H of zero. As the fault displacement increases beyond 1%, the length of the distorted zone increases linearly with the fault displacement but at a realtively small rate while the center of the distorted zone drifts slightly and consistently to the left of the center of the fault.

2. For the case with a dip angle of 45˚, the primary shear band reaches the surface at a relatively small displacement of 0.1%H and the length of the distorted zone increases with further displacements. After a threshold fault displacement that is a function of relative density is reached (1%H for medium dense and dense sands and 1.5%H for loose sands), a secondary shear band forms resulting in a graben. Once the graben forms, the length of the distorted zone increases abruptly (L/H increases from 0.38 to 1.28 for dense sand and from 0.68 to 1.66 for loose sand). In addition, the normalized location of the center of the distorted zone C/H decreases abruptly from 0.5 to around zero. Once the graben forms, the relationship between L/H and C/H with additional fault displacement becomes relatively stable and similar to that of the 30º fault.
3. Finally, for the normal fault cases with the steepest dip angle of 60, since no secondary shear band or graben is formed, the center is located to the side of the fixed wall and the length of the distorted zone is smaller compared to shallower dip angles.

Reverse Fault Case:

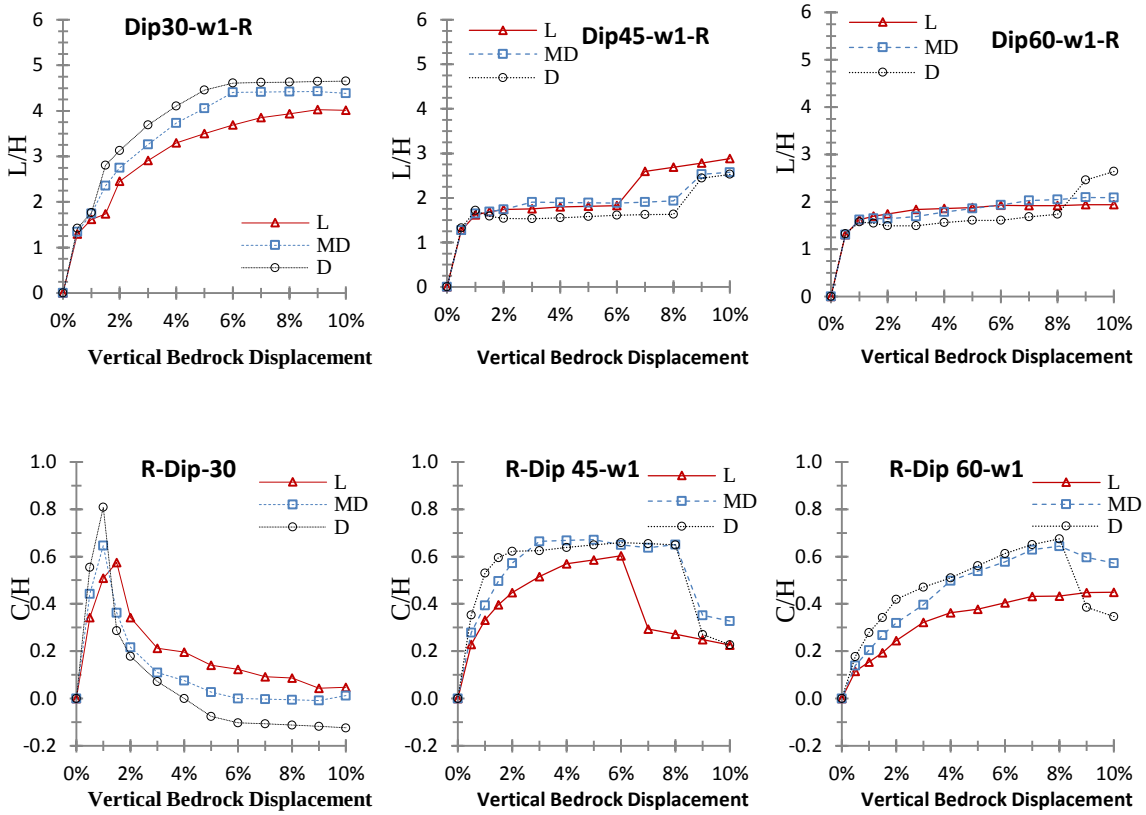

Figure 4-10 Normalized Length (L/H) and center (C/H) of distorted zone for saturated sand subjected to reverse fault for dense, medium dense, and loose sand vs. vertical bedrock displacement.

For the case of ***reverse faults***, results on figure 4-10 reflect a higher degree of sensitivity of the fault prepagation mechanism to the magnitude of the imposed vertical bedrock displacements. The following observations pertain to the reverse faults:

1. For reverse faults with a dip angle of 30˚, the length of the distorted zone intially increases in a steep manner until the primary shear band reaches the top surface at bedrock displacements of about 1%H for dense and medium dense sand and 1.5%H for loose sand. At these bedrock deformations, the normalized length of the failure zone (L/H) is in the order of 1.7, irrespective of the soil relative density, and the

center of the distorted zone is at C/H equal to 0.6 to 0.8. With additional fault deformations, the formation of a back-thrust initiates increasing the length of the distorted zone gradually and bringing the center of the zone closer to the center of the fault zone. The L/H keeps increasing and the C/H keeps decreasing until the back-thrust reaches the top surface at fault deformations of 6%H for dense and medium dense sand and 9%H for the loose sand case. Once the backthrust reaches the surface, the fault propagation mechanism stabilizes at maximum L/H values that are in the order of 4.0 to 4.6. The locations of the back-thrust in the dense and medium dense sand cases are farther than the case of loose sand, resulting in a larger length of distorted zone for the dense sand case.

2. For reverse faults with a dip angle of 45˚, the length of the distorted zone increases with increasing bedrock displacement until the first shear band propagates to the surface and stabilizes at a vertical bedrock displacement of $U_2 \approx 1\%H$ and the center of the distortion zone is on the side of the first shear band. Then with the formation of the second shear band the length of the distorted zone increases until it reaches the top surface at U2≈3%H after which it stabilizes. The length of the distorted zone increases slightly until U2=6% for loose sand and U2=8% for dense and medium dense sand after which the distortion suddenly increases due to shear strains that start to accumulate at the top of the scarp (moving block) causing the center to drift towards the direction of the moving wall side.
3. For reverse faults with a dip angle of 60˚, the length of the distorted zone increases in a steep manner until the shear band reaches the top surface at bedrock displacements in the order of 1%H after which it stabilizes at an L/H of about 1.5.

In the absence of any back-thrusts, the normalized center of the distorted zone (C/H) tends towards the fixed wall side and increases systematically from 0.15 (loose) and 0.28 (dense) at a normalized fault displacement of 1% to 0.43 (loose) and 0.67 (desne) at a normalized displacement of 8%. It is worth noting that this drifting of the center of the distorted zone to the right is not associated with an increase in the length of the distorted zone as the fault displacement increases.

4.3 Effect of Fault Breccia Thickness

4.3.1 Ground Surface Deformation Profile

The fault breccia zone width may vary from a grain-size scale to several meters. In order to investigate the effect of the breccia zone on the results, the width of the breccia zone of the reference model was varied from the base case of 1m to values of 3m and 10m.

The effect of the fault width on the ground surface deformation profiles is illustrated in figure 4-11 for the case of normal faults with dip angle of 30˚ and 45˚, for the specific case of dense sands. Results of ground surface deformation profiles for other relative densities are included in the Appendix. It should be noted that in the finite element model, the width of the breccia zone was modeled numerically by the width within which the fault displacement occurs.

Normal Fault Case:

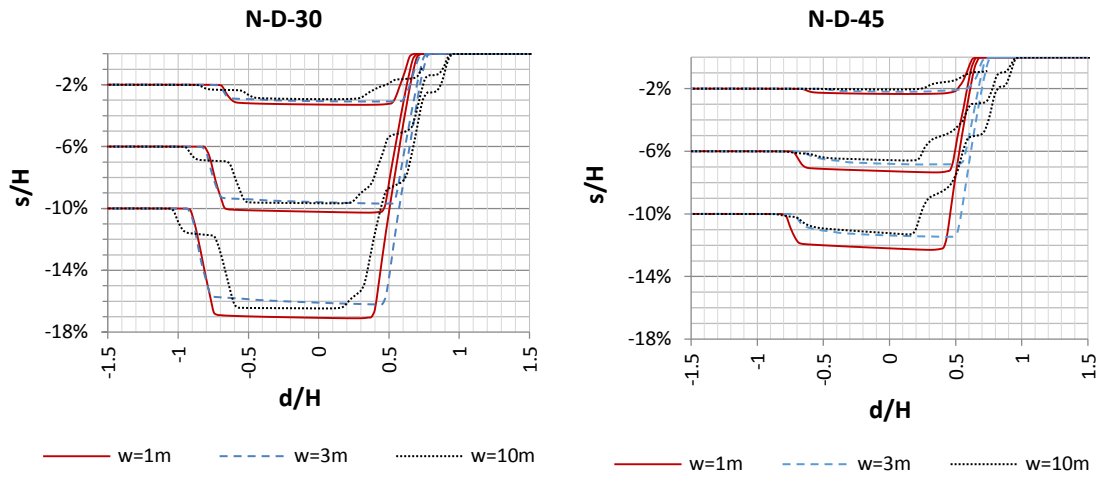

Figure 4-11 Ground surface deformation profile for dense sand layer subjected to normal fault under different fault shearing widths

Results in figure 4-11 indicate that the ground surface deformation profiles are realtively similar for cases involving fault zone widths of 1m and 3m except for some minor differences in the steepness of the profiles and the lateral extent of the ground surface deformation. However, the ground surface deformation profiles for the case with a fault width of 10m exhibited surface deformations that are uneven and rough, and were accompanied with grabens that extended laterally to a larger extent than the cases with the smaller fault widths. Moreover, at relatively larger bedrock displacements, the depths of the grabens were found to be relatively smaller for cases involving the wider fault zones (w = 3m and 10m) compared to the base case with the fault width of 1.0m.

The distribution and extent of plastic strains are shown in figure 4-12 for the normal fault cases with dip angles of 30 degrees and 45 degrees. For larger fault widths, results indicate the formation of multiple shear bands which propagate to the surface

causing uneven surface deformations. As in the cases involving a fault width of 1.0m, it is observed that the secondary shear bands that formed the graben for cases involving the larger fault widths of 3m and 10m were more visible for the shallower fault dip angle of 30 degrees.

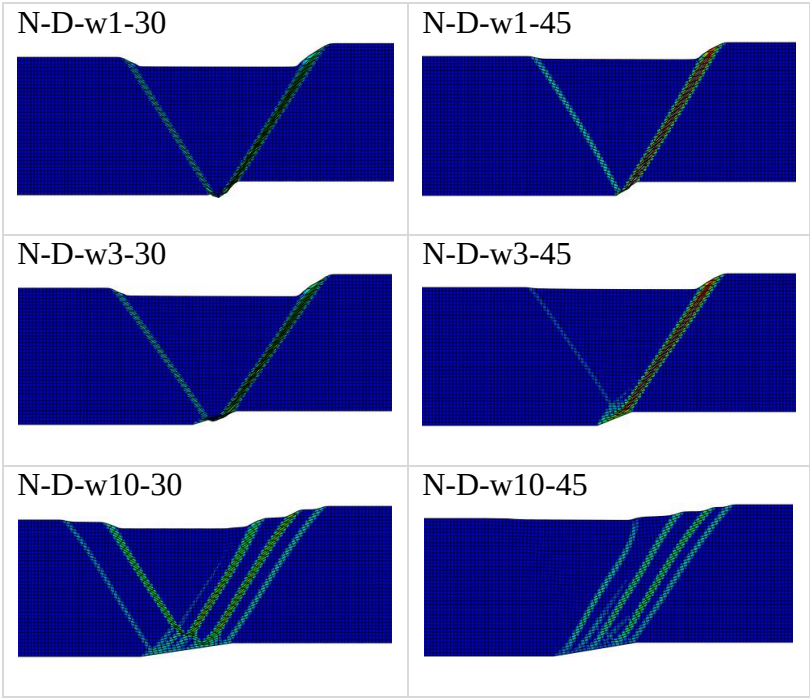

Figure 4-12 Plastic shear strains for normal fault case under different fault widths

Reverse Fault Case:

The ground surface deformation profiles for reverse fault cases with different breccia zone widths are presented in figure 4-13 for dense sand cases having different fault dip angles. Results on figure 4-13 show a 2-step displacement for a fault width of 3m and dip angles of 45˚ and 60˚. A 2-step displacement also appears for the case with a fault width of 10m for fault dip angles of 30˚ and 45˚ and a 3-step displacement for a fault with a dip angle of 60˚.

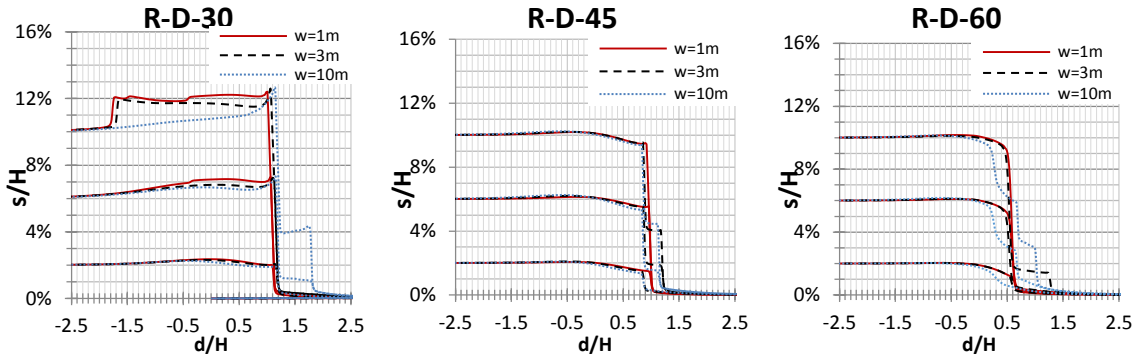

Figure 4-13 Ground surface deformation profile for dense sand layer subjected to reverse fault under different fault shearing widths.

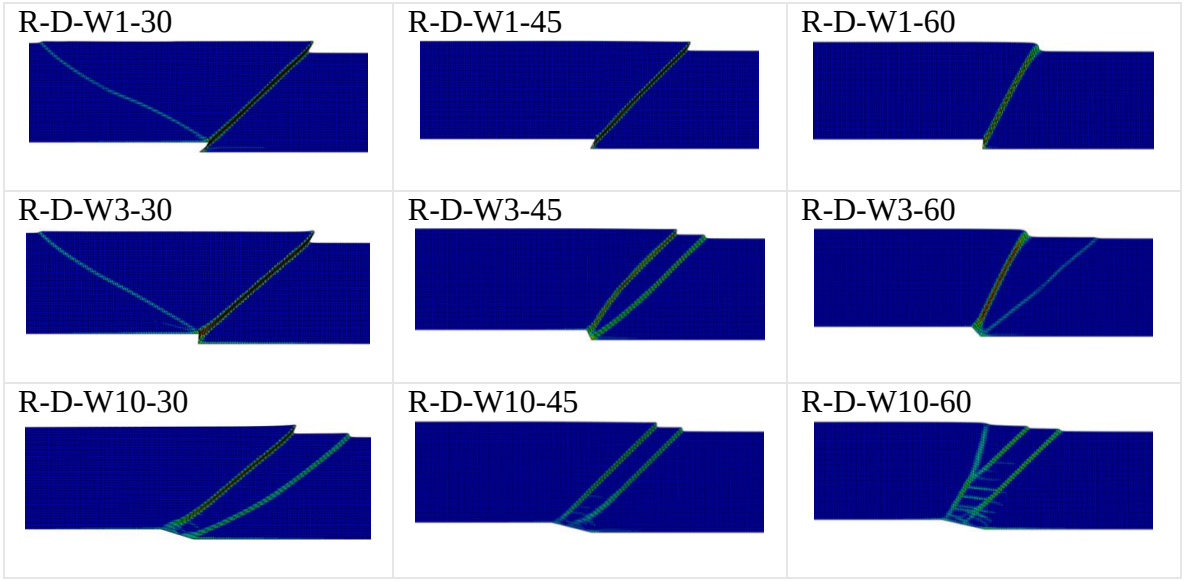

Figure 4-14 Plastic shear strains for reverse fault case under differnet dip angles and widths

A comparison between the surface deformation profiles for the three fault widths in figure 4-14 indicates that the locations of the peak inclinations for the ground surface for the case of a 1-m wide fault coincide or differ slightly from the locations of the cases with fault widths of 3m and 10m. This could be related to the fact that the initial primary shear

band forms at a more-or-less same location for different fault width width cases. For larger widths, additional shear bands are formed and result in multi-step deformation profiles.

An analysis of the results in figures 4-11 to 4-14 leads to the following observations when it comes to the effect of the fault width on the fault propagation mechanism for normal and reverse faults:

1. For a fault dip angle 30˚, the ground surface deformation profiles are almost identical for cases with fault widths of 1m and 3m. On the other hand, the ground surface deformation profile for the case with a fault width of 10m exhibits a 2-step displacement and a farther outcrop location (1.5m for width 10m vs. 1.1m for w=1m and w=3m). A pop up structure is formed for the cases with fault widths of 1m and 3m unlike the case of a 10m-wide fault where a back-thrust was not encountered.
2. Similarly, for dip angles of 45˚ and 60˚, the outcrop location corresponding to width of 3m and width of 10m are farther than the case of width 1m.
3. A comparison between the normal and reverse fault cases indicates that multiple shear bands are more likely to be formed for normal fault cases than reverse fault cases. For normal fault cases, lower bedrock displacements are required for the shear bands to propagate to the surface by analogy to active earth pressure conditions. Therefore more shear bands are formed for the normal fault cases.
4. Similarly for the case of reverse faults (figure 4-11) the ground surface inclinations are lower for w=10m and exhibit lower values. That could be attributed to the wider shearing zone that requires a higher displacement for the rupture to propagate to the ground surface.

4.3.2 Extent and Location of the Shear Surface/Band

The normalized shear band locations (S/H) as measured from the center of the fault are plotted on figure 4-15 for the cases involving reverse and normal faults with varying fault widths of 1m, 3m, and 10m for dense, medium dense, and loose sands. Except for back-thrusts, the locations of both primary and secondary shear bands that propagated to the surface are included in the figure.

Results on figure 4-15 indicate that the cases involving fault widths of 3m and 10m are accompanied by a larger number of shear bands, compared to the base case with a fault width if 1.0m. The locations of the shear bands for fault widths of 3m and 10m drift from the locations of the shear bands for theg case with a fault width of 1m by a range of 0.01H to 0.7H. The shear bands for the cases with widths of 10m are much more dispersed than cases with fault widths of 1m and 3m respectively.

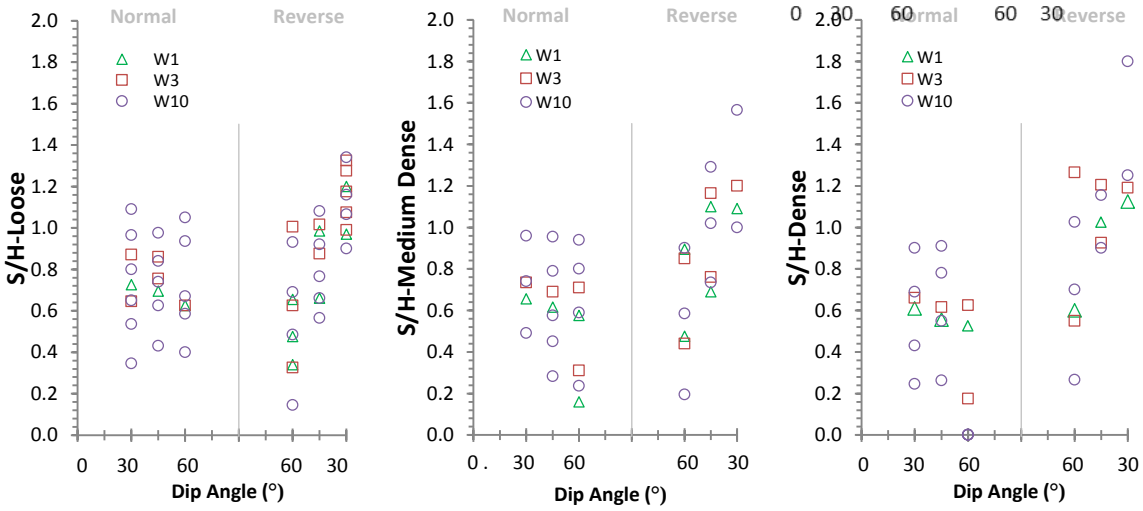

Figure 4-15 Normalized shear band locations for dense, medium dense, and loose sand for different fault shearing widths vs. the fault dip angle.

4.3.3 Bedrock Displacement Required for Rupture to reach the Surface

Figure 4-16 shows the normalized critical bedrock displacement (d_{cr}/H) required for the primary shear band to reach the surface for dense, medium dense, and loose sand for cases with fault widths of 1m, 3m, and 10m.

For the case of dense sand, the d_{crit}/H values for widths of 1m, 3m, and 10m are almost the same (≈0.1%) for the normal fault cases. For reverse fault cases, as the shearing occurs over a wider zone, a higher bedrock displacement is required for the rupture to propagate to the surface. Considering a width of 10m, results for the cases involving medium dense and dense sands indicat the normalized critical bedrock displacements (~1.3% for dip angle of 60˚, ~1.7% for dip angle of 45˚, and ~2.4% for dip angle of 30˚) are greater than those observed for the cases involving of w=1m and 3m (~1.1% for dip angle of 60˚, ~1.5% for dip angle of 45˚, and ~2% for dip angle of 30˚). These differences increase slightly for the case of loose sand where slightly higher values of d_{crit}/H are required (see figure 4-16). These results can be explained by the fact that as the fault width increases, the fault displacement is applied over a shallower slope and in a more distributed manner. Therefore, shearing occurs over a wider region with lower values compared to narrower regions requiring a higher displacement to reach the surface.

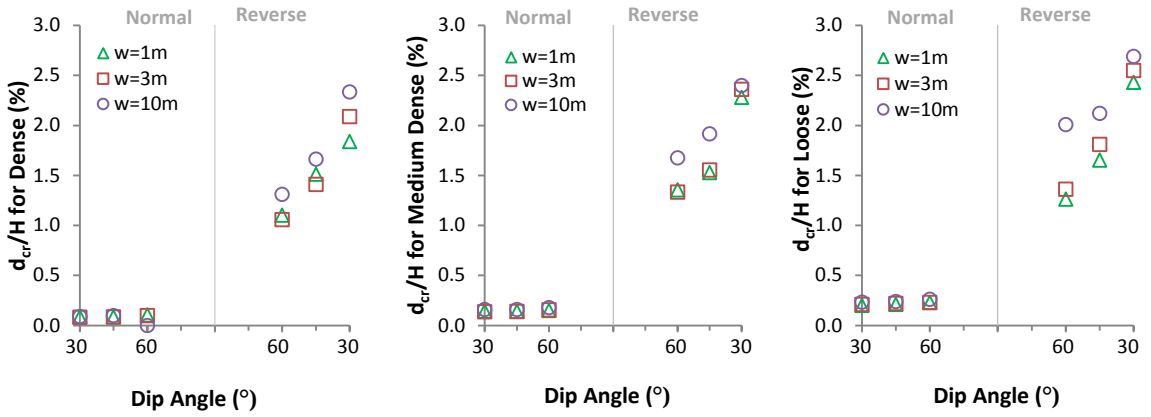

Figure 4-16 Critical bedrock displacement for the shear band to propagate to the surface for dense, medium dense, and loose sand under different fualt widths and dip angles

4.3.4 Length and Center of the distorted zone

Figure 4-17 shows the normalized length of the distorted zone vs. the fault dip angle for different fault widths and different sand types. Results indicate that the length of the distorted zone is observed to be slightly larger for fault widths of 10m compared to cases with smaller fault widths. This observation holds irrespective of the fault type (reverse vs normal), dip angle, and sand relative density. The only exception are reverse fault cases with a dip angle of 60 degrees where the fault width did not affect the length of the distorted zone. The slightly larger L/H for the cases involving w = 10m is related to the fact that shearing in such cases occurs over a wider length and displacement is applied in a more distributed manner. As a result, the soil undergoes more distortion before the shear band reaches the top surface and stabilizes.

A detailed analysis of the data in figure 4-17 shows that the length of the distortion zone varies slightly between the different widths for the cases involving normal faults. for the cases involving reverse faults, the difference in the length of the distortion zone is larger

for the case of dense sand with the formation of shear bands at farther distances from the center.

It can be observed that because shearing occurs over a wider zone for the case of a normal fault with a width of 10m, the rupture will distort over a larger length before it propagates to the surface. Loukidis et al. (2009) related the critical bedrock displacement d_{crit} to the length of the distorted zone. Since a width of 10m requires a larger bedrock displacement for the rupture to propagate to the surface and since the width simply occurs over a much wider zone compared to the case of w=1m and w=3m, the length of the distorted zone is larger for a width of 10m.

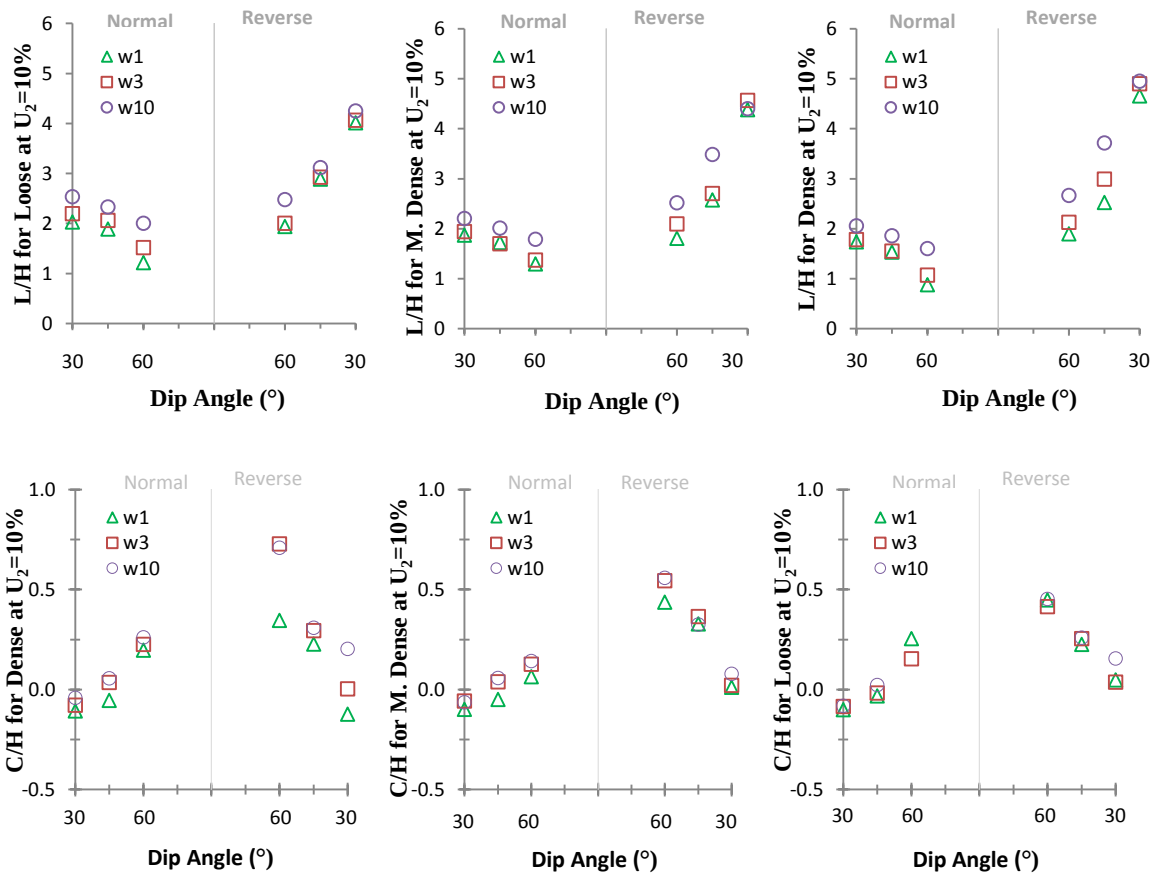

Figure 4-17 Normalized length and center of distorted zone for dense, medium dense, and loose sand for different fault shearing widths vs. dip angleResults showing the variation of the location of the center of the distorted zone with the fault width and the fault dip angle (figure 4-17) indicate that the normalized location of the center of the fault width (C/H) is relatively insensitive to the width of the fault zone. Except for slight increases that were observed in C/H as the fault width increases for the cases involving reverse faults with a dip angle of 60 degrees and a dense sand profile, this conclusion could be observed to be valid for all other cases analyzed.

The effect of the width of the fault on the normal fault propagation mechanism is best portrayed in figure 4-18, which shows how the length and center of the distorted zone change with the magnitude of the fault displacement at bedrock.

For the normal fault with the shallower dip angle of 30 degrees, results indicate that the effect of the width of the fault is only reflected through slight increases in the lengths of the distorted zone for the cases with the larger fault widths. For example, the length of the distorted zone increases by about 5% to 10% as the fault width increases from 1m to 3m and by about 20 to 30% as the width is increased from 1m to 10m. Since graben structures formed in all cases involving a normal fault with a dip angle of 30 degrees, the normalized location of the center of the distorted zone was around zero, but was slightly larger for the cases involving a larger fault width since most of the distortions in these cases are spread on the hanging wall of the soil.

For normal faults with a steeper dip angle of 45 degrees, results indicate more-ore-less similar distortion zones for the cases involving fault widths of 1.0m and 3.0m. In both cases, the graben structure does not form until a bedrock displacement of about 1.0%H is

achieved. At this displacement, the center of the distorted zone (C/H) drops from 0.5 to 0 as due to the formation of the graben. For the case involving the fault width of 10m, the formation of multiple secondary shear bands results in sudden jumps/steps in the length of the distorted zone and in the location of the center of the distorted zone (see Figure 4-18). For normalized bedrock displacement exceeding 3%H, the length of the distorted zone for the 10-m wide fault is about 20% larger than that corresponding to cases with fault widths of 1 and 3m.

Normal Fault Case

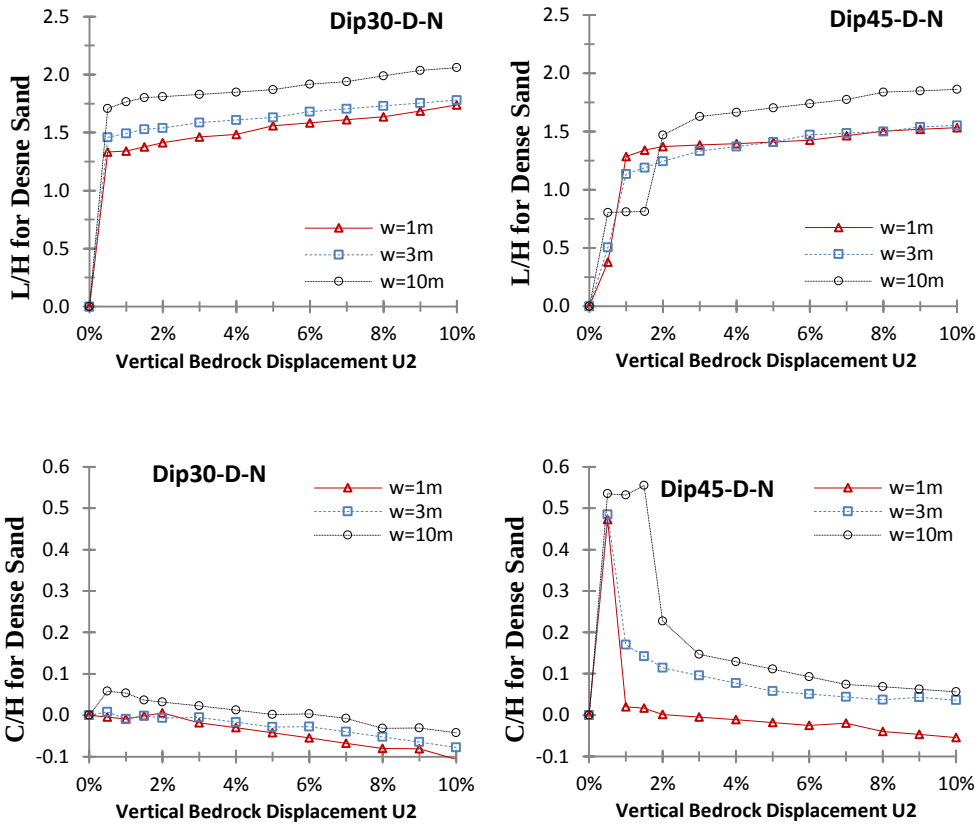

Figure 4-18 Normalized length and center of distorted zone for dense, medium dense, and loose sand for normal fault with different fault shearing widths vs. the vertical bedrock displacement

In the reverse fault cases, results on figure 4-19 show that in the case where the dip angle of the fault is 30 degrees, the width of the fault seems to have a relatively minor effect on the variation of L/H with the bedrock displacement. Since a pop-up structure is formed for the cases with fault widths of 1m and 3m, results indicate that the center of the distorted zone drifts towards the center of the fault. Since larger fault widths requires a higher bedrock displacement for the shear band to propagate to the surface, the center of the distorted zone (C/H) for the case involving a fault width of 3.0m is observed to drift towards 0 at a later stage in the deformation process. In the case involving a reverse fault with a width of 10m and a fault dip angle of 30 degrees, the center of the distorted zone remains on the non-moving side of the fault, since the plastic strain plot does not show a clear formation of a back-thrust in the overlying soil.

For a dip angle of 45˚, one shear band is formed for the case with a fault width of 1m. For cases with fault widths of 3m and 10m, 2 shear bands form to the direction of the fixed wall side. With the formation of several secondary shear bands the length of the distorted zone increases and then stabilizes and the center of the distorted zone shifts towards the direction of new shear band. For the case of a fault width of 10m, the first shear bands reaches the surface at 1% after which the length of the distorted zone increases. Then a secondary shear band is formed and it reaches the surface at 5%H after which the length for the distorted zone stabilizes at an L/H of about 3.7. For a fault width of 3m, the first shear band reaches the top surface at 1%H and the second at 4%H, with a maximum normalized distortion length of about 3.0. For the base case with a width of 1.0m, L/H was about 1.6 up to a fault deformation of 8.0%. After this deformation level, an unexplained sudden increase in L/H occurs reaching a value of 2.5 at a fault deformation of 10%. It

should be noted that for the case involving fault widths of 3.0 and 10.0m, sudden reductions are observed in the locations of the center of distorted zone (C/H) as the secondary shear bands reached the ground surface (figure 4-19).

For the case involving reverse faults with a dip angle of 60 degrees, results indicate that the lengths of the distorted zone was consistently higher (by about 50%) in the case of the 10-m wide faults compared to the 1.0-m wide fault. This observation is true over most of the range of bedrock deformations. For the 3-m wide fault, L/H was slightly higher (by about 15%) that the corresponding L/H for a fault width of 1.0m.

Reverse Fault Case:

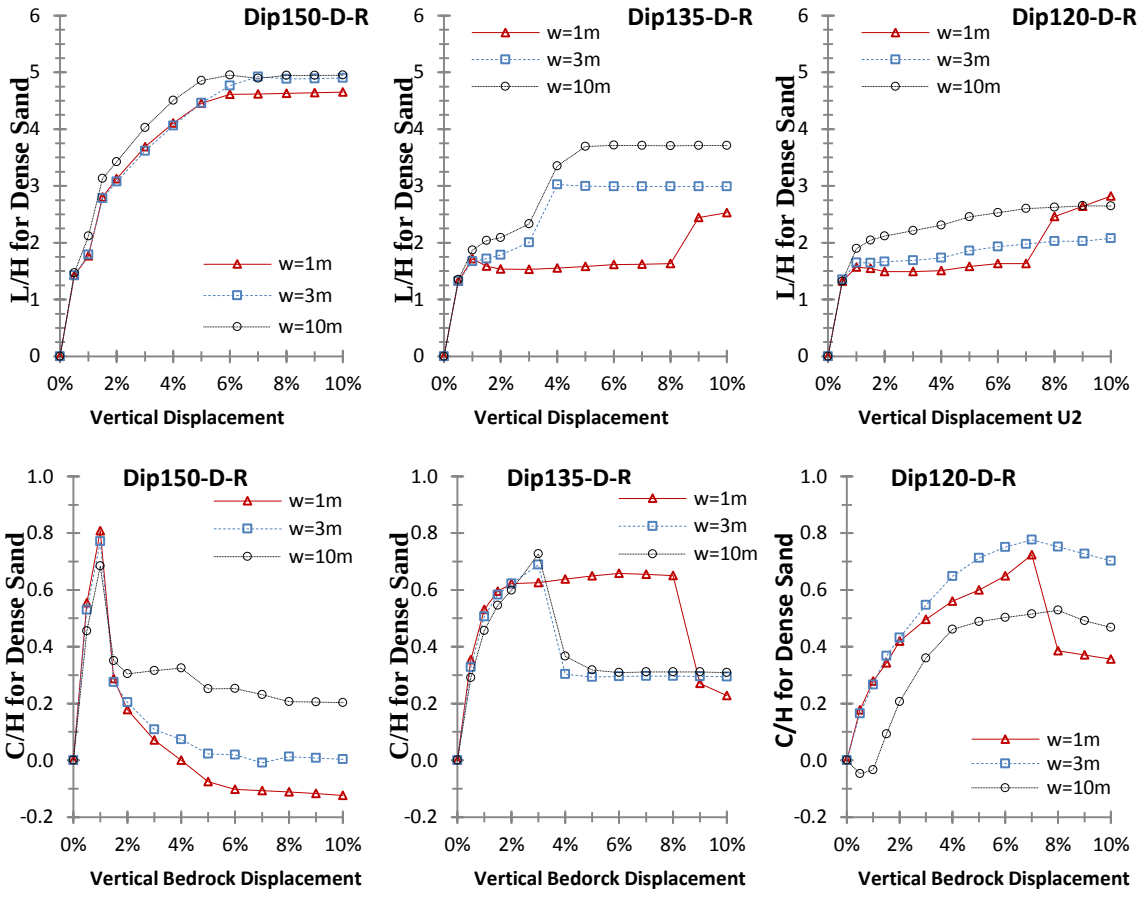

Figure 4-19 Normalized length and center of distorted zone for dense, medium dense, and loose sand for reverse fault with different fault shearing widths vs. the vertical bedrock displacement

4.4 Effect of Height of Overlying Soil Layer:

4.4.1 Ground Surface Deformation Profile

In all the analyses that were conducted in the previous sections, the height of the overlying soil was assumed to be 20m and the results were normalized with regards to this soil height. The objective of this section is to investigate whether the results of the fault propagation analyses are still valid for other soil overburden heights. In other words, it is important to check whether the normalized ground surface deformation profiles are similar for the different soil heights.

The FE analyses that were conducted in Sections 4.2 and 4.3 with a soil height of 20m were repeated for cases involving soil heights H of 40m and 80m. Results pertaining to the cases of normal faults of dip angles 30 degrees and 45 degreees indicate that the normalized ground surface deformation profiles are similar irrespective of the height of the overlying soil (figure 4-20).

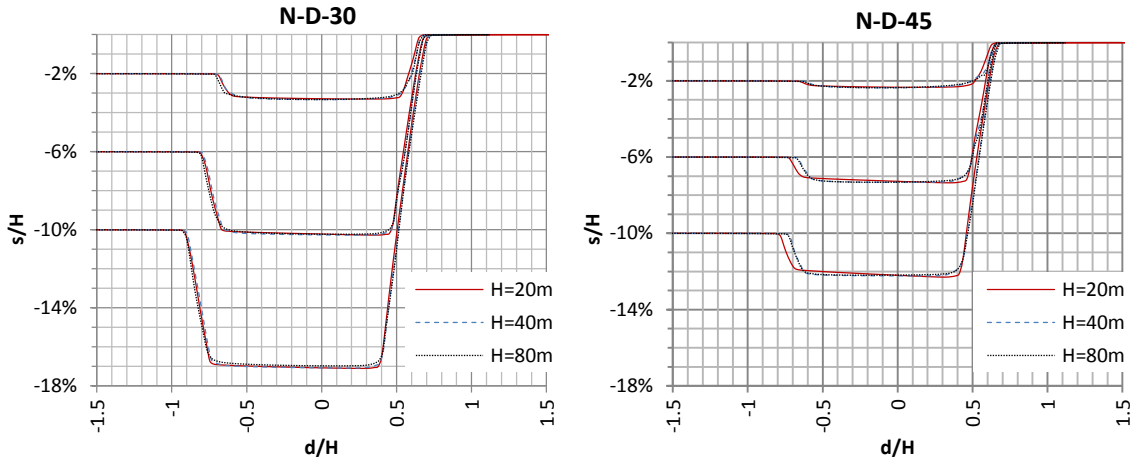

Figure 4-20 Normalized ground surface deformation profiels for dense sand subjected to normal fault of dip angles 30° and 45°

For the cases involving reverse faults, the normalized ground surface deformation profiles for dense sand subjected to reverse fault under dip angles 30˚, 45˚, and 60˚ were determined and plotted in figure 4-20. Results indicate that the normalized ground surface deformation profiles could be considered to be generally similar for a dip angle of 30˚ but not for the steeper dip angles of 45˚ and 60˚. These results could be explained by analyzing the distribution of plastic shear strains for reverse fault cases in dense sands (figure 4-21). For caes with a dip angle of 30˚, a primary shear band forms at the same location, irrespective of the height of the overlying soil. However, for the steeper dip angles, cases with the larger soil heights were accompanied by the formation of multiple shear bands. For example, in the cases involving H=80m and dip angles 45˚ and 60˚, a secondary shear band in the same direction of the primary shear band is formed at a certain bedrock displacement causing a 2 step deformation profile unlike the case of an overlying soil layer thickness of height 20m that included a single shear band. As a result, the ground surface deformation

profiles in these cases only normalize at low bedrock displacements. For larger soil layer thicknesses the shear band is more dispersed at high bedrock displacements.

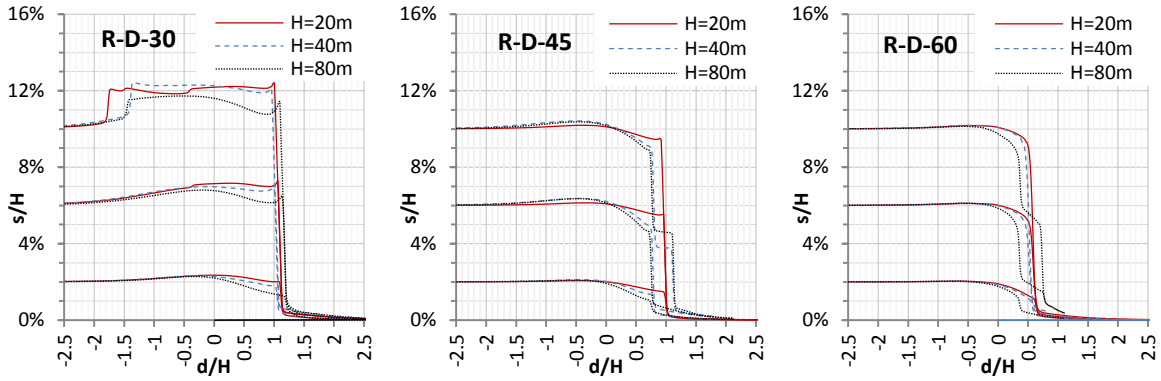

Figure 4-21 Normalized length and center of distorted zone for dense, medium dense, and loose sand for normal fault with different fault shearing widths vs. the vertical bedrock displacement

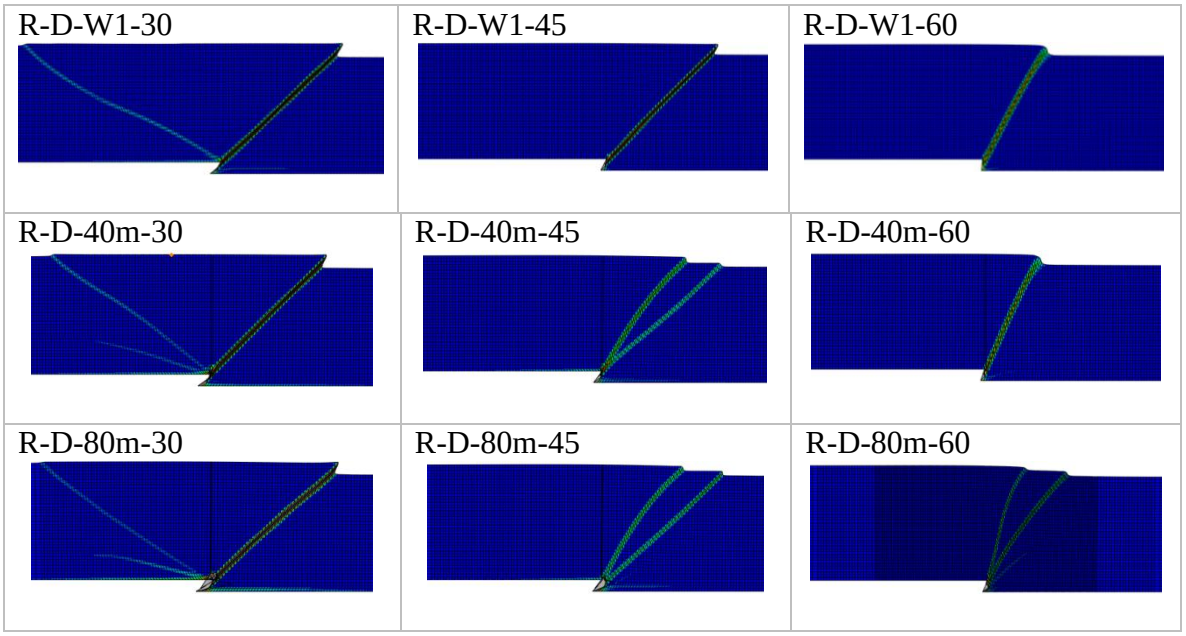

Figure 4-22 Plastic shear strains for reverse fault case of different dip angles and soil layer thickness

It could thus be concluded that for the case of reverse faults, the ground surface deformation profiles for different soil heights normalize except for the conditions where 2 shear bands form in the direction of the fixed wall side. At low vertical bedrock

displacements the ground surface deformation profiles normalize. For steep dip angles, as the vertical bedrock displacement increases, a secondary shear band in the same direction of the primary shear band forms. It should be noted that as the depth increases, the soil strength properties (modulus of elasticity, dialation angle, etc.) generally increase with depth. As a result, it is expected that at differences in the fault propagation mechanism could exist as a result of changes in the overlying soil thickness, resulting in some descrepancies in the normalized ground response.

4.4.3 Bedrock Displacement Required for Rupture to reach the Surface

Figure 4-24 shows the normalized critical inclined bedrock displacement value for each of the 3 sand types for cases of sands with different heights. The critical bedrock displacements for the normal fault cases are relatively small $\approx 0.1H - 0.3H$ and are not sensitive to the thickness of the overlying sands. On the other hand, for the reverse fault cases, it is observed that greater soil thicknesses exhibit higher d_{crit}/H values. This is explained by the fact that soils at larger depths exhibit higher stiffness and lower peak friction and dilation angles since the soils are are more confined and constrained. So a higher bedrock displacement is required for the shear bands to reach the surface. The difference between the critical bedrock distances observed for different soil heights is larger for loose sands which require additional fault movements for the fault to reach the surface. It could be concluded that for the cases involving reverse faults, the height of the overlying soil plays a significant role in defining the bedrock displacements that are required for the fault to physicall propagate to the surface. Normalizing the required displacement by the height of the overburden soil does not lead to a constant d_{cr}/H in the different cases analyzed.

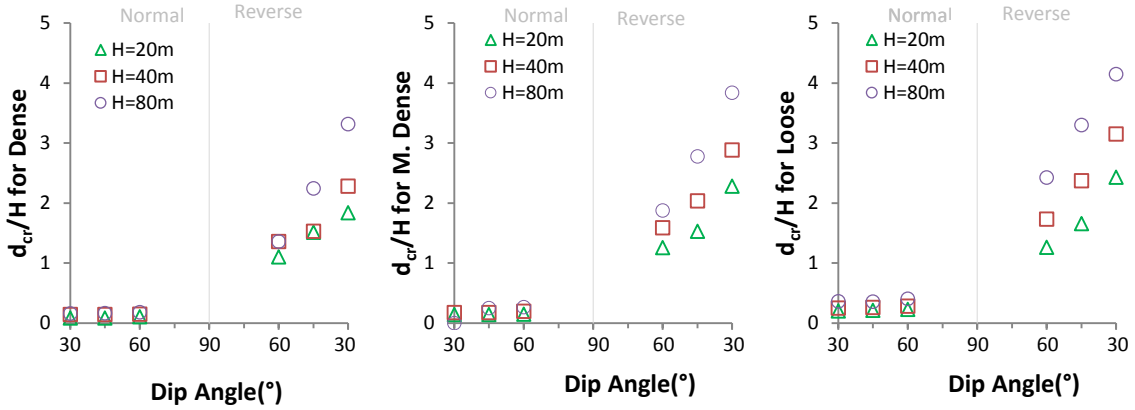

Figure 4-24 Critical bedrock displacement for shear band to reach the surface for different dip angles and soil layer thicknesses

4.4.4 Length and Location of Distorted Zone

Figure 4-25 shows the different normalized lengths of the distorted zone for heights of 20m, 40m, and 80m vs. the fault dip angle. Results indicate that the normalized lengths of the distorted zones are more-or-less similar and independent of the soil height for cases involving normal faults and reverse faults in loose sands only. This is attributed to the fact that the ground surface deformation profiles normalize for these cases, irrespective of the soil height..

For the cases of dense and medium dense sands, the length of the distorted zone differs between the different soil layer thicknesses. The ground surface deformation profiles do not completely normalize for these 2 cases, although the effect of the soil height could be considered to be relatively insignificant.

In general, the normalized length of the distorted zone for H=80m is found to be larger than for H=40m and H=20m, respectively. This is attributed to the fact that for a height of

80m, the shear band requires more displacement to propagate to the top surface. For reverse faults with dip angles of 45 and 60 degrees, since the ground surface deformation profiles were different and didn't normalize, the length of the distorted zone was slightly affected. It is worth noting that the normalized locations of the center of the distorted zone were also relatively insensitive to the soil height.

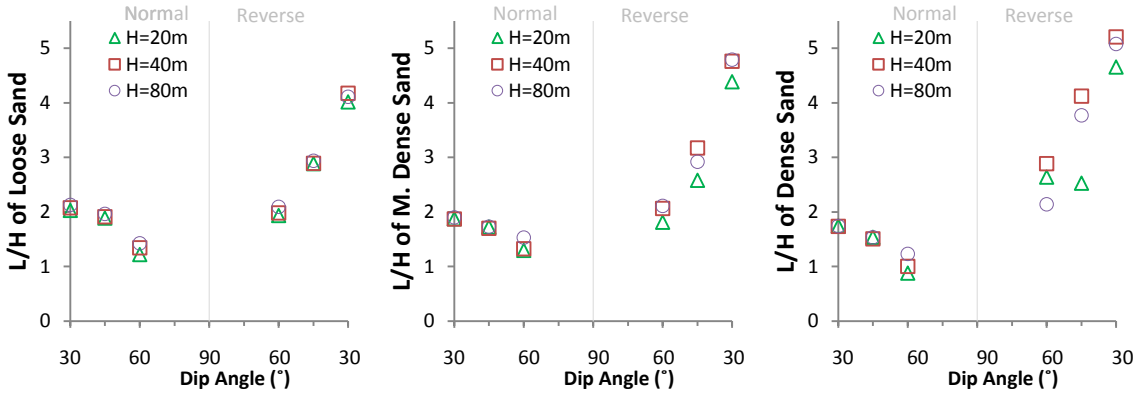

Figure 4-25 Normalized length of distorted zone vs. dip angle for different overlying soil thickness

The variations of the normalized length and center of the distorted zone with fault displacement for the cases involving normal faults with different soil heights are presented in figure 4-26. Irrespective of the applied bedrock displacement, results on figure 4-26 indicate that the length and location of the center of the distorted zone are not affected by the height of the soil above bedrock. For the case involving faults with dip angles of 60, slight variations in L/H and C/H were observed the case of H = 80m, compared to the other cases.

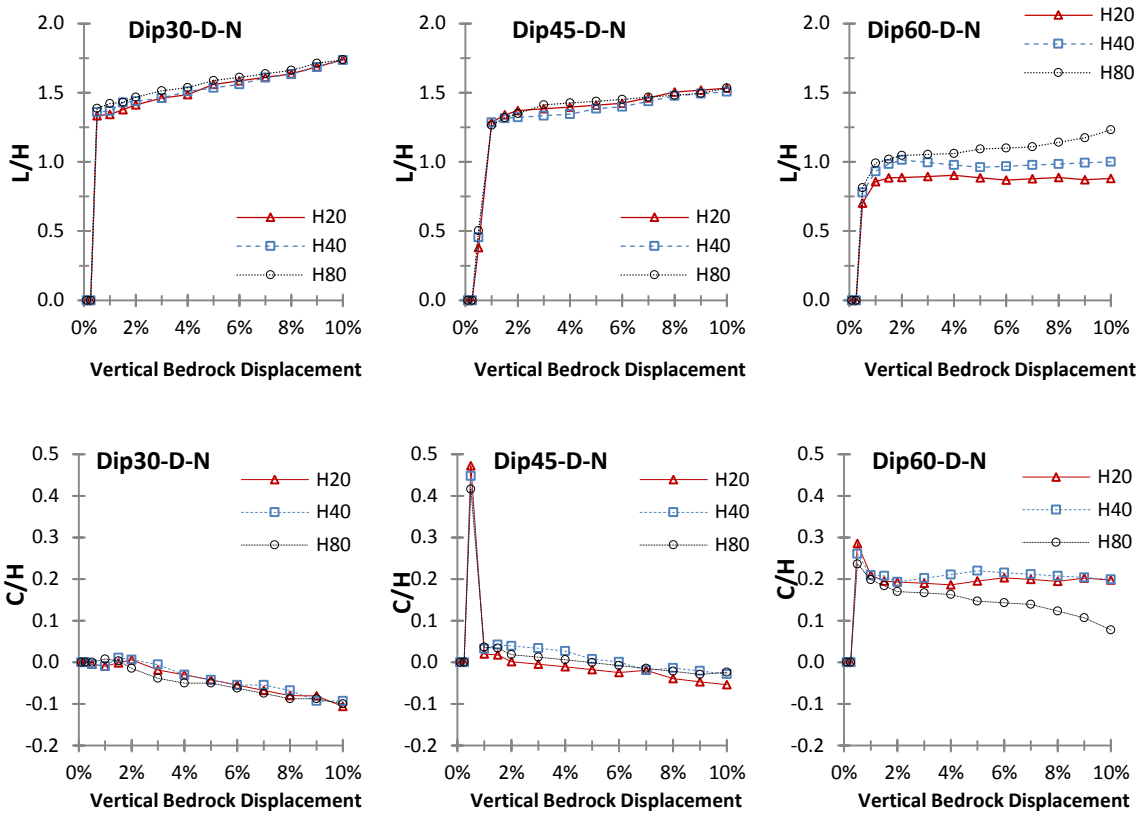

Figure 4-26 Normalized Length and center of distorted zone for different soil layer thicknesses for normal fault case

For the cases involving reverse faults (figure 4-27), the normalized length of the distorted zone is found to be dependant on the ground surface deformation profile. As a result, minor differences in the the lengths of the distorted zones are observed for different soil height cases. The difference in the ground surface deformation is larger for the dense sand cases compared to cases with loose sands and medium dense sands (see Appendix). Results in figure 4-25 indicate that variations of the normalized length and center of the distorted zone with bedrock displacement are more or less independent of the soil height for the cases involving dip angles of 30 and 60 degrees. For the particular case of a dip angle of 45 degrees, the variation of L/H and C/H with bedrock displacement are very similar for the

cases with H = 40m and 80m. However, the results for the 20m-case show a completely different pattern. The is is attributed to the fact that he cases of H=40m and H=80include the formation of a 2 step displacement due to the formation of 2 shear bands in the direction of the fixed wall

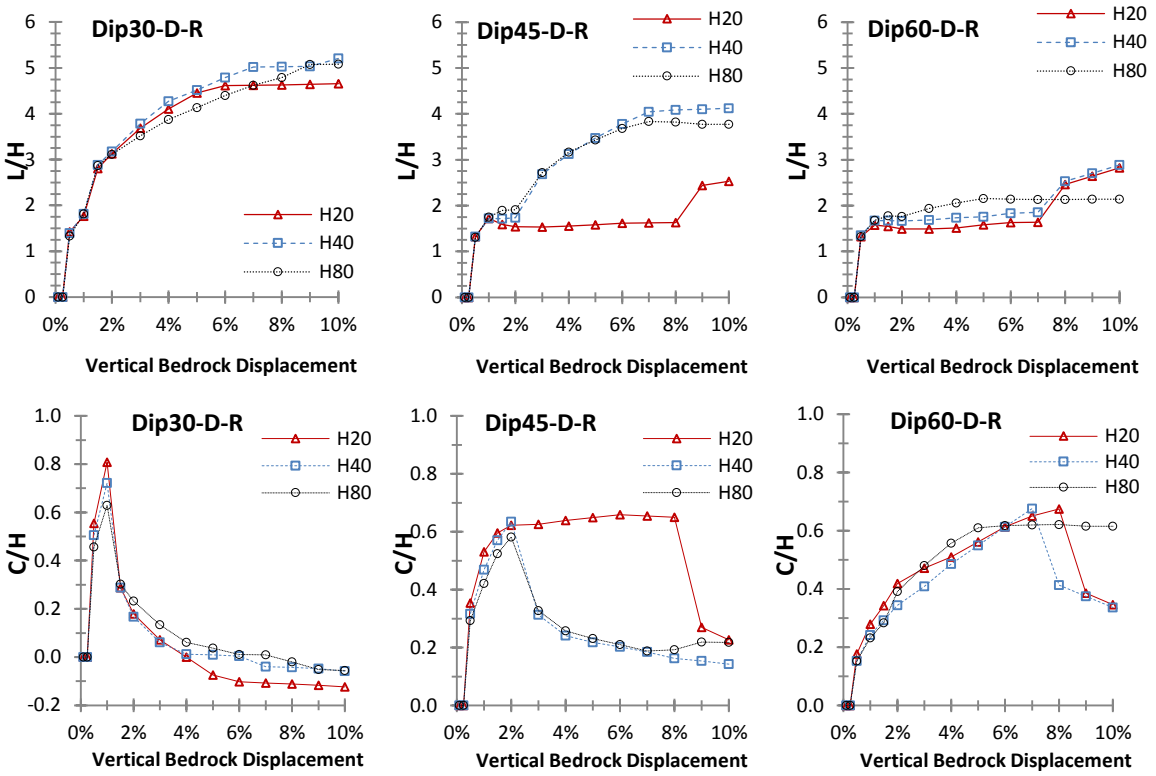

Figure 4-27 Normalized Length and center of distorted zone for different soil layer thicknesses for reverse fault case

CHAPTER 5

CONCLUSIONS AND FURTHER RESEARCH

5.1 Introduction

This chapter presents a review of the main conclusions and findings resulting from thcomprehensive investigation of the finite element model of the fault propagation in offshore saturated sand. The model consists of a saturated sand layer and includes the elasic-plasitc modified mohr coulomb constitutive model to capture the adequate behavior of the sand. The cases considered included different configurations of the sand relative density, the fault breccia zone, and the sand layer thickness. The following chapter highlights the conclusions based on the assemsement of the results of 90 simulations of the different configurations. Finally, the following chapter includes recommendations and proposals for future research.

5.2 Conclusions

In view of the 90 simulations conducted to model the mechanism of the the fault propagation on offshore saturated sand under different sand relative densities, the following conclusions can be drawn:

5.2.1 Dip Angle and Relative Density:

Grabens are more likely to be formed for shallow dip angles. Unlikely, for steep dip angles only one failure plane is formed. The width of the graben is larger for cases including loose sand and the height of the scarp of the graben is larger as well for these

cases. Similarly, pop up structures are formed for reverse fault for cases including shallow dip angles at certain bedrock displacements resulting from the formation of a backthrust. The scarp height and width of the pop-up structure is smaller for the case of loose sand.

In reverse fault cases, only one primary shear band is formed in case of dense sand independently of the dip angle. As the relative density decreases, multiple shear bands are formed causing the formation of a 2-step displacement in medium dense sand. Unlikely, the surface deformation for loose sand case is continuous.

The locations of the primary shear bands are farther for lower relative densities in cases of normal fau lt and vice versa for reverse fault case.

For medium dense sand and at certain bedrock displacements a secondary shear band on the same direction of the fixed wall is formed for the case of reverse fault for steep dip angles.

The normalized locations of the primary shear bands for the case of reverse faults are more sensitive to the sand density and the dip angle of the reverse fault. In fact, the normalized locations of the shear bands from the center of the fault tend to be the highest for dense sands, with differences between the loose and dense cases being the highest for the steeper dip angles of 45 and 60 degrees.

The locations of the secondary shear bands that were observed in the reverse fault cases involving loose and medium dense sands

In the case of normal fault, the shear band reaches the top surface at small values of bedrock displacement irrespective of the sand relative density and the dip angle. However, results for the reverse fault case, indicate that the required bedrock displacement for the rupture to reach the surface is large compared to normal fault case and is larger for shallower dip angles and lower relative densities.

The results of the comprehensive investigation of the fault propagation indicate that the length of the distorted zone is more sensitive to dip angles than relative density. The length of the distorted zone increases as the shear band propagates to the surface and in cases of formation of secondary shear bands, the length of the distorted zone increases abruptly with the propagation of the secondary shear band to the surface, after which the length stabilizes. Shallower dip angles are accompanied by larger length of distorted zone and that is explained by the formation of graben or pop up structures at certain bedrock displacements.

The location of the center of the distorted zone is directly related to the length of the distorted zone and the formation of graben and pop-up structure.

The center of the distorted zone is in the region of the shear band and shift towards the direction of the secondary shear band in cases of formation of secondary shear bands. In case of formation of pop-up structure or graben the center of the distorted zone drifts towards the center of the fault.

5.2.2 Fault Breccia Thickness:

Larger fault widths are accompanied with the formation of multiple shear bands which propagate to the surface causing uneven surface deformations. These multiple shear bands are more likely to be formed for the normal fault case than reverse fault case. The deformation profiles of larger fault widths exhibit lower inclination values, farther outcrop locations, and wider grabens. Results for reverse fault cases including large fault width indicate the formation of multiple step displacement for larger fault widths and these steps increase for steeper dip angles.

The locations of the primary shear bands for the different fault widths coincide with minor differences for reverse fault case. However, secondary shear bands are forrmed for larger widths at certain bedrock displacements.

The critical bedrock displacement is insensitive of the fault breccia width for the normal fault case. For reverse fault cases, larger fault widths require larger bedrock displacements for the shear bands to reach the surface and this difference is more significant for lower relative densities.

Results indicate that the length of the distorted zone varies slightly between the different results for different fault widths for the normal fault case. However, for the reverse fault cases, the difference in the length of the distorted zone for different fault widths is more significant and larger fault widths are accompanied by larger lengths of distorted zones.

The location of the center of the distorted zone is relatively insensitive to the fault width. The location of the center of the distorted zone is farther from the center for larger widths in general.

5.2.3 Soil Layer Thickness

The ground surface deformation profiles for different heights normalized for vertical bedrock displacements up to 2% the soil layer thickness. The ground surface deformation profiles normalized for vertical bedrock displacements up to 10% of the soil layer thickness only for normal fault cases of dip angles 30° and 45° and for reverse fault cases with loose sand.

The cases of larger soil layer thicknesses require larger vertical bedrock dispalcements for the shear band to propagate to the surface. As the depth increases, the confinement increases and the soil properties vary.

The length of the distorted one is larger for larger soil layer thicknesses for the cases that normalized. For the other cases, the length of the distorted one depends highly on the sheabr bands and on the corresponding ground surface deformation profile.

The shear band locations are farther from the center of the fault for larger soil layer thicknesses for the cases that include normal fault. For the cases that include reverse fault the locations of the primary shear bands are farther for smaller soil layer thicknesses.

5.3. Further Research

Further to the conclusions noted above, the following researches are suggested for future implementation:

The effect of excess pore water pressure on the fault propagation mechanism in offshore soil by applying a transient flow analysis. Excess negative pore pressure can increase the strength of the soil in case negative pore water pressures were generated..

Extending the following research to apply it to offshore clay sediments noting the the following thesis is limited to cases including offshore sand case. It is interesting to the investigate the affect of soil layer thickness and fault breccia on offshore clay sediments.

Modeling the fault propagation dynamically using explicit analysis and the HS small material to model the material behavior and stiffness degradation with the different damping factors. The effect of the dynamic loading on the water could affect the response as well.

The behavior of offshore pipeline subjected to dip slip fault and its resulting mode of failure. This requires 3D modeling of the pipeline and the soil and proper definition of the pipeline-soil interaction.

The following thesis considers a horizontal surface for the ground. Of the soil subjected to the dip-slip fault. It would be interesting to asses the fault propagation mechanism on a soil layer with an inclined ground surface and corresponding design parmaeters.

APPENDIX

Ground Surface Deformation Profiles

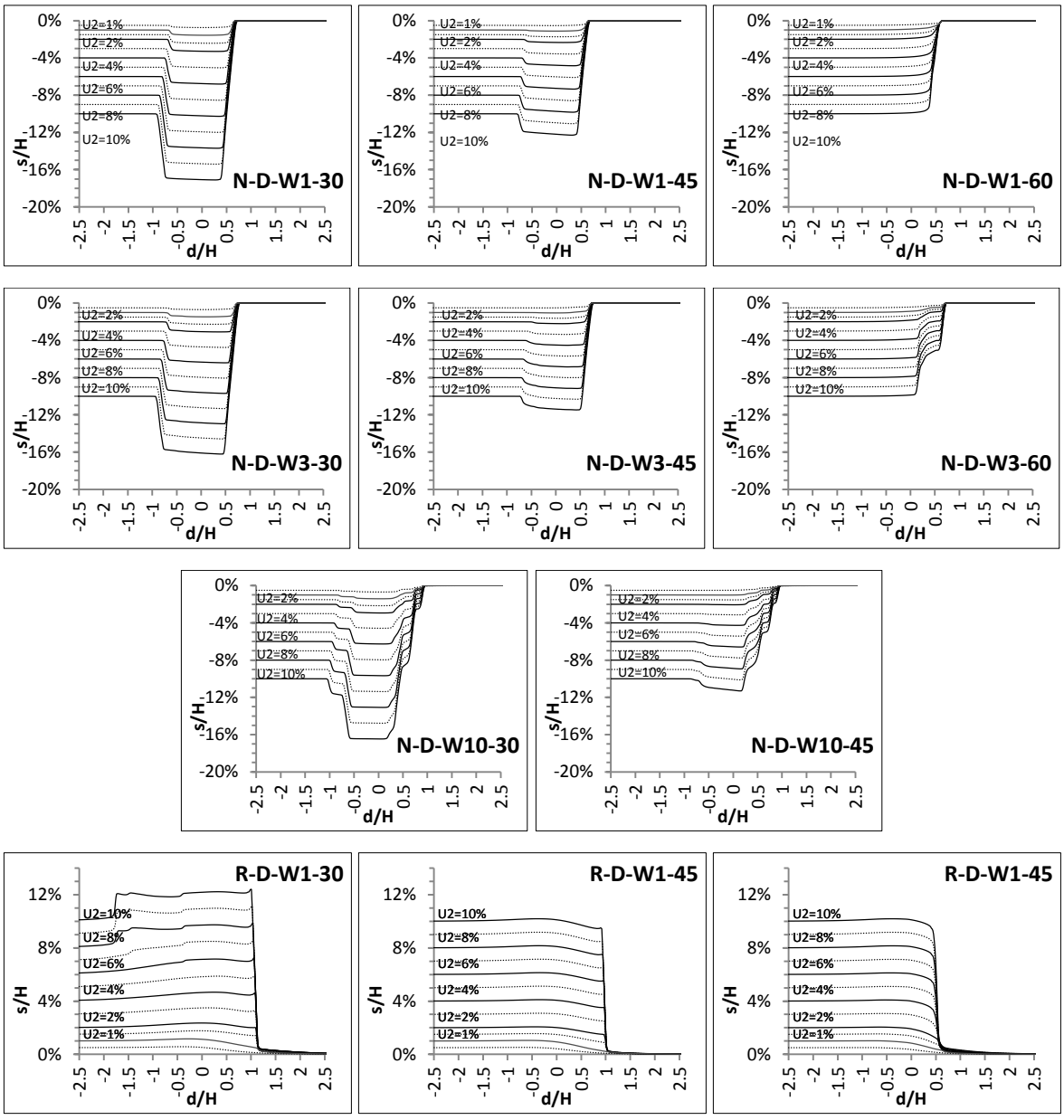

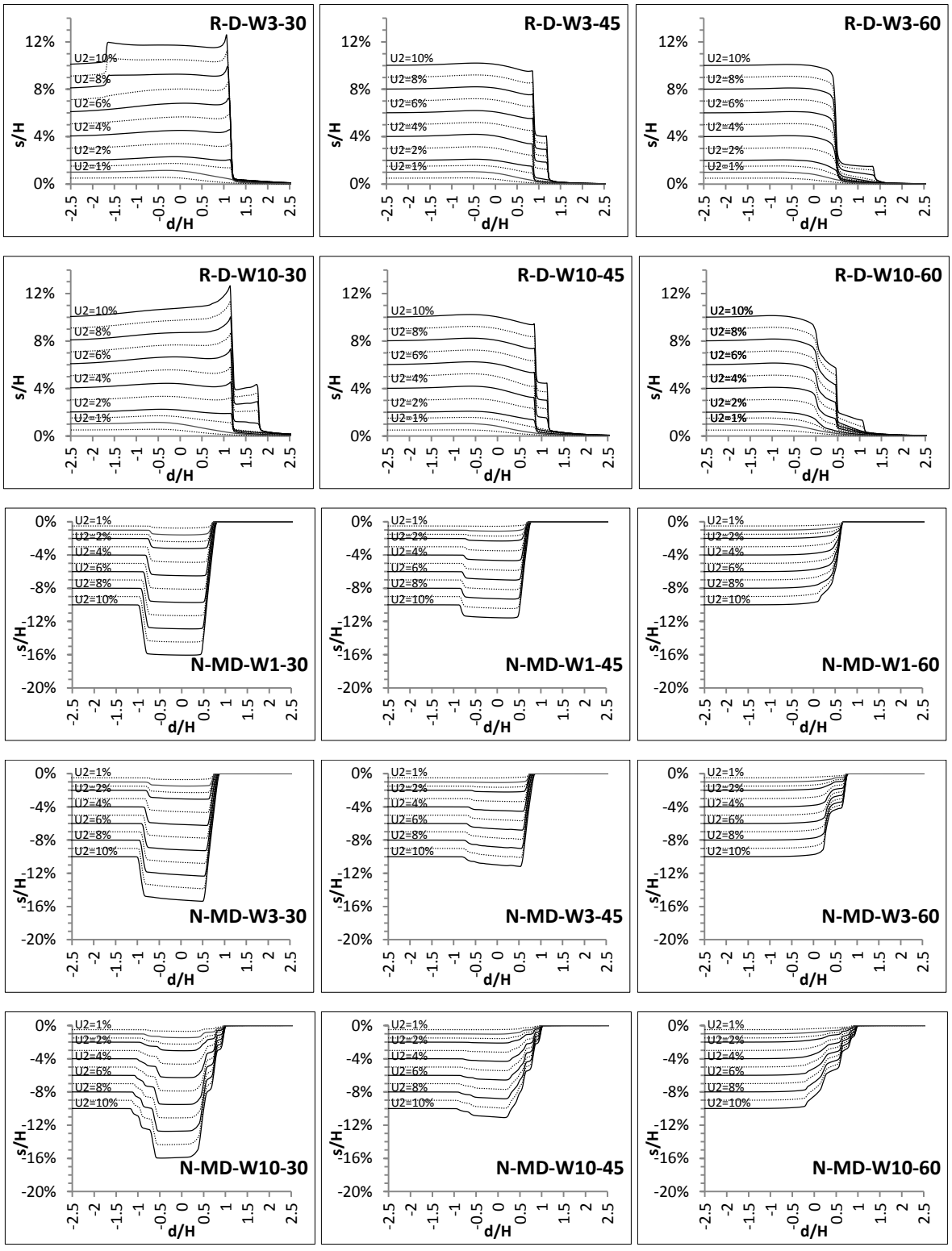
R-D-W3-30
R-D-W3-45
R-D-W3-60
R-D-W10-30
R-D-W10-45
R-D-W10-60
N-MD-W1-30
N-MD-W1-45
N-MD-W1-60
N-MD-W3-30
N-MD-W3-45
N-MD-W3-60
N-MD-W10-30
N-MD-W10-45
N-MD-W10-60
U2=1%
U2=2%
U2=4%
U2=6%
U2=8%
U2=10%
s/H
-s/H
d/H

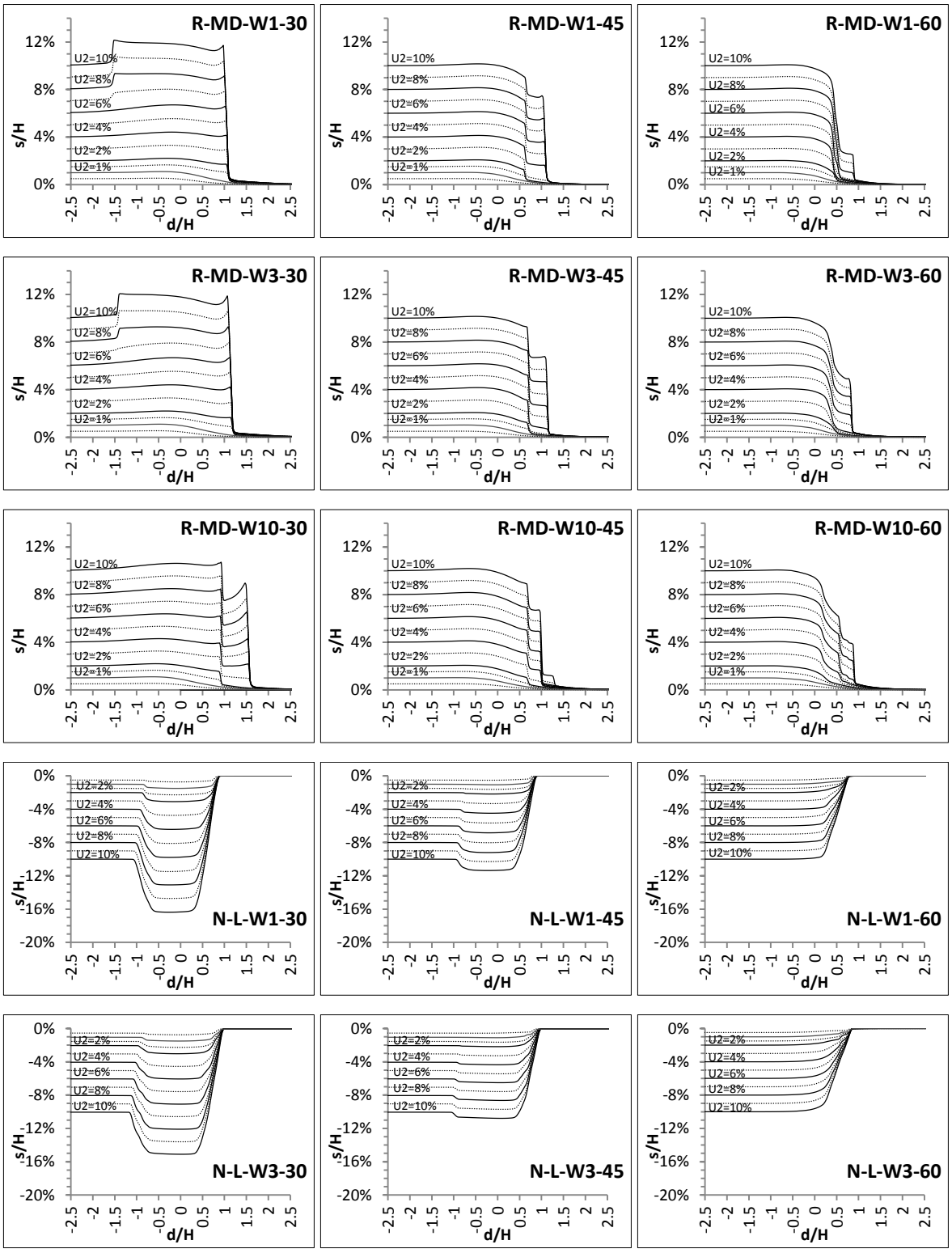
R-MD-W1-30
R-MD-W1-45
R-MD-W1-60
R-MD-W3-30
R-MD-W3-45
R-MD-W3-60
R-MD-W10-30
R-MD-W10-45
R-MD-W10-60
N-L-W1-30
N-L-W1-45
N-L-W1-60
N-L-W3-30
N-L-W3-45
N-L-W3-60
s/H
d/H
U2=1%
U2=2%
U2=4%
U2=6%
U2=8%
U2=10%

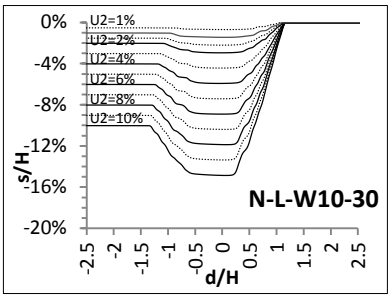
N-L-W10-30
U2=1%
U2=2%
U2=4%
U2=6%
U2=8%
U2=10%
s/H
d/H

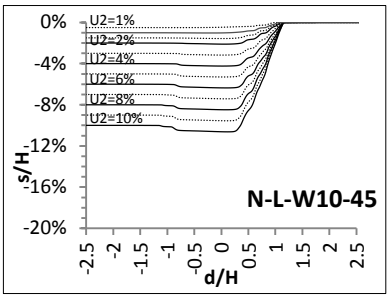
N-L-W10-45
U2=1%
U2=2%
U2=4%
U2=6%
U2=8%
U2=10%
s/H
d/H

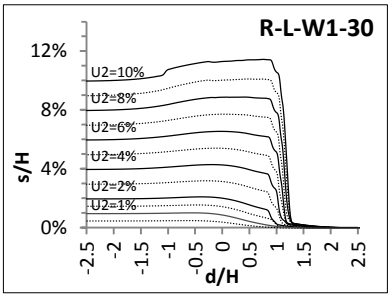
R-L-W1-30
U2=10%
U2=8%
U2=6%
U2=4%
U2=2%
U2=1%
s/H
d/H

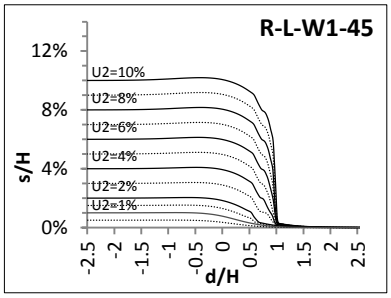
R-L-W1-45
U2=10%
U2=8%
U2=6%
U2=4%
U2=2%
U2=1%
s/H
d/H

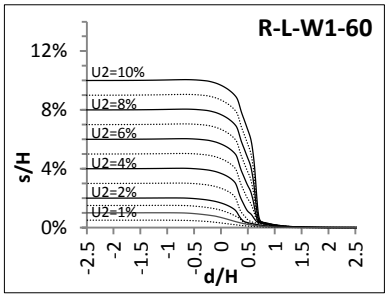
R-L-W1-60
U2=10%
U2=8%
U2=6%
U2=4%
U2=2%
U2=1%
s/H
d/H

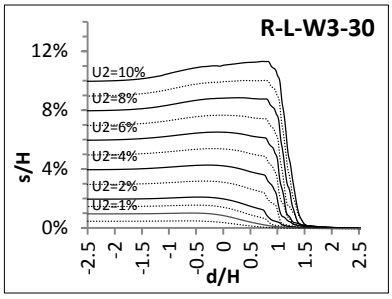
R-L-W3-30
U2=10%
U2=8%
U2=6%
U2=4%
U2=2%
U2=1%
s/H
d/H

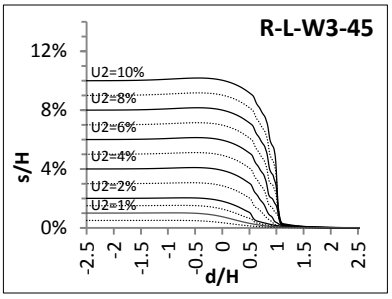
R-L-W3-45
U2=10%
U2=8%
U2=6%
U2=4%
U2=2%
U2=1%
s/H
d/H

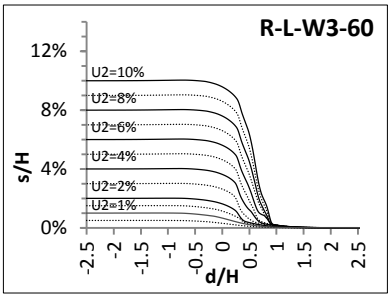
R-L-W3-60
U2=10%
U2=8%
U2=6%
U2=4%
U2=2%
U2=1%
s/H
d/H

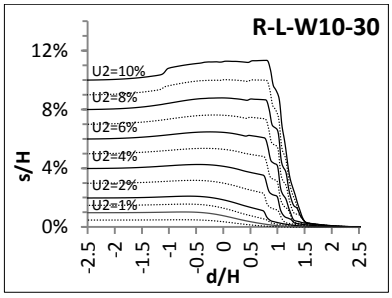
R-L-W10-30
U2=10%
U2=8%
U2=6%
U2=4%
U2=2%
U2=1%
s/H
d/H

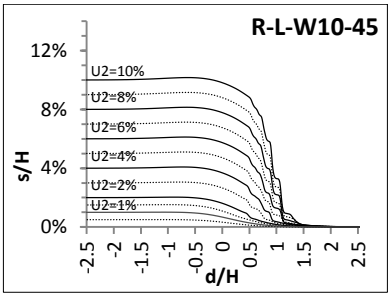
R-L-W10-45
U2=10%
U2=8%
U2=6%
U2=4%
U2=2%
U2=1%
s/H
d/H

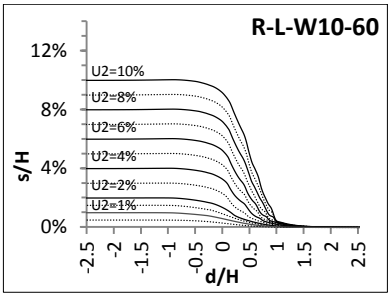
R-L-W10-60
U2=10%
U2=8%
U2=6%
U2=4%
U2=2%
U2=1%
s/H
d/H

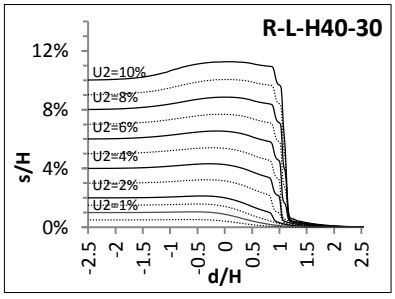
R-L-H40-30
U2=10%
U2=8%
U2=6%
U2=4%
U2=2%
U2=1%
s/H
d/H

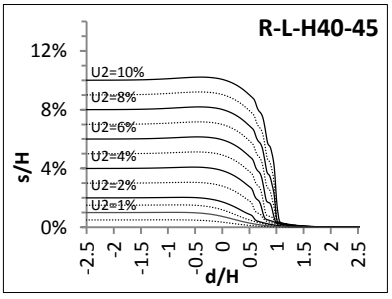
R-L-H40-45
U2=10%
U2=8%
U2=6%
U2=4%
U2=2%
U2=1%
s/H
d/H

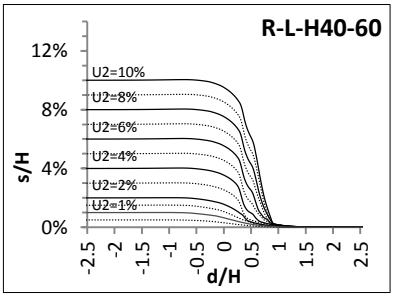
R-L-H40-60
U2=10%
U2=8%
U2=6%
U2=4%
U2=2%
U2=1%
s/H
d/H

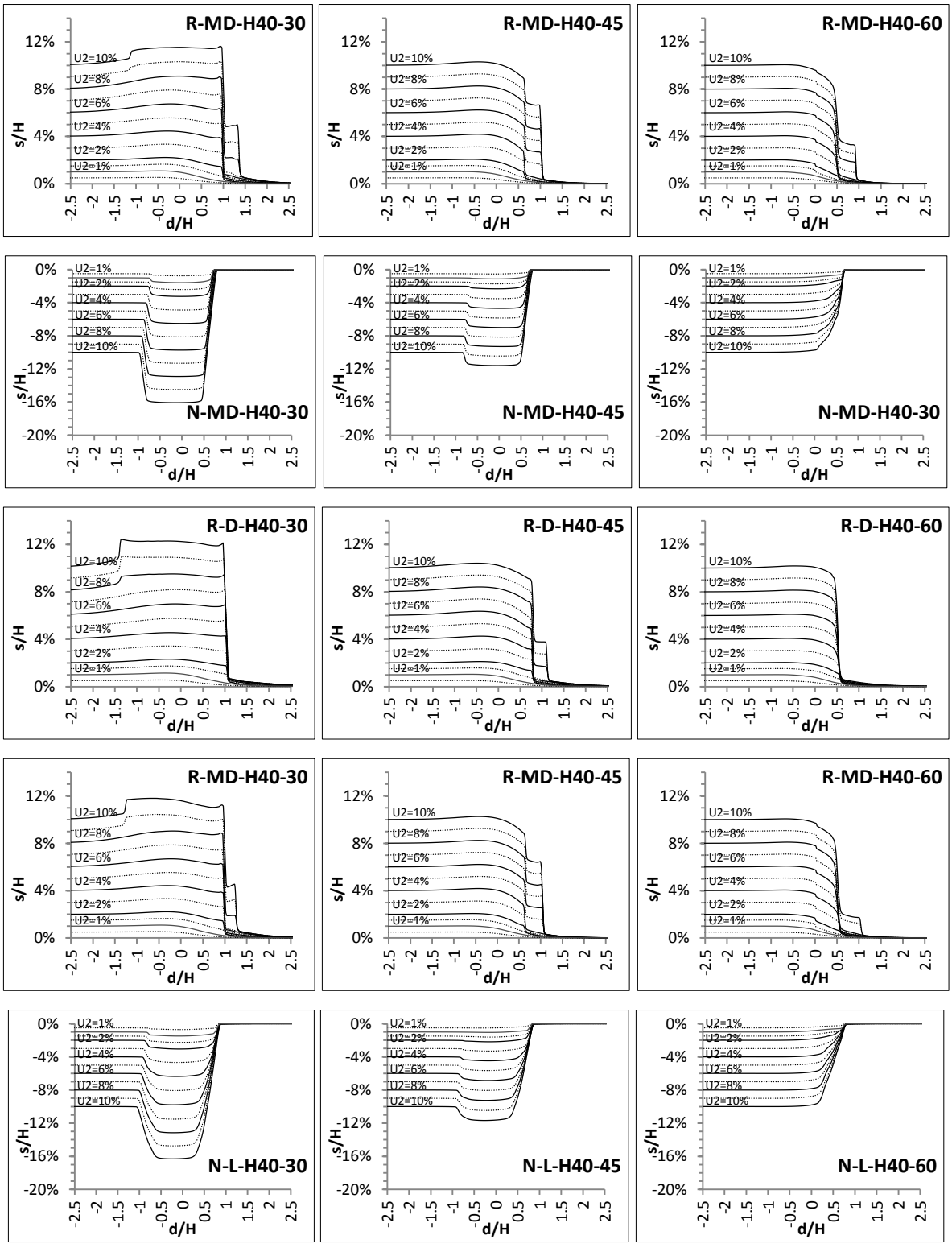
R-MD-H40-30
R-MD-H40-45
R-MD-H40-60
N-MD-H40-30
N-MD-H40-45
N-MD-H40-30
R-D-H40-30
R-D-H40-45
R-D-H40-60
R-MD-H40-30
R-MD-H40-45
R-MD-H40-60
N-L-H40-30
N-L-H40-45
N-L-H40-60
s/H
d/H
U2=1%
U2=2%
U2=4%
U2=6%
U2=8%
U2=10%

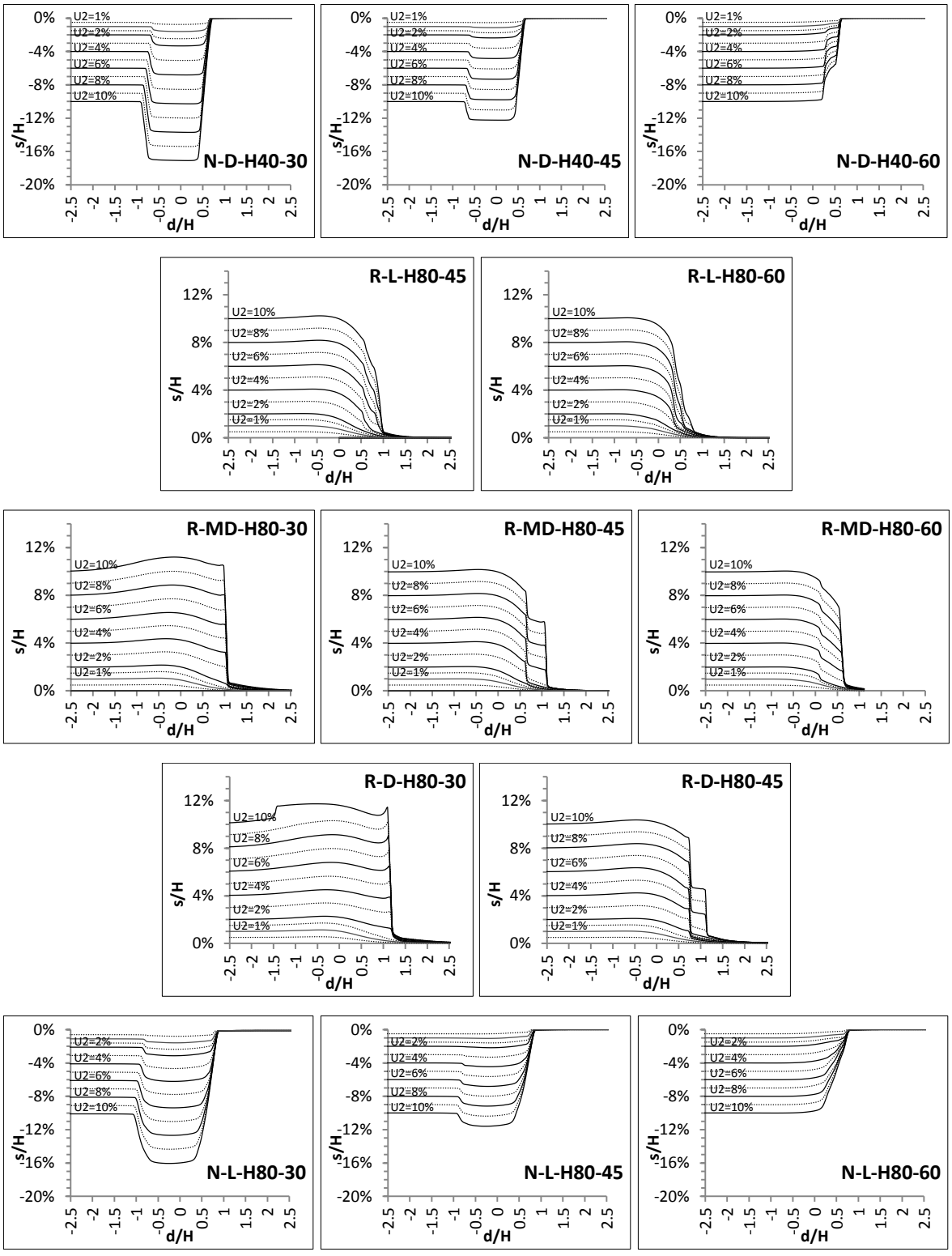
N-D-H40-30
N-D-H40-45
N-D-H40-60
R-L-H80-45
R-L-H80-60
R-MD-H80-30
R-MD-H80-45
R-MD-H80-60
R-D-H80-30
R-D-H80-45
N-L-H80-30
N-L-H80-45
N-L-H80-60
s/H
d/H
U2=1%
U2=2%
U2=4%
U2=6%
U2=8%
U2=10%

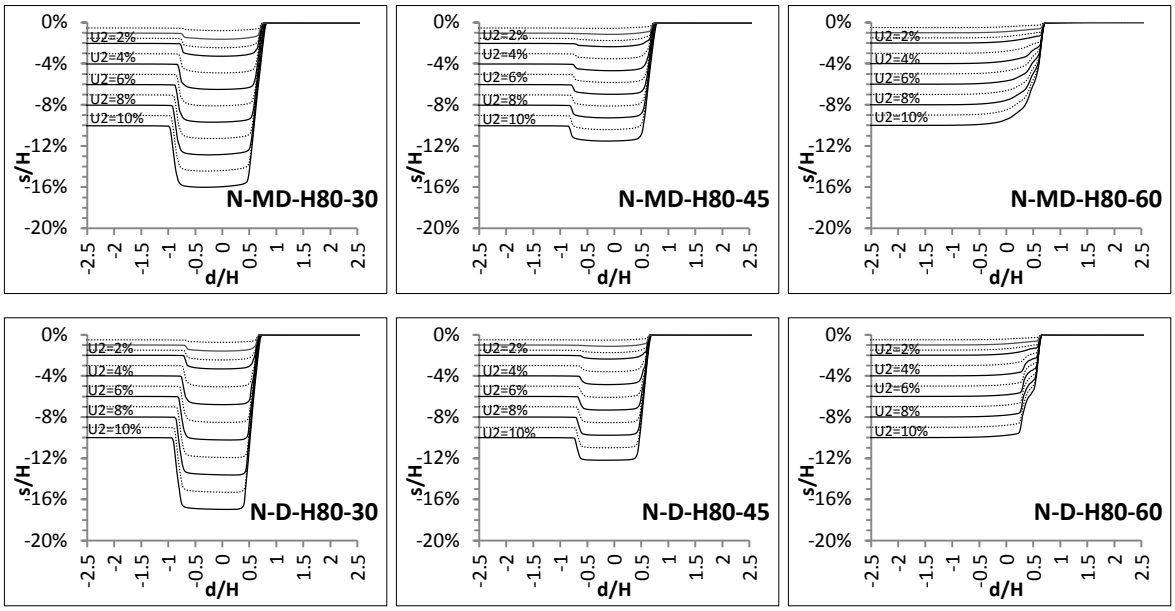

Length of the Distorted Zone:

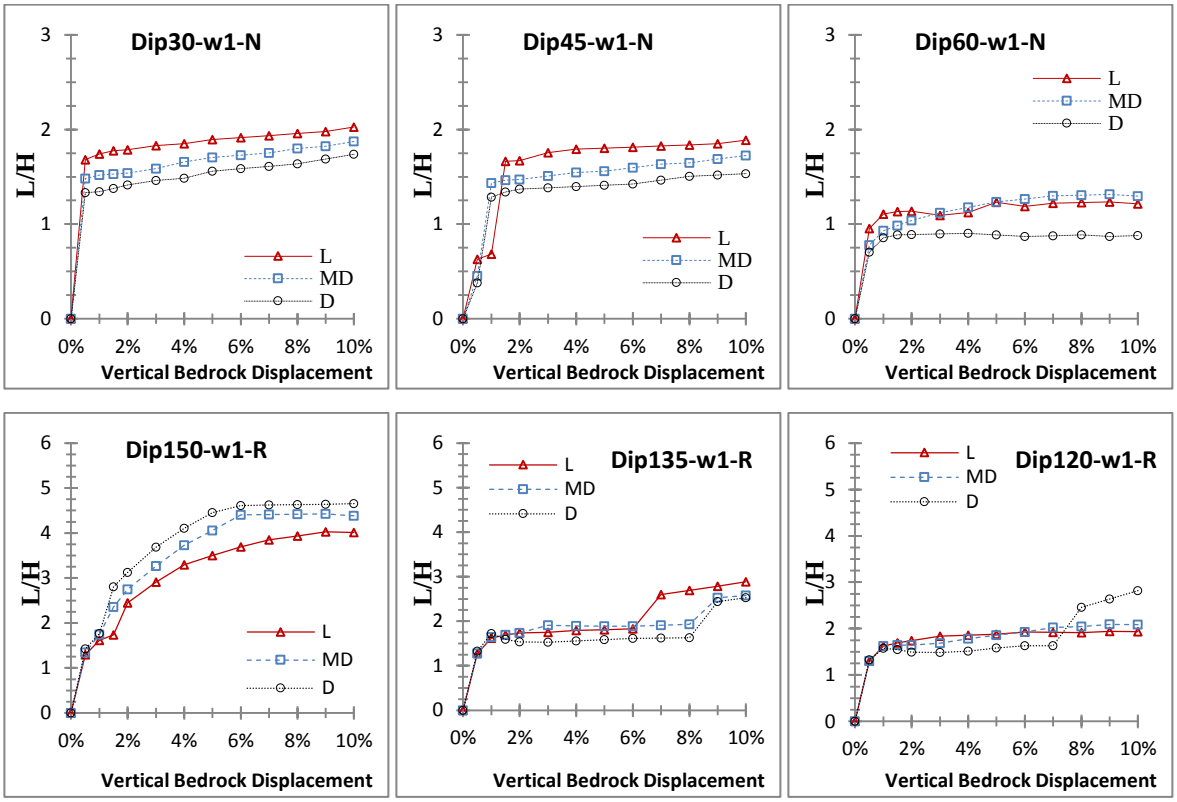

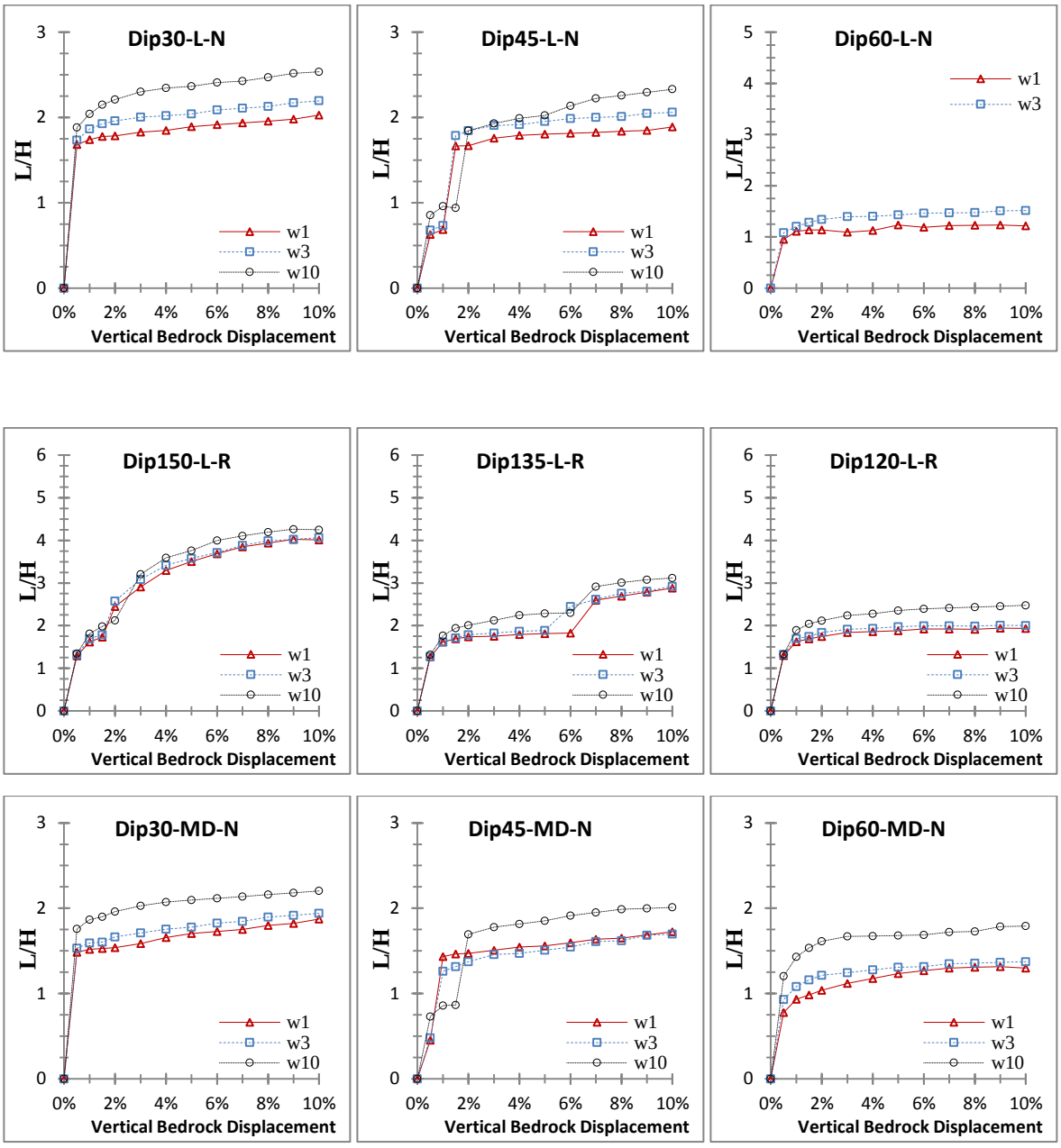
Dip30-L-N
Dip45-L-N
Dip60-L-N
Dip150-L-R
Dip135-L-R
Dip120-L-R
Dip30-MD-N
Dip45-MD-N
Dip60-MD-N
L/H
Vertical Bedrock Displacement
0%
2%
4%
6%
8%
10%
w1
w3
w10

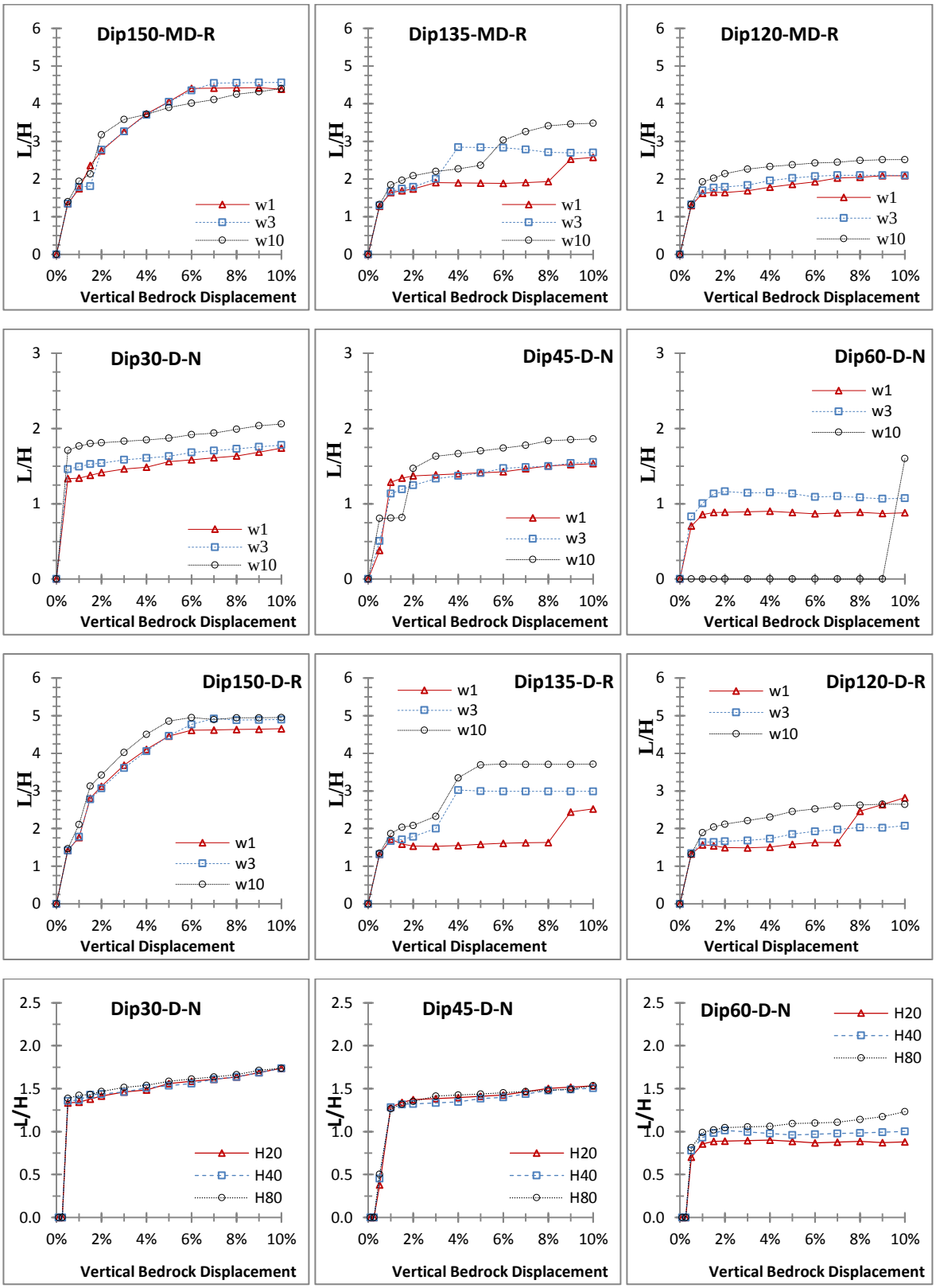
Dip150-MD-R
Dip135-MD-R
Dip120-MD-R
Dip30-D-N
Dip45-D-N
Dip60-D-N
Dip150-D-R
Dip135-D-R
Dip120-D-R
Dip30-D-N
Dip45-D-N
Dip60-D-N
L/H
w1
w3
w10
H20
H40
H80
0%
2%
4%
6%
8%
10%
Vertical Bedrock Displacement
Vertical Displacement

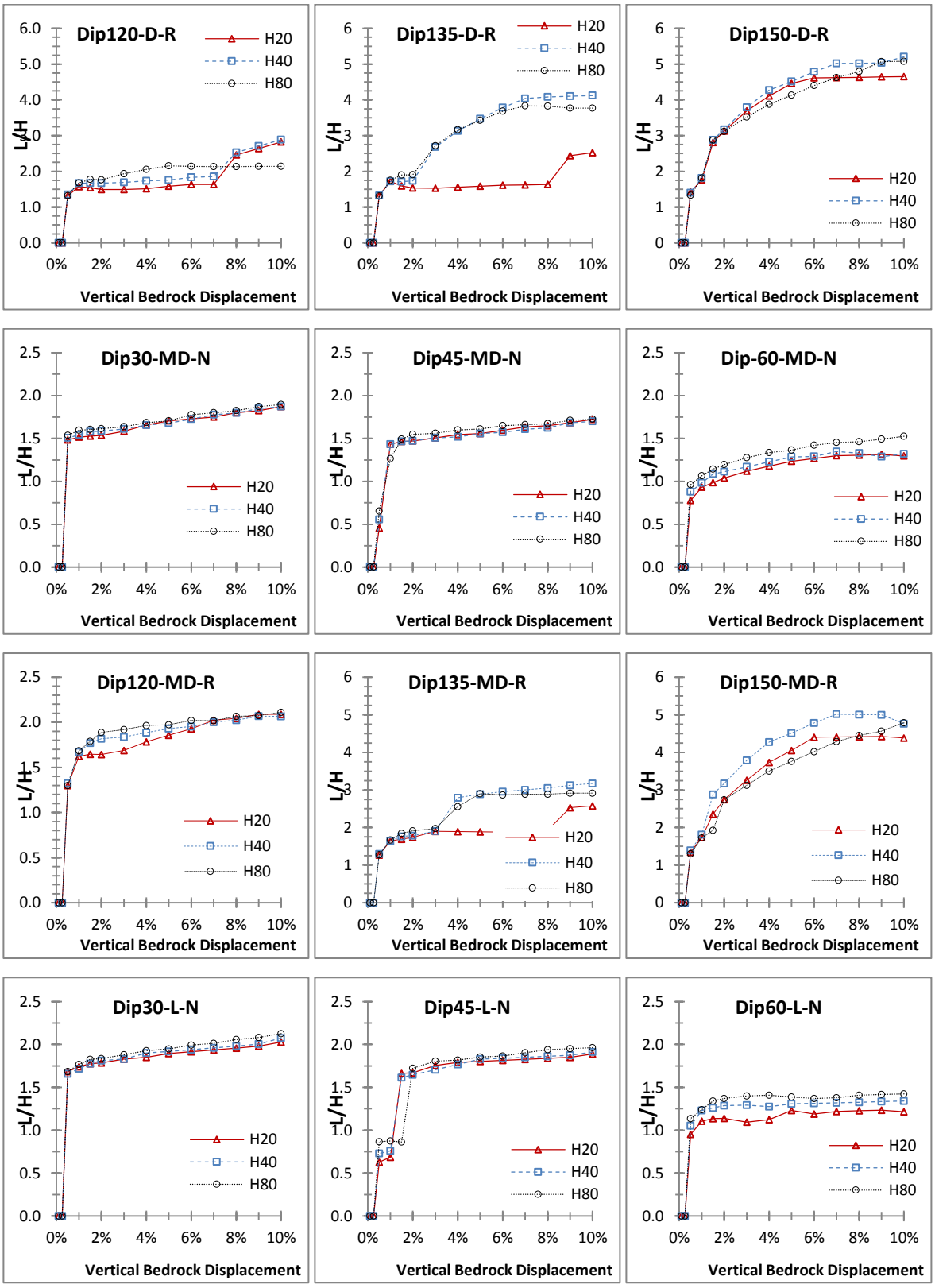
Dip120-D-R
Dip135-D-R
Dip150-D-R
Dip30-MD-N
Dip45-MD-N
Dip-60-MD-N
Dip120-MD-R
Dip135-MD-R
Dip150-MD-R
Dip30-L-N
Dip45-L-N
Dip60-L-N
H20
H40
H80
L/H
Vertical Bedrock Displacement
0%
2%
4%
6%
8%
10%

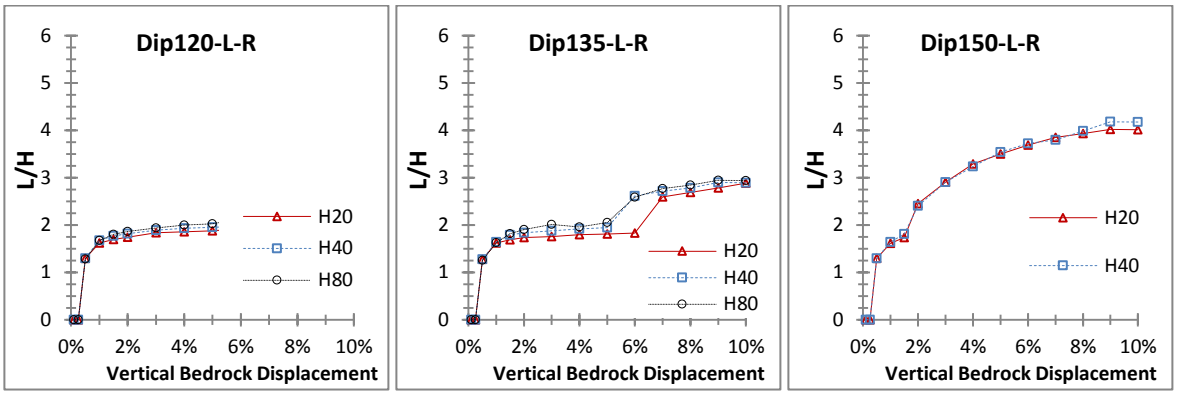

Center of The distorted Zone:

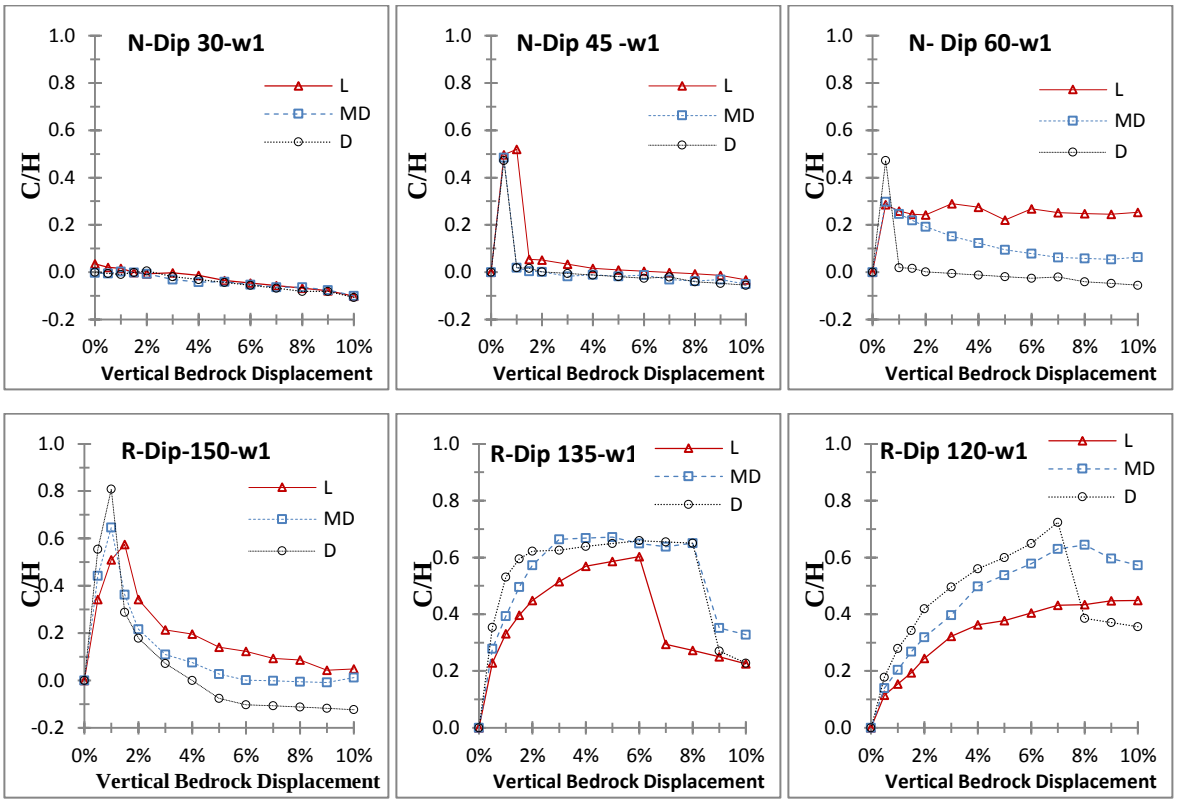

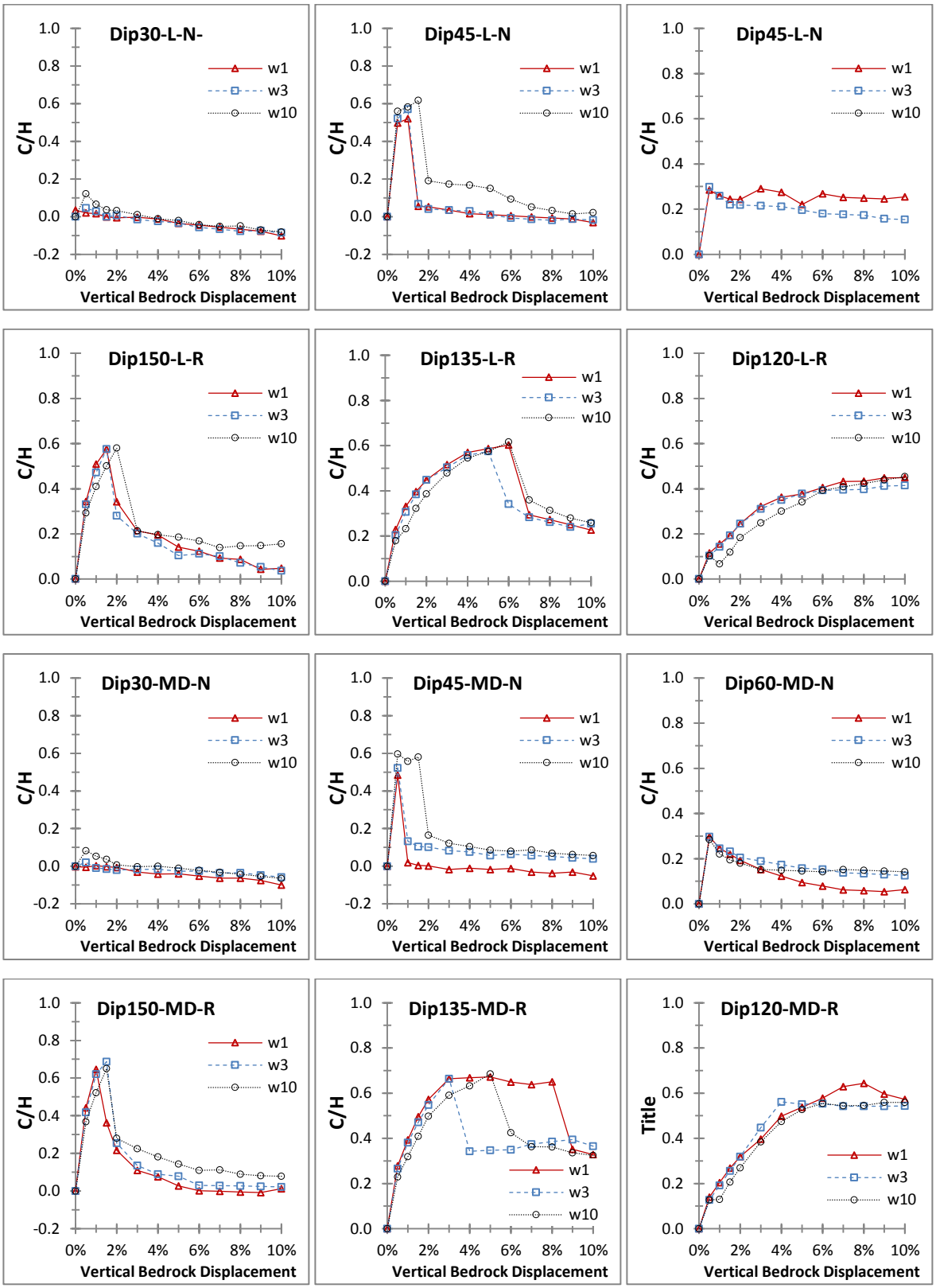
Dip30-L-N-
Dip45-L-N
Dip45-L-N
Dip150-L-R
Dip135-L-R
Dip120-L-R
Dip30-MD-N
Dip45-MD-N
Dip60-MD-N
Dip150-MD-R
Dip135-MD-R
Dip120-MD-R
C/H
Title
w1
w3
w10
1.0
0.8
0.6
0.4
0.2
0.0
-0.2
0%
2%
4%
6%
8%
10%
Vertical Bedrock Displacement
Verical Bedrock Displacement

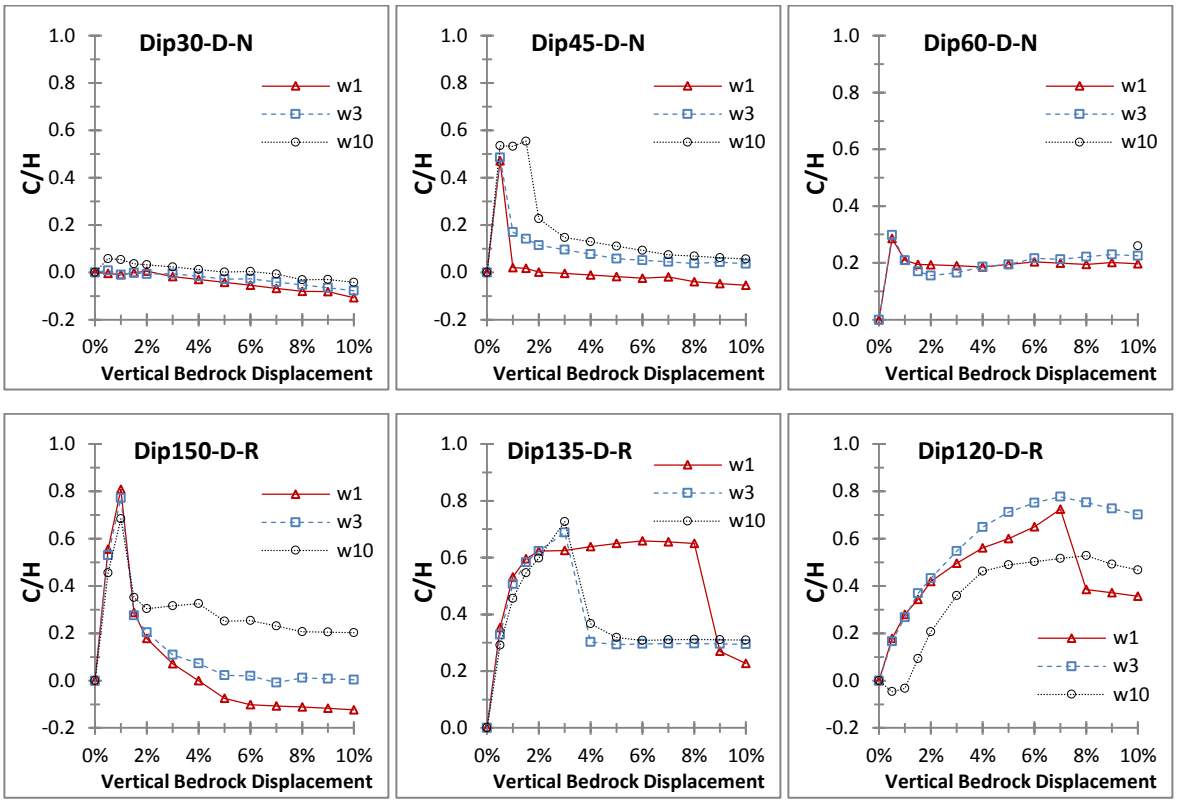
Dip30-D-N
Dip45-D-N
Dip60-D-N
Dip150-D-R
Dip135-D-R
Dip120-D-R
C/H
Vertical Bedrock Displacement
w1
w3
w10
1.0
0.8
0.6
0.4
0.2
0.0
-0.2
0%
2%
4%
6%
8%
10%

Dcrit/H:

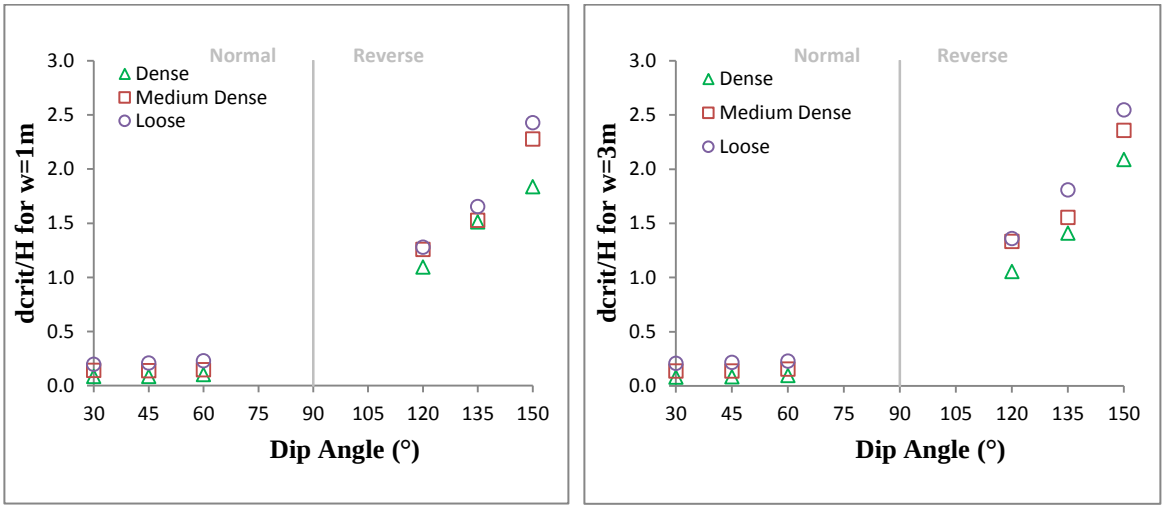
Normal
Reverse
Dense
Medium Dense
Loose
dcrit/H for w=1m
dcrit/H for w=3m
Dip Angle (°)
3.0
2.5
2.0
1.5
1.0
0.5
0.0
30
45
60
75
90
105
120
135
150

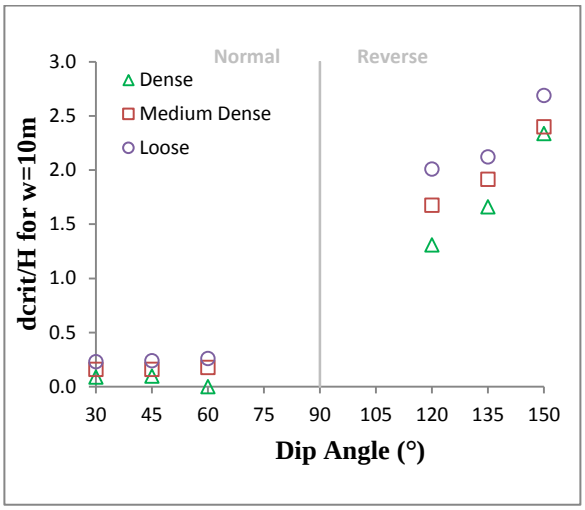
Normal
Reverse
Dense
Medium Dense
Loose
dcrit/H for w=10m
3.0
2.5
2.0
1.5
1.0
0.5
0.0
30 45 60 75 90 105 120 135 150
Dip Angle (°)

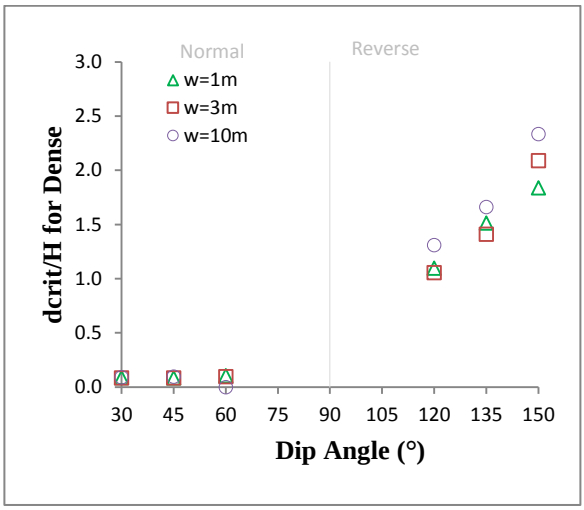
Normal
Reverse
w=1m
w=3m
w=10m
dcrit/H for Dense
3.0
2.5
2.0
1.5
1.0
0.5
0.0
30 45 60 75 90 105 120 135 150
Dip Angle (°)

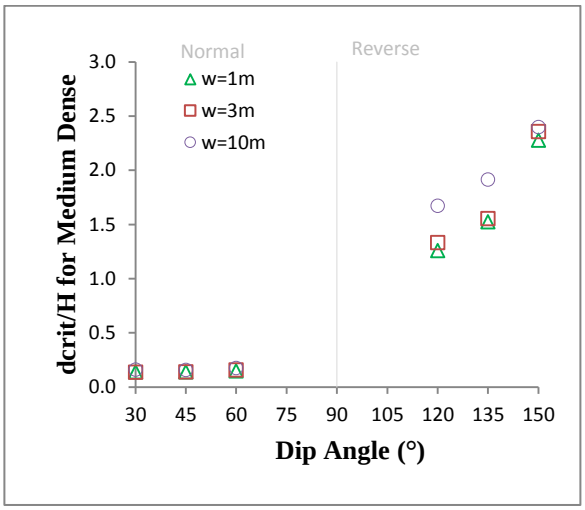
Normal
Reverse
w=1m
w=3m
w=10m
dcrit/H for Medium Dense
3.0
2.5
2.0
1.5
1.0
0.5
0.0
30 45 60 75 90 105 120 135 150
Dip Angle (°)

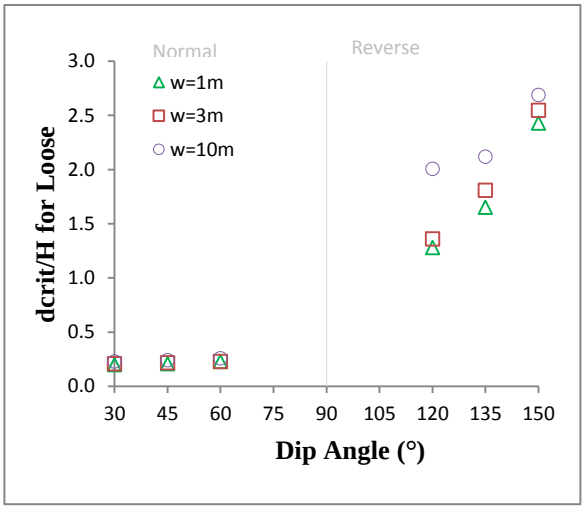
Normal
Reverse
w=1m
w=3m
w=10m
dcrit/H for Loose
3.0
2.5
2.0
1.5
1.0
0.5
0.0
30 45 60 75 90 105 120 135 150
Dip Angle (°)

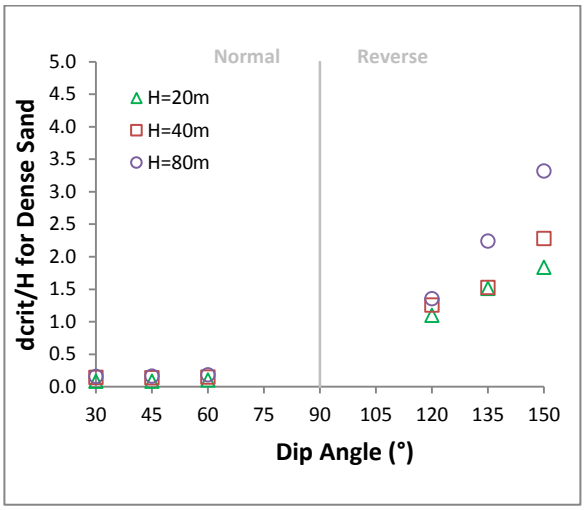
Normal
Reverse
H=20m
H=40m
H=80m
dcrit/H for Dense Sand
Dip Angle (°)
5.0
4.5
4.0
3.5
3.0
2.5
2.0
1.5
1.0
0.5
0.0
30
45
60
75
90
105
120
135
150

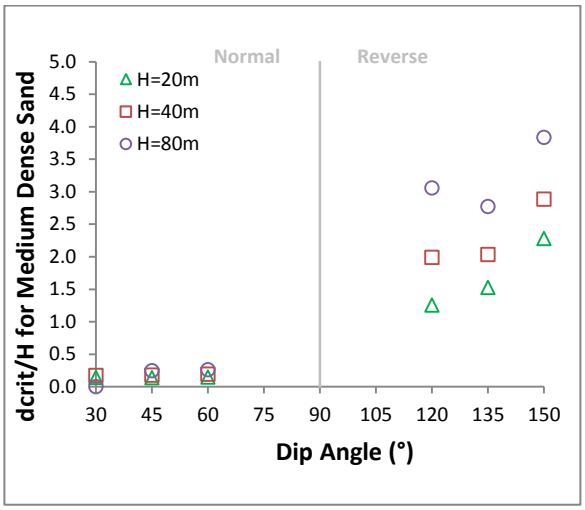
Normal
Reverse
H=20m
H=40m
H=80m
dcrit/H for Medium Dense Sand
Dip Angle (°)
5.0
4.5
4.0
3.5
3.0
2.5
2.0
1.5
1.0
0.5
0.0
30
45
60
75
90
105
120
135
150

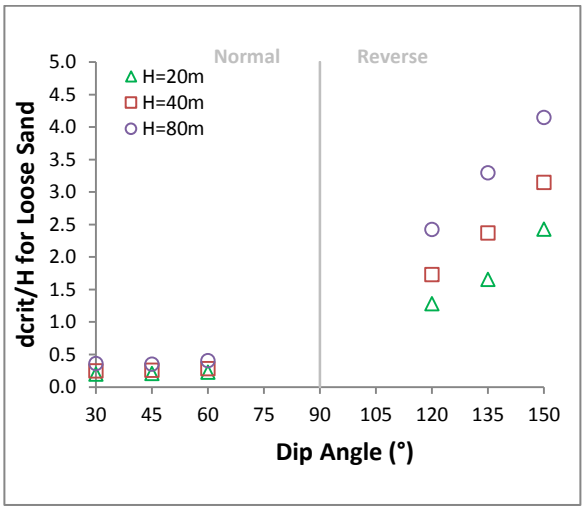
Normal
Reverse
H=20m
H=40m
H=80m
dcrit/H for Loose Sand
Dip Angle (°)
5.0
4.5
4.0
3.5
3.0
2.5
2.0
1.5
1.0
0.5
0.0
30
45
60
75
90
105
120
135
150

Shear Bands:

R-D-W1-30 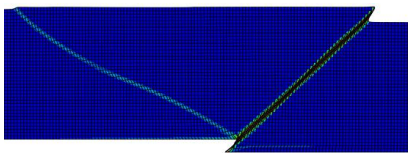	R-D-W1-45 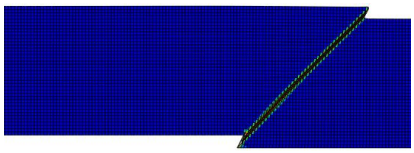	R-D-W1-60 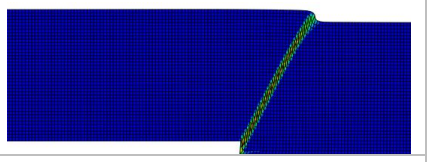
R-MD-W1-30 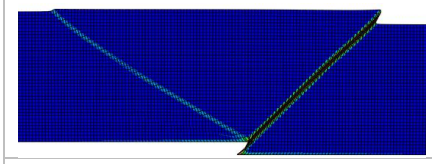	R-MD-W1-45 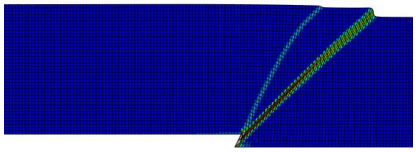	R-MD-W1-60 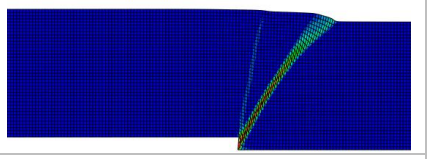
R-L-W1-30 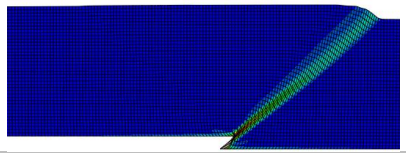	R-L-W1-45 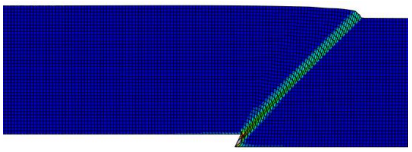	R-L-W1-60 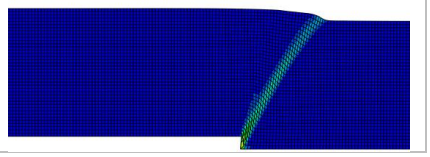

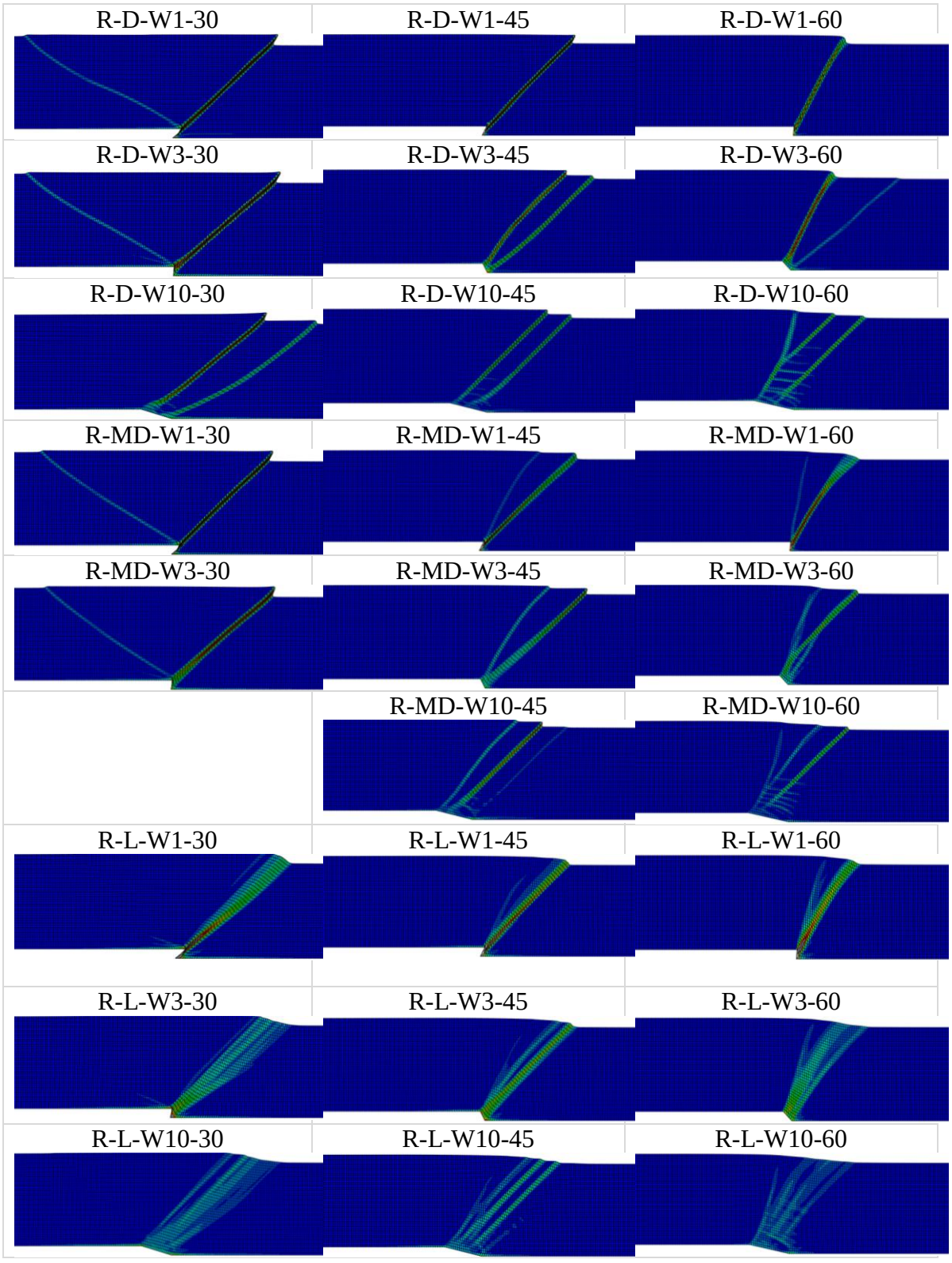
R-D-W1-30
R-D-W1-45
R-D-W1-60
R-D-W3-30
R-D-W3-45
R-D-W3-60
R-D-W10-30
R-D-W10-45
R-D-W10-60
R-MD-W1-30
R-MD-W1-45
R-MD-W1-60
R-MD-W3-30
R-MD-W3-45
R-MD-W3-60
R-MD-W10-45
R-MD-W10-60
R-L-W1-30
R-L-W1-45
R-L-W1-60
R-L-W3-30
R-L-W3-45
R-L-W3-60
R-L-W10-30
R-L-W10-45
R-L-W10-60

N-D-w1-30 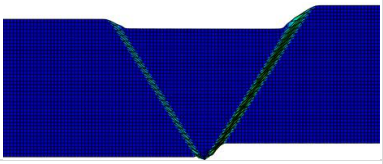	N-D-w1-45 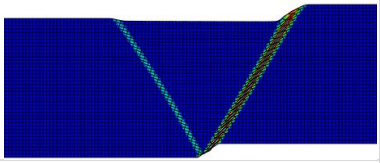	N-D-60-w1 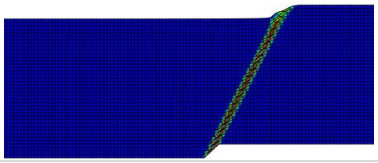
N-D-w3-30 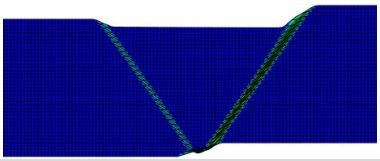	N-D-w3-45 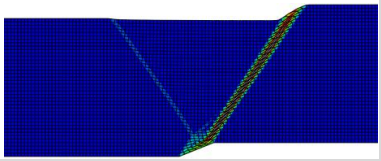	N-D-60-W3 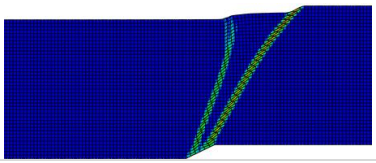
N-D-w10-30 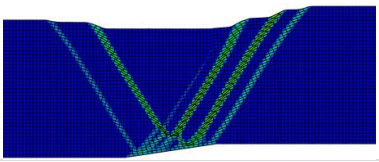	N-D-w10-45 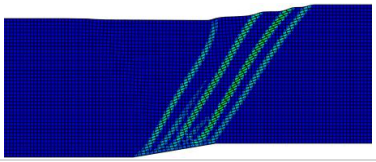	
N-MD-30-W1 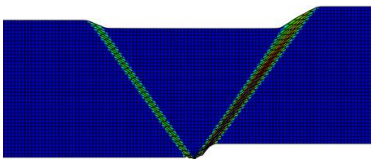	N-MD-W1-45 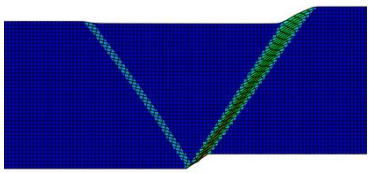	N-MD-W1-60 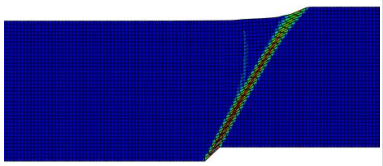
N-MD-30-W3 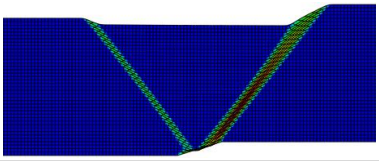		N-MD-W3-60 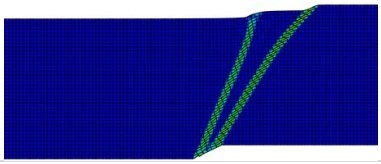
N-MD-30-W10 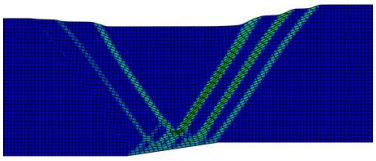		N-MD-W10-60 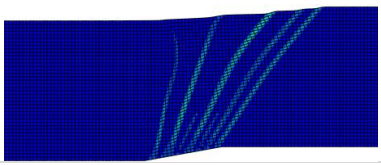
N-L-30-W1 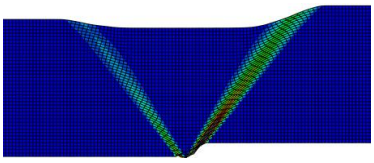	N-L-45-W1 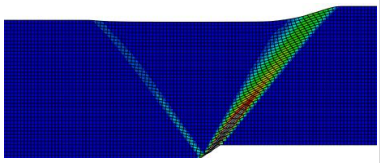	N-L-W1-60 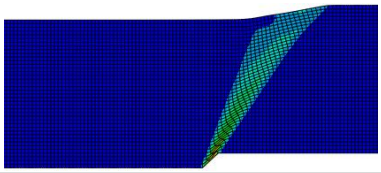
N-L-30-W3	N-L-45-W3	N-L-60-W3

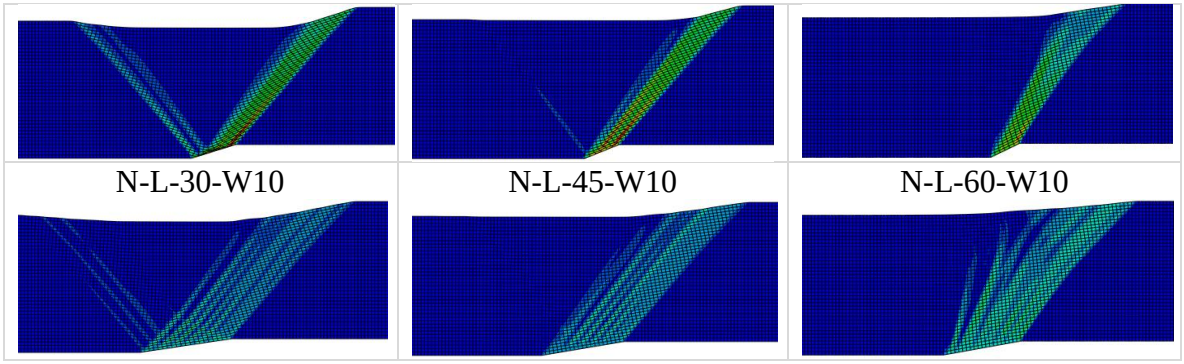

N-L-30-W10 N-L-45-W10 N-L-60-W10

REFERENCES:

ABAQUS, Inc. (2013) ABAQUS V.6.13 user's manual, Providence, R.I.

Abdoun, T. H., Ha, D., O'Rourke, M. J., Symans, M. D., O'Rourke, T. D., Palmer, M. C., & Stewart, H. E. (2009). Factors influencing the behavior of buried pipelines subjected to earthquake faulting. Soil Dynamics and Earthquake Engineering, 29(3), 415-427.

Anastasopoulos, I., Gazetas, G., Bransby, M. F., Davies, M. C. R., & El Nahas, A. (2007). Fault rupture propagation through sand: finite-element analysis and validation through centrifuge experiments. Journal of Geotechnical and Geoenvironmental Engineering, 133(8), 943-958.

Arifin , R. B., Zhao, P., & Bai, Y. (2010, January). Seismic analysis for the subsea pipeline system. In ASME 2010 29th International Conference on Ocean, Offshore and Arctic Engineering (pp. 659-667). American Society of Mechanical Engineers.

Ariman, T., Lee, B. J., & QUANQING, C. (1987). Failure of buried pipelines under large ground deformations. Developments in geotechnical engineering,49, 63-75.

Ariman, T., & Lee, B. J. (1991). Tension Bending Behavior of Buried Pipelines Under Large Ground Deformations in Active Faults. In Lifeline Earthquake Engineering (1991) (pp. 226-233). ASCE.

ASCE (1984), Guidelines for the Seismic Design of Oil and Gas Pipeline Systems, Committee on Gas and Liquid Fuel Lifeline, ASCE, 1984.

American Lifeline Alliance-ASCE (2001, July), Guidelines for the design of buried steel pipe, (addenda through Feb, 2005).

Anastasopoulos, I., Gazetas, G., Bransby, M. F., Davies, M. C. R., and El Nahas, A. (2007). "Fault rupture propagation through sand: finite-element analysis and validation through centrifuge experiments." J. Geotech. Geoenviron. Eng., 133(8), 943-958.

Anastasopoulos, I. , and Gazetas, G. (2007a). "Foundation-structure systems over a rupturing normal fault. I: Observations after the Kocaeli 1999 Earthquake." *Bull. Earthquake Eng.* , **5** (**3**), 253–275.

Anastasopoulos, I. , and Gazetas, G. (2007b). "Foundation-structure systems over a rupturing normal fault. II: Analysis of the Kocaeli case histories." *Bull. Earthquake Eng.* , **5** (**3**), 277–301

Belousov, V. V. (1961). "Experimental geology". Sci. Am., 204(2), 96-107.

Brankman, C. M., and Aydin, A. (2004). "Uplift and contractional deformation along a segmented strike-slip fault system: the Gargano Promontory, southern Italy". *J. Struct. Geol.*, *26*(5), 807-824.

Bransby, M. F., Nahas, E., Turner, E., & Davies, M. C. R. (2007). The interaction of reverse faults with flexible continuous pipelines. International Journal of Physical Modelling in Geotechnics, 7(3), 25-40.

Bransby, M. F., Davies, M. C. R., and El Nahas, A. (2008a). "Centrifuge modelling of normal fault-footing interaction." *Bull. Earthquake Eng.*, **6** (**4**), 585–605.

Bransby, M. F., Davies, M. C. R., El Nahas, A. , and Nagaoka, S. (2008b). “Centrifuge modelling of reverse fault-foundation interaction.” *Bull. Earthquake Eng.* , **6** (**4**), 607–628.

Bray, J.D., Seed, R.B., and Seed ,H.B.(1989). "The effects of tectonic movements on stresses and deformations in earth embankments." Report no. UCB/EERC-90/13: Earthquake Engineering Research Center, University of California, Berkeley.

Bray, J. D., Seed, R. B., and Seed, H. B. (1993). "lg small-scale modelling of saturated cohesive soils." Geotech. Testing J., 16(1), 46-53.

Bray, J. D., Seed, R. B., Cluff, L. S., and Seed, H. B. (1994a). “Earthquake fault rupture propagation through soil.” J. Geotech. Engrg.,120(3), 543–561.

Bray, J. D., Seed, R. B., and Seed, H. B. (1994b). “Analysis of earthquake fault rupture propagation through cohesive soil.” J. Geotech. Engrg., 120(3), 562–580.

Carr, P., & Preston, R. (1999, March). Risk Assessment of Deepwater Gas Trunk lines. In 2nd International Deepwater Pipeline Technology Conference.

Chaudhary, V., Kumar P, V. D., & Kumar, R. P. (2013). Finite element analysis of buried continuous pipeline subjected to fault motion. International Journal of Structural Engineering, 4(4), 314-331.

Cole, D. A., Jr., and Lade, P. V. (1984). "Influence zones in alluvium over dip-slip faults." J. Geotech. Engrg., ASCE, 110(5), 599-615.

Dong, J. J., Wang, C. D., Lee, C. T., Liao, J. J., & Pan, Y. W. (2004). “The influence of surface ruptures on building damage in the 1999 Chi-Chi earthquake: a case study in Fengyuan City”. *Eng. Geol.*, *71*(1-2), 157-179.

Duan., M., Mao., D., Yue. Z., Estefen, S., & Li, Z. (2011). A seismic design method for subsea pipelines against earthquake fault movement. China Ocean Engineering, 25(2), 179–188.

Duncan, J. M., and Lefebvre, G. (1973). "Earth pressures on structures due to fault movement". J Soil Mech. Found. Div., 99(12), 1153-1163.

Emmons, R. C. (1969). "Strike-slip rupture patterns in sand models." Tectonophysics,7(1), 71-87.

Erickson, S. G., Staryer, L. M., and Suppe, J. (2001). “Initiation and reactivation of faults during movement over a thrust-fault ramp: Numerical mechanical models.” J. Struct. Geol., 23, 11–23.

Faccioli, E., Anastasopoulos, I., Gazetas, G., Callerio, A., and Paolucci, R. (2008). Fault rupture–foundation interaction: selected case histories. Bull. Earthq. Eng, 6(4), 557-583.

Guo, E., Shao, G., & Liu, H. (2004, August). Numerical study of damage to buried oil pipeline under large fault displacement. In Proc. Of the 13th World Conference on Earthquake Engineering, Vancouver, Canada, Aug (Vol. 1, p. e6).

Ha, D., Abdoun, T. H., O’Rourke, M. J., Symans, M. D., O’Rourke, T. D., Palmer, M. C., & Stewart, H. E. (2008). Centrifuge modeling of earthquake effects on buried high-density polyethylene (HDPE) pipelines crossing fault zones. Journal of Geotechnical and Geoenvironmental Engineering, 134(10), 1501-1515.

Ha, D., Abdoun, T. H., O'Rourke, M. J., Symans, M. D., O'Rourke, T. D., Palmer, M. C., & Stewart, H. E. (2008). Buried high-density polyethylene pipelines subjected to normal and strike-slip faulting-a centrifuge investigation. Canadian Geotechnical Journal, 45(12), 1733-1742

Hashem, N., Kamhawi, K. and Walker, A. C. (2004), Gulf of Aqaba Pipeline Crossing, Offshore Pipeline Technology Conference.

Horsfield, W. T. (1977). "An experimental approach to basement-controlled faulting." Geologie En Mijnbouw, Haarlem, The Netherlands, 56(4), 363-370.

Jiao, Z. L., Shuai, J., & Han, K. J. (2009). Response analysis of buried pipeline subjected to fault movements. In International Conference on Pipelines and Trenchless Technology (pp. 1212-1218).

Johansson, J., and Konagai, K. (2004). Fault surface rupture experiments: a comparison of dry and saturated soils. In Proceeding of 27th Symposium on Earthquake Engineering, JSCE, Paper (No. 271).

Johansson, J., and Konagai, K. (2006). "Fault induced permanent ground deformations—an experimental comparison of wet and dry soil and implications for buried structures". J. Soil Dyn. Earthq. eng.,26(1), 45-53.

Johansson, J., and Konagai, K. (2007). "Fault induced permanent ground deformations: Experimental verification of wet and dry soil, numerical findings' relation to field observations of tunnel damage and implications for design." J. Soil Dyn. Earthq. eng, 27(10), 938-956.

Joshi, S., Prashant, A., Deb, A., & Jain, S. K. (2011). Analysis of buried pipelines subjected to reverse fault motion. Soil Dynamics and Earthquake Engineering, 31(7), 930-940.

Karamitros, D. K., Bouckovalas, G. D., & Kouretzis, G. P. (2007). Stress analysis of buried steel pipelines at strike-slip fault crossings. Soil Dynamics and Earthquake Engineering, 27(3), 200-211.

Karamitros, D. K., Bouckovalas, G. D., Kouretzis, G. P., & Gkesouli, V. (2011). An analytical method for strength verification of buried steel pipelines at normal fault crossings. Soil Dynamics and Earthquake Engineering, 31(11), 1452-1464.

Kelson, K. I., Kang, K. H., Page, W. D., Lee, C. T., and Cluff, L. S. (2001). "Representative styles of deformation along the Chelungpu fault from the 1999 Chi-Chi (Taiwan) earthquake: geomorphic characteristics and responses of man-made structures". Bull. Seismol. Soc. Am. ,91(5), 930-952.

Kennedy RP, Chow AW, William RA. Fault movement effects on buried oil pipeline. Transportation Engineering Journal, ASCE 1977; 103(TES):617– 633.

Kershenbaum, N. Y., Mebarkia, S. A., & Choi, H. S. (2000). Behavior of marine pipelines under seismic faults. Ocean engineering, 27(5), 473-487.

Kokavessis, N. K., & Anagnostidis, G. S. (2006, January). Finite element modeling of buried pipelines subjected to seismic loads: soil structure interaction using contact elements. In ASME 2006 Pressure Vessels and Piping/ICPVT-11 Conference (pp. 119-125). American Society of Mechanical Engineers.

Lade, P. V., Cole Jr, D. A., and Cummings, D. (1984)."Multiple failure surfaces over dip-slip faults". J. Geotech. Engrg, 110(5), 616-627.

Loukidis, D. (1999). "Active fault propagation through soil." Thesis, School of Civil Engineering, National Technical Univ., Athens,Greece.

Lin, M. L., Chung, C. F., and Jeng, F. S. (2006). "Deformation of overburden soil induced by thrust fault slip." Engineering Geology, 88(1), 70-89.

Liu, A. W. (2002). Response analysis of a buried pipeline crossing the fault based on shell-model. China Seismological Bureau, Institute of Geophysics.

Liu, M., Wang, Y. Y., & Yu, Z. (2008, January). Response of pipelines under fault crossing. In The Eighteenth International Offshore and Polar Engineering Conference. International Society of Offshore and Polar Engineers.

Liu, A. W., Hu, Y. X., Zhao, F. X., Li, X. J., Takada, S., & Zhao, L. (2004). An equivalent-boundary method for the shell analysis of buried pipelines under fault movement. Acta Seismologica Sinica, 17(1), 150-156.

Loukidis, D. (1999). "Active fault propagation through soil." Thesis, School of Civil Engineering, National Technical Univ., Athens, Greece.

Loukidis, D., Bouckovalas, G. D., and Papadimitriou, A. G. (2009). "Analysis of fault rupture propagation through uniform soil cover." J. Soil Dyn. Earthq. Engrg, 29(11), 1389-1404.

Micarelli, L., Moretti, I., and Daniel, J. M. (2003). "Structural properties of rift-related normal faults: the case study of the Gulf of Corinth, Greece". *J. Geodyn., 36*(1), 275-303.

Moradi, M., Rojhani, M., Galandarzadeh, A., & Takada, S. (2013). Centrifuge modeling of buried continuous pipelines subjected to normal faulting. Earthquake Engineering and Engineering Vibration, 12(1), 155-164.

Nakai, T., Muir Wood, D., and Stone, K. J. L. (1995). "Numerical calculations of soil response over a displacing basement." Soils Found.,35(2), 25–35.

Newmark NM, Hall WJ. Pipeline design to resist large fault displacement. Proceedings of U.S. National Conference on Earthquake Engineering, 1975; 416 – 425.

Nobahar, A., and Kenny, S. (2007). 'Analysis and design of buried pipeline for displacement controlled hazards: A probabilistic approach.' J.OMAE. Vol.129, pp.219-228.

Odina, L., & Tan, R. (2009, January). Seismic fault displacement of buried pipelines using continuum finite element methods. In ASME 2009 28th International Conference on Ocean, Offshore and Arctic Engineering (pp. 617-625). American Society of Mechanical Engineers.

Ogawa, Y., Yanou, Y., Kawakami, M., & Kurakake, T. (2004, August). Numerical study for rupture behavior of buried gas pipeline subjected to seismic fault displacement. In Proceedings of the 13th World Conference on Earthquake Engineering, Vancouver, BC, Canada (pp. 1-6).

O'Rourke, M. J., & Liu, X. (1999). Response of buried pipelines subject to earthquake effects.

O'rourke, M., Gadicherla, V., & Abdoun, T. (2005). Centrifuge modeling of PGD response of buried pipe. Earthquake Engineering and Engineering Vibration,4(1), 69-73.

Popescu, R. and Nobahar, A. (2003, February), '3D Finite Element Analysis of Pipe-Soil Interaction – Effects of Groundwater', Final Report, C-Core Report: R-02-029-076.

Rabian, E., Mansour-Tehrani, M. and Walker, A. C. (1999, February), Subsea Pipeline Response to Seabed Movement due to Faulting, 22nd Annual Offshore Pipeline Technology Conference, Amsterdam.

Rahman, M. A., & Taniyama, H. (2015). Analysis of a buried pipeline subjected to fault displacement: A DEM and FEM study. Soil Dynamics and Earthquake Engineering, 71, 49-62.

Rojhani, M., Moradi, M., Galandarzadeh, A., & Takada, S. (2012). Centrifuge modeling of buried continuous pipelines subjected to reverse faulting. Canadian Geotechnical Journal, 49(6), 659-670.

Roth, W. H., Scott, R. F., & Austin, I. (1981). "Centrifuge modeling of fault propagation through alluvial soils." *Geophys. Res. Ltrs*, *8*(6), 561-564.

Roth, W. H., Kalsi, G., Papastamatiou, D., and Cundall, P. A. (1982). "Numerical modeling of fault propagation in soils." Proc., ., 4th Int. Conf. Num. Meth. Geomech., Edmonton, Canada ,487-494.

Sanford, A. R. (1959). "Analytical and experimental study of simple geologic structures."Geol. Soc. of Am. Bull., 70(Jan.), 19-52.

Scott, R. F., and Achoustra, J.J. (1974). "Nuclear power plant siting on deep alluvium." J. Geotech. Engrg Div, ASCE, 100 (GT4), 449-459.a66 J. Geotech. Eng. Div., Am. Soc. Civ. Eng.

Scott, R. F. (1987). "Failure." Geotechnique, London, England, 37(4), 423-466.get Geotechnique

Takada, S., Liang, J. W., & Li, T. (1998). Shell-mode response of buried pipelines to large fault movements. Journal of Structural Engineering, 44, 1637-1646.

Takada, S., Hassani, N., & Fukuda, K. (2001). A new proposal for simplified design of buried steel pipes crossing active faults. Earthquake engineering & structural dynamics, 30(8), 1243-1257.

Taniyama, H., and Watanabe, H. (2000). "Deformation of sandy deposits by fault movement." Proc., 12th WCEE (Vol. 6, pp. 325-336). Tokyo: Mc Graw Hill, CD, code.

Trifonov, O. V., & Cherniy, V. P. (2010). A semi-analytical approach to a nonlinear stress–strain analysis of buried steel pipelines crossing active faults.Soil Dynamics and Earthquake Engineering, 30(11), 1298-1308.

Trifonov, O. V., & Cherniy, V. P. (2012). Elastoplastic stress–strain analysis of buried steel pipelines subjected to fault displacements with account for service loads. Soil Dynamics and Earthquake Engineering, 33(1), 54-62.

Vazouras, P., Karamanos, S. A., & Dakoulas, P. (2010). Finite element analysis of buried steel pipelines under strike-slip fault displacements. Soil Dynamics and Earthquake Engineering, 30(11), 1361-1376.

Vasileiadis, M., Gazetas, G., & Anastasopoulos. I. (2012). Buried Pipeline Subjected to Normal and Reverse Tectonic Fault Rupture.

Walters, J. V., and Thomas, J. N. (1982). "Shear zone development in granular materials." Proc., 4th Int. Conf. Num. Meth. Geomech., Edmonton, Canada, Vol.I, 263-274.

Waltham, A.C. (1994). "Foundations of engineering geology". Blackie Academic and Professional, London

Wang, L. R. L., & Yeh, Y. H. (1985). A refined seismic analysis and design of buried pipeline for fault movement. Earthquake engineering & structural dynamics, 13(1), 75-96.

White, R. J., Stone, K. J. L., and Jewel, R. J. (1994). "Effect of particle size on localization development in model tests on sand." Proc., Inst.Centrifuge Conf., C. F. Leung, F. H. Lee, and T. S. Tan, eds.,Balkema, Rotterdam, The Netherlands, 817–822.

Zhao, L., Cui, C., & Li, X. (2010). Response analysis of buried pipelines crossing fault due to overlying soil rupture. Earthquake Science, 23(1), 111-116.

Zhang, J., Liang, Z., & Han, C. J. (2014). Buckling behavior analysis of buried gas pipeline under strike-slip fault displacement. Journal of Natural Gas Science and Engineering, 21, 921-928.